Water Interaction with Microporous Coordination Polymers: Energy Efficient Dehumidification, Antimatter Probing and Polymer Coating

by

Ping Guo

A dissertation submitted in partial fulfillment
of the requirements for the degree of
Doctor of Philosophy
(Chemistry)
in The University of Michigan
2015

Doctoral Committee:

Professor Adam J. Matzger, Chair
Professor H. Scott Fogler
Professor David W. Gidley
Professor Robert T. Kennedy

This dissertation is gratefully dedicated to my loving father and mother

Jingxiang Xu and Yan Guo

Acknowledgements

First and foremost, I would like to thank my advisor, Professor Adam J. Matzger for his guidance and support during my graduate studies. I sincerely appreciate that he has always been there for me with patience, honesty and insightful answers whenever I have questions. No words can express my gratitude towards all the support he has given me. I will always keep the advice from my incomparable mentor in mind no matter which career path I will follow after graduate school.

I would also like to thank Professor David W. Gidley for mentoring me, introducing me to positron annihilation lifetime spectroscopy, and letting me try new ideas with it. I truly appreciate that he always generously shares his knowledge of physics with me. I am very lucky to catch a glimpse of how physicists solve problems.

I am also thankful to my committee members, Professor Robert T. Kennedy and Professor H. Scott Fogler for their time and commitment to me during my graduate career.

Dr. Antek G. Wong-Foy is an excellent teacher and friend I am very grateful to have. I thank him for helping me start on projects, teaching me a variety of laboratory techniques, and offering creative suggestion about everything whenever I need his input.

I am thankful to my collaborators in physics, Dr. Dhanadeep Dutta and James Imirzian, and those outside the University of Michigan as well: Dr. William Frieze and Dr. Paolo Crivelli.

A huge thanks to the members of the Matzger lab: Dr. Kyoungmoo Koh, Dr. Onas Bolton, Dr. Baojian Liu, Dr. Saikat Roy, Dr. Tae-Hong Park, Dr. Ly Tran, Dr. Rajesh Nagula, Dr. Leila Foroughi, Dr. Austin Kizzie, Dr. Kira Landenberger, Dr. Jeremy Feldblyum, Dr. Rachel Barnard, Laura Pfund, Ananya Dutta, Zi Li, Jon Bennion, Kortney Kersten, Kyle McDonald, Jake Boissonnault, and Jialiu Ma. The camaraderie among us carries me through graduate school.

I would like to show my gratitude to my friends out of lab in Ann Arbor who have enriched my life. Special thanks to my friend Yuanyuan Zhang for standing by me through thick and thin.

I am eternally grateful for the support and encouragement from my family, especially my parents Jingxiang and Yan, and my uncle Jingfu and aunt Huayi. You taught me to see the world, to experience the unknown, and to be true to myself.

Table of Contents

List of Figures

List of Tables

Abstract

Microporous coordination polymers (MCPs) are most typically built from rigid ligands and arrays of metals/metal clusters resulting in the formation of crystalline materials; in many cases these materials are highly porous. The chemical and structural features are easily controlled in MCPs thus offering significant potential for their development as application-specific, high performance materials. However, commercial applications of MCPs have been slow to develop and one often cited barrier to applications for some MCPs is their instability against moisture. This thesis focuses on application-oriented investigation of the interaction between water and MCPs: MCPs have been intensively studied as practical industrially viable sorbents for gas dehumidification, MCP porosity evolution during water degradation has been elucidated by positronium annihilation lifetime spectroscopy (PALS), and a hybrid polymer@MCP composite with increased water stability has been studied.

MCPs are demonstrated here to be efficient desiccants for the dehumidification of air and comparison of their capacity, regenerability and efficiency with commercial activated alumina is conducted. Complete regeneration using dry air with mild heating is achieved. The achievement of high water adsorption capacity coupled to gentle regeneration indicates that gas dehumidification may be an important application for MCPs.

The details of MCPs structural collapse caused by water with regard to pore size evolution are acquired by incorporating a flow-through system in tandem with PALS. From the decrease in porosity, we have observed an induction period for water degradation of some Zn_4O-based MCPs that signals much greater stability than commonly believed to be possible. The sigmoidal trend in the degradation curve of unfunctionalized MCPs caused by water vapor has been established. The water sensitivity of Zn_4O-based MCPs is found to be structure and history dependent.

A hybrid polymer@MCP architecture is examined, which interfaces hard (crystalline) MCP, MOF-5, and soft (amorphous) polymers, polystyrene, to form polystyrene@MOF-5 in which polystyrene chains are uniformly tethered to the outer shell of MOF-5. Control over the position of polymer initiation and the thickness of the polymer coating is achieved by IRMOF-3@MOF-5 core-shell arrangement. The polystyrene@MOF-5 demonstrates an increase in the kinetic stability when subjected to humid environments.

Chapter 1 **Introduction**

1.1 **Microporous Coordination Polymers (MCPs)**

Microporous Coordination Polymers (MCPs) are crystalline materials constructed from rigid organic ligands (linkers) and metals/metal clusters, which often maintain their porosity after the removal of guests. MCPs are named with varying terminology such as metal-organic framework (MOF), porous coordination polymer (PCP), and porous coordination network (PCN), or reflecting the location where it is first created such as Hong Kong University of Science and Technology (HKUST), Matériaux de l'Institut Lavoisier (MIL), University of Oslo (UiO), and University of Michigan Crystalline Material (UMCM).

Early work by Robson and co-workers[1,2,3] in 1989-1991 defined the concept of crystalline coordination polymers and pioneered the field of MCPs. Highly ordered structures with porosities much larger than typically available in molecular crystals were shown to result from organic linkers which subsequently allowed for a variety of functionalization and controlled architectures. However, accessible porosity by gas sorption after guest removal of these early materials was not studied, mainly because their structures collapsed upon removal of guest molecules or exposure to air.

In late 1990s, coordination polymers that have permanent porosity in the absence of guest molecules, as evidenced by gas sorption, were reported by Kitagawa,[4] Williams,[5] Rosseinsky,[6] and Yaghi[7]. The incredibly diverse selection of transition metals and organic linkers available for synthesis allows for one to readily control the chemical and structural features of MCPs as compared to other porous materials. Furthermore, the hydrophilicity of the pores walls and pore geometry can be easily tuned by incorporating functional groups (e.g. amine, sulfonic acid, and carboxyl) onto the linkers. In one of the most recent review articles in *Science* about MCPs, the authors illustrated that the number

of MCP structures reported in the Cambridge Structural Database (CSD) grows exponentially to around 6000 from 1971 till 2011.[8] The number of MCPs discovered keeps growing and till 2013, there have been more than 20,000 MCPs reported and studied.[9] Since the concept of porous coordination polymers was first discovered, tremendous advances have been made towards various applications of coordination polymers such as H_2 storage[10,11,12,13], CO_2 capture[14,15,16,17,18], liquid phase separations[19,20,21], and catalysis[22]. Almost 6000 publications came up for the search for a topic combination of "metal organic framework" and "application" in Web of Science databases. However, the barrier to applications for some of the most extensively scrutinized MCPs is their instability against moisture.[23] This issue has been addressed by an ongoing effort to change the nature of the metal-linker interaction given the incredible diversity of transition metals and organic linkers available to synthesize MCPs.[24,25,26]

1.2 **Water Stability of Microporous Coordination Polymers**

Water stability of MCPs and their behavior in the presence of water/water vapor is of significant importance for adsorption applications in addition to their sorption capacity, selectivity and regenerability. This is because MCPs must be able to tolerate the water vapor existing in natural gas,[27] flue gas,[28] organic chemical streams[29] and air streams[30] to be considered as feasible sorbent candidates for real world applications.

1.2.1 Prototypical Microporous Coordination Polymers

Here we selected these prototypical MCPs to study because scientists often use these materials as templates to discover new MCPs with higher gas-accessible surface area and porosity, unique functionality and greater thermal and chemical stability via linker extension/substitution/functionalization, metal cluster substitution and postsynthetic modification. MOF-5,[7] $Zn_4O[C_6H_4(COO)_2]_3$, is one of the first intensively scrutinized MCPs with exceptionally high surface area. A family of cubic MCPs with same fundamental topology as MOF-5 have been successfully synthesized by means of linker expansion and functionalization.[9],[31] Scientists often use MOF-5 as a representative of the group of MCPs with $Zn_4O(CO_2R)_6$ metal clusters. MOF-5 has been utilized by our

research group as a benchmark material for a variety of applications.[19,32,33] The performance of MOF-5 is compromised by its sensitivity to water vapor[34,35,36,37,38] mainly due to the weak metal-linker coordination bonds between the $Zn_4O(CO_2R)_6$ metal clusters and 1,4-benzene dicarboxylate linkers.[39] However, Cychosz et al[39] have previously reported that MOF-5 maintains its crystallinity after soaking in a mixture of water and DMF in the ratio of 1:8 for one hour. Greathouse and Allendorf[34] has provided some insight into the interaction between water and MOF-5 via molecular dynamics simulations by showing modes of interaction between water molecules and MOF-5 at $Zn_4O(CO_2R)_6$ metal clusters. Powder X-ray Diffraction (PXRD)[40] and post-hydration N_2 adsorption measurements[41] have been applied to study behavior of MOF-5 in the presence of water/water vapor; however, a better quantitative understanding of the water degradation of MOF-5 is needed.

HKUST-1,[5] ($Cu_3[C_6H_3(COO)_3]_2$), has coordinatively unsaturated metal sites providing high affinity to H_2O. In 2002, Bülow and co-workers[42] reported the H_2O adsorption isotherm of HKUST-1 (also referred to as Cu-BTC), pointing out the possibility of using HKUST-1 as a drying agent or highly sensitive moisture sensor. Kaskel and co-workers[24] then published a type I water isotherm of HKUST-1 which agrees with Bülow showing its saturation capacity to be approximately 25 mol/kg (45 wt%) exceeding the benchmark industry standard zeolite 5A and 13X with saturation capacities of approximately 15 mol/kg (29 wt %).[43] Henninger et al[44] then reported that the framework of HKUST-1 goes through irreversible structural change over a few cycles of water adsorption/desorption. DeCoste and co-workers[45] have tested the stability of HKUST-1 under different relative humidities and temperatures. There is minimal degradation occurs in HKUST-1 under 40% relative humidity at 40 °C over 28 days. Our work[30] in Chapter 2 successfully demonstrates the total water capacity of HKUST-1 to be 50 wt% under dynamic flow-through condition with humid air stream of 75% relative humidity and the superior water breakthrough capacity of HKUST-1 to be 7 times that of activated alumina. HKUST-1 is proven to be fully regenerated after five hydration (humid air stream with 75% relative humidity) /thermal regeneration (80 °C with dry air flow) cycles by breakthrough curves and PXRD patterns before and after each cycles.

MIL-100,[46] $Cr_3XO[C_6H_3(COO)_3]_2$ (X=F, OH), is one of the earliest reported and most studied MCPs with good water stability. Its good hydrothermal cyclic stability has been discussed and demonstrated by Pirngruber and co-workers[47] as a highly porous sorbent under humid conditions. The stability resulting from the highly charged trivalent metal Cr^{3+} leads to a strong coordination bond between the metal and ligand.[39] MIL-100 has been reported to have high saturation water capacity based on isotherms from molecular simulation by De Lange[48] and experiments by Kitagawa[49]. However, the H_2O/air breakthrough curve reported by our group[30] shows that MIL-100 has very poor breakthrough capacity which renders it unsuitable for replacing conventional desiccants even with a promising large total water capacity.

Since first reported in 2005 by Férey and co-workers[50], MIL-101, $Cr_3XO[C_6H_4(COO)_2]_3$ (X=F, OH) has attracted enormous interests due to its high surface area, possession of both microporosity and mesoporosity, high stability against water, and acids. MIL-101 can maintain its surface area and crystallinity after immersion in boiling water for one week.[51] Both type V water isotherm[24,52,53] and a two-step H_2O/air breakthrough curve[30] of MIL-101 indicate that it has a high total water capacity; however, it possesses a very limited breakthrough capacity. Due to its mesoporosity, accumulation of certain amount of water molecules is required for water to significantly occupy the pores. This suggests a mechanism for water accumulation in the pores dominated by water-water interactions.[24,54] Employment of more hydrophilic linkers can effectively increase the water affinity of MIL-101 and therefore its breakthrough capacity.[30] The breakthrough performance of MIL-101 has been improved by changing a H atom to a SO_3H group[55,30] without compromising too much of the total water capacity due in part to the mass addition from the functional groups.

Another example of an MCP is UiO-66,[25] $Zr_6O_6[C_6H_4(COO)_2]_6$, which has been shown to possess exceptional water stability. UiO-66 consists of 12-coordinated zirconium-oxo clusters and 1,4-benzene dicarboxylate linkers. The MCP displays a reversible type V water isotherm from both experiments[23,56] and simulation[57] and a two-step H_2O/air breakthrough curve,[30] demonstrating its hydrophobicity. Functionalization of UiO-66 with hydrophilic groups such as NH_2 leads to a type I isotherm and a smooth

one-step H_2O/air breakthrough curve[30] due to a combination of the improved hydrophilicity of the linkers and small functional group size.[56]

1.2.2 Thermodynamic stability

The metal-ligand coordination bonds in MCPs are the weakest targets for water.[58] The metal-ligand coordination bond strength, although complex, can be evaluated based on Lewis acid-base coordination chemistry, e.g. the pK_a of the coordinating atom on the ligand,[59,60] metal-oxygen bond strength in corresponding metal oxide[58] and the similarity between the ligand and metal's polarizability[61].

The water stability of the metal clusters is another important factor to consider in terms of thermodynamic stability of MCPs against water. MCPs with tetranuclear zinc clusters are less water stable than those with dinuclear copper clusters, whereas MCPs with trinuclear chromium clusters were found to have long-term water stability.[39] Low and co-workers[58] suggested that the oxidation state of the metal is a vital factor for the hydrothermal stability of the MCPs through a combination of high-throughput XRD screening and molecular modeling. Jhung and co-workers[62] concluded that the inertness of the metals (Cr>Al>V) largely affects the relative chemical stability of MCPs with isoreticular structures (Cr-MIL-53>Al-MIL-53>V-MIL-47). Matzger[28] and LeVan[63] suggest that M/DOBDC has a stronger stability against moisture if the metal species is a weaker reducing agent. $M_4O[C_6H_4(COO)_2]_3$ (M=Zn, Mg, or Be) has been investigated by Bellarosa and co-workers[64] using Born–Oppenheimer Molecular Dynamics in liquid water. Their results suggested that the stronger the M-O bond in metal clusters the more water stable $M_4O[C_6H_4(COO)_2]_3$ is.

1.2.3 Kinetic stability

Even with inherent low thermodynamic water stability, some MCPs can still be utilized in a fairly large and operationally relevant window of relative humidity. High kinetic water stability allows these materials to have long-term stability against water vapor. Incorporating hydrophobic functional groups on the linkers, such as fluorinated[65,66] and alkyl[67], can improve MCP kinetic stability against water via shielding effect. Low[58] suggested that MCPs containing 6-coordinate (usually octahedral) metal ions tends to be more stable than those containing 4-coordinate (usually tetrahedral)

metal ions due to the high coordination number limiting the space available for water to attack the metal ions. UiO-66, in group with a series of porous Zr oxide dicarboxylate MOFs, such as MIL-140 series[68], DUT-51[69], have the Zr_6O_6 metal cluster with a coordination number as high as 12 which contributes to their high stability against water. One explanation is that the crowding effect[59] around metal center prevents water cluster from forming and collapsing the MCP framework. Also, MCPs containing metal ions with a high coordination number are more likely to maintain their framework structure even after hydrolysis happens.[25,70]

1.3 **Positronium Annihilation Lifetime Spectroscopy (PALS)**

A positron is an electron with positive charge-the antimatter of an electron.[71] When a positron is injected into a solid, it loses energy through collisions with the surrounding electrons until binding to one of the ionized electrons to form positronium (Ps), a bound state of an electron and a positron, which annihilates with a lifetime depending on the size of pore. Ps annihilation lifetime is longer when the pore is larger because of a reduced overlap of the Ps wave function with the surrounding electrons of the pore wall.[72] Positronium annihilation lifetime spectroscopy (PALS) is an *in situ* pore characterization technique[72] in which the reduction of the annihilation lifetime of Ps in porous dielectrics can be directly related to the size of the pores using quantum mechanical and classical models.[73,74,75] Positron can also annihilate directly with electrons within a few hundred picoseconds. There are two spin states for Ps: *ortho*-Ps with parallel spins which has a lifetime in vacuum of 142 ns or *para*-Ps with antiparallel spins which has a much shorter lifetime of 0.125 ns. The characteristic detectable annihilation lifetime of *ortho*-Ps is used for analyzing porosity. In PALS, a positron source, ^{22}NaCl, is placed adjacent to the sample being analyzed. The 1270 keV gamma ray from the beta decay of the positron source, ^{22}NaCl, can be monitored by a photomultiplier (start detector) as the start signal of the production of a positron. Ps finally annihilates with an electron inside the material and generates gamma ray photons (0-511 keV) which can be detected by another photomultiplier (stop detector). The lifetime of the positronium event is the time interval between the start and stop signals. A

Ps lifetime spectrum is then plotted as the histogram built from ~10^5-10^7 *ortho*-Ps annihilation events and fitted in the fashion of exponential decay to determine the average annihilation lifetime of *ortho*-Ps. The pore diameter then can be reliably correlated to the average *ortho*-Ps annihilation lifetime in porous material using the Tao-Eldrup model[72,76,77].

The utilization of PALS to study pores and voids in crystalline and amorphous materials has risen rapidly in the past 40 years.[72] However, there have only been a few examples[78,79] using PALS as an *in situ* nondestructive technique complementing the traditional probes for MCPs. The work by our group using PALS to study characterization of inaccessible pore space,[73] structural evolution in MOFs during heating,[78] porosity information of MOFs during gas adsorption[78,79] has proven the fruitful applications of PALS for MCPs porosity characterization.

Conventional methods to characterize water-induced degradation of MCPs are PXRD and post-exposure gas adsorption analysis. PXRD can yield crystallinity information of MCP samples. Post-exposure gas adsorption analysis can provide quantitative measurements of accessible internal surface area.[73] Neither of these techniques is well-suited to characterizing structural disorder, nor can they monitor pore structural evolution under humid conditions.[78] PALS is an ideal probe for evolution in pore size or pore size distribution due to water damage. During the water degradation of MCPs, the coordination bonds between metal clusters and organic linkers can be broken down by water molecules, the framework collapses and the relative amount of intact framework pores is reduced as a result.[80] The reduction in relative amount of intact framework pores can be detected by PALS as a decrease in the intensity of Ps annihilating in the framework pores. The humid gas flowing through the MCP sample does not interfere with the data collection of PALS. Therefore, incorporation of *in situ* PALS with a flow-through system in tandem is well suited to monitor structural evolution of MOFs in real-time under humid conditions.

1.4 **Organization of Thesis**

This thesis focuses on water interaction with microporous coordination polymers. In Chapter 2, air dehumidification using microporous coordination polymers as efficient sorbents is discussed. The packed-bed breakthrough curves were determined for MOF-5, UiO-66,[25] UiO-66-NH_2,[81] HKUST-1, Co/DOBDC,[82,83] MIL-100, MIL-101, MIL-101-SO_3H[55] and the industrial sorbent alumina for the removal of water from humid air streams. Cyclic regeneration of HKUST-1, Co/DOBDC, MIL-100 and MIL-101 were successfully performed with significantly less energy compared to alumina. Via comparison of their water capacity, regenerability and efficiency with commercial activated alumina, HKUST-1, Co/DOBDC, UiO-66-NH_2 and MIL-101-SO_3H are demonstrated to be efficient desiccants. Introduction of hydrophilic functional groups onto linkers is shown to increase breakthrough capacity and total capacity of MCPs. In Chapter 3, the study of water sensitivity in Zn_4O-based metal organic frameworks (MOFs) by PALS is described. By incorporating a flow-through system in tandem with PALS, MOF pore size evolution during water degradation is acquired under dynamic conditions. The water stability of Zn_4O-based MOFs with cubic structure was found to be related to pore size and linker hydrophilicity, as demonstrated by comparison of the behavior of UMCM-8,[84] MOF-5, $Zn_4O(FMA)_3$[85] and IRMOF-3[86]. The induction period for water degradation and greater stability against water of some Zn_4O-based MOFs are observed. A sigmoidal degradation trend of unfunctionalized Zn_4O-based MOFs has been established from the temporal component of pore size changing as characterized by *in situ* PALS. IRMOF-3 is found to have a different degradation trend and a lower relative humidity window for long-term stability than MOF-5, a finding attributed to the presence of an amine groups. In Chapter 4, preliminary results of the synthesis, characterization and water stability of a hybrid polymer-MOF composite, MOF-5 with polystyrene coating (PS@MOF-5), is presented as well as summary and future work. PS@MOF-5 in which polystyrene chains are tethered to the shell layer of MOF-5 is achieved, and is examined to have an increased water stability than the parent material MOF-5 as a result of its polystyrene coating.

1.5 References

(1) Hoskins, B. F.; Robson, R. Infinite Polymeric Frameworks Consisting of Three Dimensionally Linked Rod-like Segments. *J. Am. Chem. Soc.* **1989**, *111*, 5962–5964.

(2) Hoskins, B. F.; Robson, R. Design and Construction of a New Class of Scaffolding-like Materials Comprising Infinite Polymeric Frameworks of 3D-Linked Molecular Rods. A Reappraisal of the Zinc Cyanide and Cadmium Cyanide Structures and the Synthesis and Structure of the Diamond-Related Frameworks $[N(CH_3)_4][Cu^{I}Zn^{II}(CN)_4]$ and Cu^{I}[4,4',4'',4'''-tetracyanotetraphenylmethane]$BF_4.xC_6H_5NO_2$. *J. Am. Chem. Soc.* **1990**, *112*, 1546–1554.

(3) Abrahams, B. F.; Hoskins, B. F.; Robson, R. A New Type of Infinite 3D Polymeric Network Containing 4-Connected, Peripherally-Linked Metalloporphyrin Building Blocks. *J. Am. Chem. Soc.* **1991**, *113*, 3606–3607.

(4) Kondo, M.; Yoshitomi, T.; Matsuzaka, H.; Kitagawa, S.; Seki, K. Three-Dimensional Framework with Channeling Cavities for Small Molecules: {$[M_2(4,4'\text{-bpy})_3(NO_3)_4]\cdot xH_2O$}n (M=Co, Ni, Zn). *Angew. Chem. Int. Ed. Engl.* **1997**, *36*, 1725–1727.

(5) Chui, S. S.-Y.; Lo, S. M.-F.; Charmant, J. P. H.; Orpen, A. G.; Williams, I. D. A Chemically Functionalizable Nanoporous Material $[Cu_3(TMA)_2(H_2O)_3]_n$. *Science* **1999**, *283*, 1148–1150.

(6) Kepert, C. J.; Rosseinsky, M. J. Zeolite-like Crystal Structure of an Empty Microporous Molecular Framework. *Chem. Commun.* **1999**, 375–376.

(7) Li, H.; Eddaoudi, M.; O'Keeffe, M.; Yaghi, O. M. Design and Synthesis of an Exceptionally Stable and Highly Porous Metal-Organic Framework. *Nature* **1999**, *402*, 276–279.

(8) Long, J. R.; Yaghi, O. M. The Pervasive Chemistry of Metal–organic Frameworks. *Chem. Soc. Rev.* **2009**, *38*, 1213–1214.

(9) Furukawa, H.; Cordova, K. E.; O'Keeffe, M.; Yaghi, O. M. The Chemistry and Applications of Metal-Organic Frameworks. *Science* **2013**, *341*, 1230444.

(10) Rosi, N. L.; Eckert, J.; Eddaoudi, M.; Vodak, D. T.; Jaheon Kim; O'Keeffe, M.; Yaghi, O. M. Hydrogen Storage in Microporous Metal-Organic Frameworks. *Science* **2003**, *300*, 1127–1129.

(11) Murray, L. J.; Dincă, M.; Long, J. R. Hydrogen Storage in Metal–organic Frameworks. *Chem Soc Rev* **2009**, *38*, 1294–1314.

(12) Suh, M. P.; Park, H. J.; Prasad, T. K.; Lim, D.-W. Hydrogen Storage in Metal–Organic Frameworks. *Chem. Rev.* **2012**, *112*, 782–835.

(13) Liu, Y.; Kabbour, H.; Brown, C. M.; Neumann, D. A.; Ahn, C. C. Increasing the Density of Adsorbed Hydrogen with Coordinatively Unsaturated Metal Centers in Metal−Organic Frameworks. *Langmuir* **2008**, *24*, 4772–4777.

(14) Millward, A. R.; Yaghi, O. M. Metal−Organic Frameworks with Exceptionally High Capacity for Storage of Carbon Dioxide at Room Temperature. *J. Am. Chem. Soc.* **2005**, *127*, 17998–17999.

(15) Caskey, S.; Matzger, A. J.; Wong-Foy, A. G. Microporous Coordination Polymers as Novel Sorbents for Gas Separation. US20100258004 A1, October 14, 2010.

(16) Bloch, E. D.; Queen, W. L.; Krishna, R.; Zadrozny, J. M.; Brown, C. M.; Long, J. R. Hydrocarbon Separations in a Metal-Organic Framework with Open Iron(II) Coordination Sites. *Science* **2012**, *335*, 1606–1610.

(17) Dietzel, P. D. C.; Besikiotis, V.; Blom, R. Application of Metal–organic Frameworks with Coordinatively Unsaturated Metal Sites in Storage and Separation of Methane and Carbon Dioxide. *J Mater Chem* **2009**, *19*, 7362–7370.

(18) Lin, L.-C.; Kim, J.; Kong, X.; Scott, E.; McDonald, T. M.; Long, J. R.; Reimer, J. A.; Smit, B. Understanding CO_2 Dynamics in Metal–Organic Frameworks with Open Metal Sites. *Angew. Chem. Int. Ed.* **2013**, *52*, 4410–4413.

(19) Cychosz, K. A.; Wong-Foy, A. G.; Matzger, A. J. Enabling Cleaner Fuels: Desulfurization by Adsorption to Microporous Coordination Polymers. *J. Am. Chem. Soc.* **2009**, *131*, 14538–14543.

(20) Cychosz, K. A.; Ahmad, R.; Matzger, A. J. Liquid Phase Separations by Crystalline Microporous Coordination Polymers. *Chem. Sci.* **2010**, *1*, 293–302.

(21) Li, J.-R.; Kuppler, R. J.; Zhou, H.-C. Selective Gas Adsorption and Separation in Metal–organic Frameworks. *Chem Soc Rev* **2009**, *38*, 1477–1504.

(22) Lee, J.; Farha, O. K.; Roberts, J.; Scheidt, K. A.; Nguyen, S. T.; Hupp, J. T. Metal–organic Framework Materials as Catalysts. *Chem Soc Rev* **2009**, *38*, 1450–1459.

(23) Schoenecker, P. M.; Carson, C. G.; Jasuja, H.; Flemming, C. J. J.; Walton, K. S. Effect of Water Adsorption on Retention of Structure and Surface Area of Metal–Organic Frameworks. *Ind. Eng. Chem. Res.* **2012**, *51*, 6513–6519.

(24) Küsgens, P.; Rose, M.; Senkovska, I.; Fröde, H.; Henschel, A.; Siegle, S.; Kaskel, S. Characterization of Metal-Organic Frameworks by Water Adsorption. *Microporous Mesoporous Mater.* **2009**, *120*, 325–330.

(25) Cavka, J. H.; Jakobsen, S.; Olsbye, U.; Guillou, N.; Lamberti, C.; Bordiga, S.; Lillerud, K. P. A New Zirconium Inorganic Building Brick Forming Metal Organic Frameworks with Exceptional Stability. *J. Am. Chem. Soc.* **2008**, *130*, 13850–13851.

(26) Demessence, A.; D'Alessandro, D. M.; Foo, M. L.; Long, J. R. Strong CO_2 Binding in a Water-Stable, Triazolate-Bridged Metal−Organic Framework Functionalized with Ethylenediamine. *J. Am. Chem. Soc.* **2009**, *131*, 8784–8786.

(27) Mason, J. A.; Veenstra, M.; Long, J. R. Evaluating Metal–organic Frameworks for Natural Gas Storage. *Chem. Sci.* **2013**, *5*, 32–51.

(28) Kizzie, A. C.; Wong-Foy, A. G.; Matzger, A. J. Effect of Humidity on the Performance of Microporous Coordination Polymers as Adsorbents for CO_2 Capture. *Langmuir* **2011**, *27*, 6368–6373.

(29) Tao, W.; Yang, T.; Chang, Y.; Chang, L.; Chung, T. Effect of Moisture on the Adsorption of Volatile Organic Compounds by Zeolite 13×. *J. Environ. Eng.* **2004**, *130*, 1210–1216.

(30) Guo, P.; Wong-Foy, A. G.; Matzger, A. J. Microporous Coordination Polymers as Efficient Sorbents for Air Dehumidification. *Langmuir* **2014**, *30*, 1921–1925.

(31) Eddaoudi, M.; Kim, J.; Rosi, N.; Vodak, D.; Wachter, J.; O'Keeffe, M.; Yaghi, O. M. Systematic Design of Pore Size and Functionality in Isoreticular MOFs and Their Application in Methane Storage. *Science* **2002**, *295*, 469–472.

(32) Wong-Foy, A. G.; Matzger, A. J.; Yaghi, O. M. Exceptional H_2 Saturation Uptake in Microporous Metal−Organic Frameworks. *J. Am. Chem. Soc.* **2006**, *128*, 3494–3495.

(33) Park, T.-H.; Hickman, A. J.; Koh, K.; Martin, S.; Wong-Foy, A. G.; Sanford, M. S.; Matzger, A. J. Highly Dispersed Palladium(II) in a Defective Metal–Organic Framework: Application to C–H Activation and Functionalization. *J. Am. Chem. Soc.* **2011**, *133*, 20138–20141.

(34) Greathouse, J. A.; Allendorf, M. D. The Interaction of Water with MOF-5 Simulated by Molecular Dynamics. *J. Am. Chem. Soc.* **2006**, *128*, 10678–10679.

(35) Sabo, M.; Henschel, A.; Fröde, H.; Klemm, E.; Kaskel, S. Solution Infiltration of Palladium into MOF-5: Synthesis, Physisorption and Catalytic Properties. *J. Mater. Chem.* **2007**, *17*, 3827.

(36) Schröck, K.; Schröder, F.; Heyden, M.; Fischer, R. A.; Havenith, M. Characterization of Interfacial Water in MOF-5 ($Zn_4(O)(BDC)_3$)—a Combined Spectroscopic and Theoretical Study. *Phys Chem Chem Phys* **2008**, *10*, 4732–4739.

(37) Yang, S. J.; Choi, J. Y.; Chae, H. K.; Cho, J. H.; Nahm, K. S.; Park, C. R. Preparation and Enhanced Hydrostability and Hydrogen Storage Capacity of CNT@MOF-5 Hybrid Composite. *Chem Mater* **2009**, *21*, 1893–1897.

(38) Chen, X.; Lukaszczuk, P.; Tripisciano, C.; Rümmeli, M. H.; Srenscek-Nazzal, J.; Pelech, I.; Kalenczuk, R. J.; Borowiak-Palen, E. Enhancement of the Structure Stability of MOF-5 Confined to Multiwalled Carbon Nanotubes. *Phys. Status Solidi B* **2010**, *247*, 2664–2668.

(39) Cychosz, K. A.; Matzger, A. J. Water Stability of Microporous Coordination Polymers and the Adsorption of Pharmaceuticals from Water. *Langmuir* **2010**, *26*, 17198–17202.

(40) Kaye, S. S.; Dailly, A.; Yaghi, O. M.; Long, J. R. Impact of Preparation and Handling on the Hydrogen Storage Properties of Zn_4O(1,4-benzenedicarboxylate)$_3$ (MOF-5). *J. Am. Chem. Soc.* **2007**, *129*, 14176–14177.

(41) Sabo, M.; Henschel, A.; Fröde, H.; Klemm, E.; Kaskel, S. Solution Infiltration of Palladium into MOF-5: Synthesis, Physisorption and Catalytic Properties. *J. Mater. Chem.* **2007**, *17*, 3827–3832.

(42) Min Wang, Q.; Shen, D.; Bülow, M.; Ling Lau, M.; Deng, S.; Fitch, F. R.; Lemcoff, N. O.; Semanscin, J. Metallo-Organic Molecular Sieve for Gas Separation and Purification. *Microporous Mesoporous Mater.* **2002**, *55*, 217–230.

(43) Wang, Y.; LeVan, M. D. Adsorption Equilibrium of Carbon Dioxide and Water Vapor on Zeolites 5A and 13X and Silica Gel: Pure Components. *J. Chem. Eng. Data* **2009**, *54*, 2839–2844.

(44) Henninger, S. K.; Jeremias, F.; Kummer, H.; Janiak, C. MOFs for Use in Adsorption Heat Pump Processes. *Eur. J. Inorg. Chem.* **2012**, *2012*, 2625–2634.

(45) DeCoste, J. B.; Peterson, G. W.; Schindler, B. J.; Killops, K. L.; Browe, M. A.; Mahle, J. J. The Effect of Water Adsorption on the Structure of the Carboxylate Containing Metal–organic Frameworks Cu-BTC, Mg-MOF-74, and UiO-66. *J. Mater. Chem. A* **2013**, *1*, 11922–11932.

(46) Férey, G.; Serre, C.; Mellot-Draznieks, C.; Millange, F.; Surblé, S.; Dutour, J.; Margiolaki, I. A Hybrid Solid with Giant Pores Prepared by a Combination of Targeted Chemistry, Simulation, and Powder Diffraction. *Angew. Chem. Int. Ed.* **2004**, *43*, 6296–6301.

(47) Pirngruber, G. D.; Hamon, L.; Bourrelly, S.; Llewellyn, P. L.; Lenoir, E.; Guillerm, V.; Serre, C.; Devic, T. A Method for Screening the Potential of MOFs as CO_2 Adsorbents in Pressure Swing Adsorption Processes. *ChemSusChem* **2012**, *5*, 762–776.

(48) De Lange, M. F.; Gutierrez-Sevillano, J.-J.; Hamad, S.; Vlugt, T. J. H.; Calero, S.; Gascon, J.; Kapteijn, F. Understanding Adsorption of Highly Polar Vapors on Mesoporous MIL-100(Cr) and MIL-101(Cr): Experiments and Molecular Simulations. *J. Phys. Chem. C* **2013**, *117*, 7613–7622.

(49) Akiyama, G.; Matsuda, R.; Kitagawa, S. Highly Porous and Stable Coordination Polymers as Water Sorption Materials. *Chem. Lett.* **2010**, *39*, 360–361.

(50) Ferey, G.; Mellot-Draznieks, C.; Serre, C.; Millange, F.; Dutour, J.; Surblé, S.; Margiolaki, I. A Chromium Terephthalate-Based Solid with Unusually Large Pore Volumes and Surface Area. *Science* **2005**, *309*, 2040–2042.

(51) Hong, D.-Y.; Hwang, Y. K.; Serre, C.; Férey, G.; Chang, J.-S. Porous Chromium Terephthalate MIL-101 with Coordinatively Unsaturated Sites: Surface

Functionalization, Encapsulation, Sorption and Catalysis. *Adv. Funct. Mater.* **2009**, *19*, 1537–1552.

(52) Henninger, S. K.; Jeremias, F.; Kummer, H.; Janiak, C. MOFs for Use in Adsorption Heat Pump Processes. *Eur. J. Inorg. Chem.* **2012**, *2012*, 2625–2634.

(53) Akiyama, G.; Matsuda, R.; Sato, H.; Hori, A.; Takata, M.; Kitagawa, S. Effect of Functional Groups in MIL-101 on Water Sorption Behavior. *Microporous Mesoporous Mater.* **2012**, *157*, 89–93.

(54) Seo, Y.-K.; Yoon, J. W.; Lee, J. S.; Hwang, Y. K.; Jun, C.-H.; Chang, J.-S.; Wuttke, S.; Bazin, P.; Vimont, A.; Daturi, M.; et al. Energy-Efficient Dehumidification over Hierachically Porous Metal–Organic Frameworks as Advanced Water Adsorbents. *Adv. Mater.* **2012**, *24*, 806–810.

(55) Akiyama, G.; Matsuda, R.; Sato, H.; Takata, M.; Kitagawa, S. Cellulose Hydrolysis by a New Porous Coordination Polymer Decorated with Sulfonic Acid Functional Groups. *Adv. Mater.* **2011**, *23*, 3294–3297.

(56) Cmarik, G. E.; Kim, M.; Cohen, S. M.; Walton, K. S. Tuning the Adsorption Properties of UiO-66 via Ligand Functionalization. *Langmuir* **2012**, *28*, 15606–15613.

(57) Ghosh, P.; Colón, Y. J.; Snurr, R. Q. Water Adsorption in UiO-66: The Importance of Defects. *Chem. Commun.* **2014**, *50*, 11329–11331.

(58) Low, J. J.; Benin, A. I.; Jakubczak, P.; Abrahamian, J. F.; Faheem, S. A.; Willis, R. R. Virtual High Throughput Screening Confirmed Experimentally: Porous Coordination Polymer Hydration. *J. Am. Chem. Soc.* **2009**, *131*, 15834–15842.

(59) Burtch, N. C.; Jasuja, H.; Walton, K. S. Water Stability and Adsorption in Metal–Organic Frameworks. *Chem. Rev.* **2014**, *114*, 10575–10612.

(60) Colombo, V.; Galli, S.; Choi, H. J.; Han, G. D.; Maspero, A.; Palmisano, G.; Masciocchi, N.; Long, J. R. High Thermal and Chemical Stability in Pyrazolate-Bridged Metal–organic Frameworks with Exposed Metal Sites. *Chem. Sci.* **2011**, *2*, 1311–1319.

(61) Pearson, R. G. Hard and Soft Acids and Bases. *J. Am. Chem. Soc.* **1963**, *85*, 3533–3539.

(62) Kang, I. J.; Khan, N. A.; Haque, E.; Jhung, S. H. Chemical and Thermal Stability of Isotypic Metal–Organic Frameworks: Effect of Metal Ions. *Chem. – Eur. J.* **2011**, *17*, 6437–6442.

(63) Liu, J.; Benin, A. I.; Furtado, A. M. B.; Jakubczak, P.; Willis, R. R.; LeVan, M. D. Stability Effects on CO_2 Adsorption for the DOBDC Series of Metal–Organic Frameworks. *Langmuir* **2011**, *27*, 11451–11456.

(64) Bellarosa, L.; Calero, S.; López, N. Early Stages in the Degradation of Metal–organic Frameworks in Liquid Water from First-Principles Molecular Dynamics. *Phys. Chem. Chem. Phys.* **2012**, *14*, 7240–7245.

(65) Yang, C.; Kaipa, U.; Mather, Q. Z.; Wang, X.; Nesterov, V.; Venero, A. F.; Omary, M. A. Fluorous Metal–Organic Frameworks with Superior Adsorption and Hydrophobic Properties toward Oil Spill Cleanup and Hydrocarbon Storage. *J. Am. Chem. Soc.* **2011**, *133*, 18094–18097.

(66) Decoste, J. B.; Peterson, G. W.; Smith, M. W.; Stone, C. A.; Willis, C. R. Enhanced Stability of Cu-BTC MOF via Perfluorohexane Plasma-Enhanced Chemical Vapor Deposition. *J. Am. Chem. Soc.* **2012**, *134*, 1486–1489.

(67) Ma, D.; Li, Y.; Li, Z. Tuning the Moisture Stability of Metal–organic Frameworks by Incorporating Hydrophobic Functional Groups at Different Positions of Ligands. *Chem. Commun.* **2011**, *47*, 7377–7379.

(68) Guillerm, V.; Ragon, F.; Dan-Hardi, M.; Devic, T.; Vishnuvarthan, M.; Campo, B.; Vimont, A.; Clet, G.; Yang, Q.; Maurin, G.; et al. A Series of Isoreticular, Highly Stable, Porous Zirconium Oxide Based Metal–Organic Frameworks. *Angew. Chem. Int. Ed.* **2012**, *51*, 9267–9271.

(69) Bon, V.; Senkovskyy, V.; Senkovska, I.; Kaskel, S. Zr(IV) and Hf(IV) Based Metal–organic Frameworks with Reo-Topology. *Chem. Commun.* **2012**, *48*, 8407–8409.

(70) Valenzano, L.; Civalleri, B.; Chavan, S.; Bordiga, S.; Nilsen, M. H.; Jakobsen, S.; Lillerud, K. P.; Lamberti, C. Disclosing the Complex Structure of UiO-66 Metal Organic Framework: A Synergic Combination of Experiment and Theory. *Chem. Mater.* **2011**, *23*, 1700–1718.

(71) Positron annihilation http://www.positronannihilation.net/ (accessed Nov 24, 2014).

(72) Gidley, D. W.; Peng, H.-G.; Vallery, R. S. Positron Annihilation as a Method to Characterize Porous Materials. *Annu. Rev. Mater. Res.* **2006**, *36*, 49–79.

(73) Feldblyum, J. I.; Liu, M.; Gidley, D. W.; Matzger, A. J. Reconciling the Discrepancies between Crystallographic Porosity and Guest Access As Exemplified by Zn-HKUST-1. *J. Am. Chem. Soc.* **2011**, *133*, 18257–18263.

(74) Gidley, D. W.; Frieze, W. E.; Dull, T. L.; Sun, J.; Yee, A. F.; Nguyen, C. V.; Yoon, D. Y. Determination of Pore-Size Distribution in Low-Dielectric Thin Films. *Appl. Phys. Lett.* **2000**, *76*, 1282.

(75) Dull, T. L.; Frieze, W. E.; Gidley, D. W.; Sun, J. N.; Yee, A. F. Determination of Pore Size in Mesoporous Thin Films from the Annihilation Lifetime of Positronium. *J Phys Chem B* **2001**, *105*, 4657–4662.

(76) Eldrup, M.; Lightbody, D.; Sherwood, J. N. The Temperature Dependence of Positron Lifetimes in Solid Pivalic Acid. *Chem. Phys.* **1981**, *63*, 51–58.

(77) Tao, S. J. Positronium Annihilation in Molecular Substances. *J. Chem. Phys.* **1972**, *56*, 5499–5510.

(78) Liu, M.; Wong-Foy, A. G.; Vallery, R. S.; Frieze, W. E.; Schnobrich, J. K.; Gidley, D. W.; Matzger, A. J. Evolution of Nanoscale Pore Structure in Coordination Polymers During Thermal and Chemical Exposure Revealed by Positron Annihilation. *Adv. Mater.* **2010**, *22*, 1598–1601.

(79) Feldblyum, J. I.; Dutta, D.; Wong-Foy, A. G.; Dailly, A.; Imirzian, J.; Gidley, D. W.; Matzger, A. J. Interpenetration, Porosity, and High-Pressure Gas Adsorption in Zn_4O(2,6-Naphthalene dicarboxylate)$_3$. *Langmuir* **2013**, *29*, 8146–8153.

(80) Hausdorf, S.; Wagler, J.; Mossig, R.; Mertens, F. O. R. L. Proton and Water Activity-Controlled Structure Formation in Zinc Carboxylate-Based Metal Organic Frameworks. *J Phys Chem A* **2008**, *112*, 7567–7576.

(81) Garibay, S. J.; Cohen, S. M. Isoreticular Synthesis and Modification of Frameworks with the UiO-66 Topology. *Chem. Commun.* **2010**, *46*, 7700–7702.

(82) Dietzel, P. D. C.; Morita, Y.; Blom, R.; Fjellvåg, H. An In Situ High-Temperature Single-Crystal Investigation of a Dehydrated Metal–Organic Framework

Compound and Field-Induced Magnetization of One-Dimensional Metal–Oxygen Chains. *Angew. Chem. Int. Ed.* **2005**, *44*, 6354–6358.

(83) Caskey, S. R.; Wong-Foy, A. G.; Matzger, A. J. Dramatic Tuning of Carbon Dioxide Uptake via Metal Substitution in a Coordination Polymer with Cylindrical Pores. *J. Am. Chem. Soc.* **2008**, *130*, 10870–10871.

(84) Koh, K.; Van Oosterhout, J. D.; Roy, S.; Wong-Foy, A. G.; Matzger, A. J. Exceptional Surface Area from Coordination Copolymers Derived from Two Linear Linkers of Differing Lengths. *Chem. Sci.* **2012**, *3*, 2429.

(85) Xue, M.; Liu, Y.; Schaffino, R. M.; Xiang, S.; Zhao, X.; Zhu, G.-S.; Qiu, S.-L.; Chen, B. New Prototype Isoreticular Metal−Organic Framework $Zn_4O(FMA)_3$ for Gas Storage. *Inorg Chem* **2009**, *48*, 4649–4651.

(86) Rowsell, J. L. C.; Yaghi, O. M. Effects of Functionalization, Catenation, and Variation of the Metal Oxide and Organic Linking Units on the Low-Pressure Hydrogen Adsorption Properties of Metal−Organic Frameworks. *J. Am. Chem. Soc.* **2006**, *128*, 1304–1315.

Chapter 2 **Microporous Coordination Polymers as Efficient Sorbents for Air Dehumidification**

Published in Ping Guo, Antek G. Wong-Foy, Adam J. Matzger. *Langmuir* **2014**, 30, 1921–1925

2.1 **Introduction**

In industry, compressed air is considered the "fourth utility" after water, electricity and natural gas. Compressed air is utilized by approximately 70% of companies.[1] Broad areas of use include powering pneumatic equipment, energy storage, metal machining, vehicle service, and food processing. Upon compression, the dew point of air is raised, necessitating removal of water to avoid effects such as condensation, corrosion, and catalyst contamination.[2] Gas drying, especially when very dry air is required (dew points of -40 °C to -70 °C, corresponding to relative humidities of 0.59%-0.014% and absolute humidities of $0.13 g/m^3$-$0.0033 g/m^3$ at STP), is typically accomplished by passing a gas through regenerable desiccant beds; this method adds 15-20% to the operational costs for compressed air use.[1,3] Although alumina has enjoyed widespread acceptance as a desiccant due to its low cost and regenerability,[2] it is not particularly well-suited for drying gases with low relative humidities and has a modest capacity for water. Most importantly, regeneration is only complete at high temperatures thus requiring a large input of energy. Zeolites have been used as an alumina alternative in dehumidification, and of particular use in drying gases with low relative humidities. However, a drawback of zeolite desiccants is their low water capacities and high cost of regeneration. An estimated 75% of the cost of compressed air over a 10-year period can be attributed to energy consumption.[1] Considering the scale of compressed air use and the energy-intensive nature of the drying process, there is considerable opportunity to

develop higher performing desiccants. Here we propose microporous coordination polymers (MCPs) as high capacity and energy efficient desiccants for air drying.

MCPs are most typically built from rigid ligands (linkers) and arrays of metals/metal clusters resulting in the formation of crystalline materials; in many cases these materials are highly porous. Compared to activated alumina, the chemical and structural features are more easily controlled in MCPs thus offering significant potential for their development as application-specific, high performance materials. We hypothesize that there exists a particular opportunity in compressed air drying afforded by the characteristics of MCPs. Due to their construction from organic (and often aromatic) ligands and the presence of inorganic clusters, these materials sit at a strategic position between hydrophobic carbonaceous sorbents and hydrophilic metal oxides. Therefore it should be possible to tune affinity and capacity of MCPs to achieve high capacity coupled with modest energies of regeneration. Competing with alumina capacities while improving the energy of regeneration is a key requirement for more efficient desiccants.

A potential barrier to using MCPs for air drying is chemical instability to water. Given the incredible diversity of transition metals and organic linkers available to synthesize MCPs, this is one issue that can be addressed by choosing the appropriate metal/linker combination to construct the MCP. We previously reported the water stability of MCPs across several structure types and found correlations to the identity of their metal clusters: MCPs with tetranuclear zinc clusters are less water stable than those with dinuclear copper clusters, whereas MCPs with trinuclear chromium clusters were found to have long-term water stability.[4] Using a combination of high-throughput XRD screening and molecular modeling, Low et al[5] suggested that the number of metal ions in the cluster, oxidation state of the metals and metal-oxygen bond strength in metal oxides are important factors in the hydrothermal stability of MCPs. Walton and coworkers[6] investigated water adsorption and structural degradation of some prototypical MCPs under conditions up to 90% relative humidity at room temperature via static water vapor adsorption, PXRD and nitrogen adsorption measurements. UiO-66[7] (University of Oslo) and its derivatives[8] have been shown to possess exceptional water stability. One of the most significant series of MCPs, reported by Férey and coworkers,[9] denoted MIL

(Matériaux de l'Institut Lavoisier), has been suggested for efficient water adsorption[10] and heat transformation[11], attributed to their micro/meso porosity, high surface area and excellent stability toward water. The Ni and Co members of the M/DOBDC series, which possess exceptional CO_2 adsorption capacity, were shown by Kizzie et al[12] to recover most of their CO_2 capacity after exposure to moisture and effectively desiccated humid air in simulated flue gas streams.

2.2 **Results and Discussion**

Although a number of static water vapor sorption studies[6,13,14,15,16] have been recently reported, dynamic water adsorption using MCPs under industrially relevant conditions are noticeably absent. Here we examine the efficacy of air dehumidification by the MCPs MOF-5,[17] UiO-66,[7] UiO-66-NH_2,[18] HKUST-1,[19,20] Co/DOBDC,[21,22] MIL-100,[23] MIL-101[9] and MIL-101-SO_3H[24] (Figure 2.1) using packed bed breakthrough curves. These eight MCPs were selected as a cross-section of currently available materials under intensive investigation for sorption: MOF-5 has $Zn_4O(CO_2R)_6$ metal clusters with the structure of basic zinc acetate which are proposed to be responsible for its sensitivity to water;[4] UiO-66 is hydrothermally stable;[7] both HKUST-1 and Co/DOBDC have coordinatively unsaturated metal sites providing high affinity to guest molecules to enhance physisorption;[20,25,26,27] MIL-100 and MIL-101 are reported as water-stable;[9,10,23] UiO-66-NH_2 and MIL-101-SO_3H are selected because of their hydrophilic functional groups for comparison to the parent compounds. These materials are benchmarked against the industry standard: alumina. Several of the MCPs demonstrated extremely high water capacities, exceeding those of alumina, in flow-through adsorption experiments, and show promising regenerability as determined from cyclic thermal regeneration.

Initially the dehumidification ability of MOF-5 (a water-sensitive MCP), UiO-66 (a water-stable MCP), and alumina were compared. MCPs show total water capacities of 16 wt% and 32 wt%, under an air stream with 75% relative humidity, at 14.7 psi (298 K), respectively, compared to 21 wt% for activated alumina under the same conditions (Figure 2.2a). The breakthrough curve of MOF-5 demonstrates that water breaks through

immediately and the water signal increases rapidly, plateaus, and increases again until the bed is saturated. This rapid breakthrough indicates poor affinity consistent with the lack of coordinatively unsaturated metal sites and a relatively non-polar interior. The plateau at $C/C_0 \approx 0.6$ is attributed to the consumption of water during the transformation of MOF-5 to $ZnBDC \cdot xH_2O$ (BDC = 1,4-benzenedicarboxylate, x is between 1 and 2)[28]. Little water uptake occurs until this transformation begins (Figure 2.8). The shape of the MOF-5 breakthrough curve and its crystallinity changes (Figure 2.8) after exposure to humid air, suggesting that the total water capacity of MOF-5 can be attributed to this chemical transformation. The water-stable UiO-66 has a higher total capacity than alumina. However, it may not be industrially useful as a desiccant due to its low breakthrough capacity. Breakthrough capacity is defined as the capacity of a packed bed after which unadsorbed water vapor begins to be emitted. Total/saturation capacity is the maximum amount of water vapor that can be adsorbed per unit weight of adsorbent. The breakthrough capacity is what is vital for industrial applications since the bed typically must be regenerated prior to breakthrough.

Coordinatively unsaturated metal sites in MCPs act as strong binding sites for guest molecules, such as olefins,[29,30] acetylene,[31] carbon dioxide,[22,32] and the water molecules.[13] HKUST-1 and Co/DOBDC both possess coordinatively unsaturated metal sites and were therefore applied. It has been demonstrated that water adsorption capacity has a positive correlation with coordinatively unsaturated metal sites that can maximize the interaction between the MCP as adsorbents for dehumidification of humid air. Both HKUST-1 and Co/DOBDC effectively adsorb water from humid air with breakthrough capacities that are approximately 7 times that of alumina and total capacities of 50 wt% and 52 wt%, respectively (Figure 2.2b). The experimental water uptake capacities agree well with the maximum capacities computed based on pore volume considerations (Table 2.2), proving efficient utilization of void space in both MCPs. Moreover, their breakthrough curves are more similar to ideal ones with steep slopes, comparing favorably to that of alumina. This indicates that the passage of humid air through the bed before saturation is negligible, and that diffusion of water into the pores of HKUST-1 and Co/DOBDC and water adsorption are rapid.MIL-100 and MIL-101 have been reported to be efficient desiccants. Seo et al. have tested their hydrothermal stability and

adsorption/desorption properties.[10] The MCPs show large total capacities of water based on their isotherms.[10] Figure 2.2c presents the breakthrough curves for MIL-100 and MIL-101; both materials have very poor breakthrough capacities which render them unsuitable for replacing alumina in cases where a low relative humidity is required. If a higher relative humidity can be tolerated or the dehumidification takes place under static conditions, as in desiccant packs for quality preservation, MCPs with large saturation capacity but small breakthrough capacity could find application. MIL-101 has trinuclear chromium metal clusters with coordinatively unsaturated metal sites and two types of mesoporous cages with internal diameters close to 2.9 nm and 3.4 nm.[9] In the breakthrough curve of MIL-101 (Figure 2.2c), water begins to appear in the exit air stream from the packed bed shortly after the start of the experiment. The water signal increases quickly until it reaches approximately half of the absolute humidity of the inlet stream. At this point the breakthrough curve plateaus, and then increases until the bed is saturated. The shape of the breakthrough curve implies that, due to the mesoporosity, accumulation of certain amount of water molecules (i.e. a certain value of absolute humidity) is required for water to significantly occupy the pores. This suggests a mechanism for water accumulation in the cages dominated by water-water interaction.[10,13] MIL-100 has mesopores of two different sizes (2.5 nm and 2.9 nm) as well. Both are smaller than MIL-101, thus giving a lower total water capacity of 82 wt% (Figure 2.2c). MIL-101 has the highest total water capacity of 152 wt% among all MCPs investigated here. However, the two-step breakthrough curve of MIL-101 indicates that the enormous pore size limits the breakthrough capacity of this material. The breakthrough capacity is vital for industrial applications requiring dry air because desiccant beds need to be regenerated before water breaks through.

One of the critical challenges for the industrial application of MCPs is regenerability over multiple hydration and regeneration cycles. Here, regeneration of MCPs was achieved by passing dry air through the water exposed column while heating at 80 °C. This is a substantially lower regeneration temperature than typically employed for alumina (180-220 °C).[2] Higher flow rates and/or higher temperatures lead to reduced regeneration times. Five hydration/regeneration cycles were conducted for HKUST-1, Co/DOBDC, MIL-100 and MIL-101. Figure 2.3 and Figure 2.5-2.7 shows that the

breakthrough curves for both new and regenerated MCPs are nearly identical, indicating that the MCPs are fully regenerable under the aforementioned conditions. Similarly, PXRD patterns before and after five cycles (Figure 2.9-2.12) showed that these materials retained crystallinity.

We propose that the primary reason that the pore volumes in UiO-66, MIL-100 and MIL-101 cannot be fully utilized for dehumidification is that their pores are too hydrophobic.[13] If true, employing more hydrophilic linkers should effectively increase water affinity and therefore breakthrough capacity. Figure 2.2d shows the comparison between the breakthrough curves of UiO-66 and UiO-66-NH_2. By simply changing a H atom to an NH_2 group on the organic linker, the breakthrough is optimized while retaining comparable total capacities (Table 2.2). A similar strategy is also effective in the MIL series as evidenced by the improved breakthrough performance of MIL-101-SO_3H[24] (Figure 2.13). Though the total water capacity of MIL-101-SO_3H is lower than that of MIL-101, the breakthrough curve is transformed from a two-step curve seen in MIL-101 to a smooth one-step curve. The lower gravimetric water capacity of MIL-101-SO_3H is due in part to the mass addition from the sulfonic acid functional groups and pore volume displacement.

2.3 **Conclusions**

HKUST-1, Co/DOBDC, UiO-66, UiO-66-NH_2, MIL-100, MIL-101 and MIL-101-SO_3H have total capacities superior to the industrial sorbent of choice (alumina) for gas drying applications and HKUST-1, Co/DOBDC, UiO-66-NH_2, MIL-101-SO_3H also display superior breakthrough performance. Although capacity alone may not be sufficient to adopt a new sorbent, the fact that cyclic regeneration of the aforementioned MCPs can be achieved using significantly less energy compared to currently employed alumina, suggests that MCPs should be vigorously developed for this application. The modification of MCP linkers to increase hydrophilicity offers the possibility to increase breakthrough capacity and total capacity. These results indicate that MCPs may serve as practical, industrially viable sorbents for dehumidification. Remaining challenges to address are (1) the effects of extended cycling on capacity and (2) cost of the MCP

sorbent. The second issue is actively being pursued in industry and academia because of the current commercial interest in these materials for gas storage in transportation applications. The issue of sorbent robustness under process conditions must be scrutinized and will vary depending on the chemistry of the individual MCP, studies of which are currently underway.

2.4 Experimental Methods

2.4.1 Synthesis of MCPs

MOF-5,[17] UiO-66,[7] UiO-66-NH_2,[7,18] HKUST-1,[19,20] Co/DOBDC,[12] MIL-100,[23] MIL-101[9] and MIL-101-SO_3H[24] were synthesized and activated using previously reported methods. Alumina was obtained from SPX Dehydration & Filtration/SPX Corporation, and crushed into powder (120 mesh). The BET surface areas and pore volumes were calculated from N_2 sorption isotherms at 77K and given in Table 2.1.[33]

2.4.2 Air Breakthrough Apparatus

Breakthrough curves were acquired by packing a copper column (7.5 cm length, 0.47 cm inner diameter) with the MCP sorbent and using a gas-flow apparatus designed and constructed in-house (Figure 2.4). The MCP sorbent is contained between two glass wool plugs to immobilize the bed and keep the material tightly packed. All packed bed experiments were performed at room temperature. The packed beds were equilibrated with dry air at a flow rate of 18.8 mL/min and then treated with humid air. A humid air flow of 75% relative humidity was achieved by directing dry air through a bubbler at a flow rate of 18.8 mL/min. The bubbler was filled with saturated NaCl solution; air bubbles were forced to flow through the solution with a depth of 51cm. For Air/H_2O breakthrough experiments, Between 10 and 24 mg of a material was used. The column effluent was analyzed using a Hiden Analytical model HPR20 mass spectrometer. All calculations and plotting were performed in OriginPro 8.6.

Regeneration of MCPs was carried out by passing dry air at a flow rate of 10 mL/min through the packed beds, while heating the bed to 80 °C.

2.4.3 Post-regeneration MCP Analyses by PXRD

Samples of each material were coated in mineral oil, then loaded onto a Nylon loop and mounted onto a Rigaku R-axis Spider diffractometer. Images were collected in transmission mode with χ set at 45°, φ rotating at 10°/sec and ω oscillating between 80° and 140° at 1°/sec. Integration of the resulting images was performed in the AreaMax software package (version 2.3.8., Rigaku 2008).

2.4.4 Theoretical Maximum Water Uptake Based on Void Volumes

$$Void\ volume = \frac{1}{Crystal\ density} \times Free\ volume\ fraction$$

$$Maximium\ water\ uptake = Void\ volume \times Density\ of\ water$$

The Crystallographic Information File (CIF) files used to calculate void volumes are obtained from the Cambridge Crystallographic Data Centre. Removal of solvent molecules (bound and free), addition of hydrogen atoms and functional groups (UiO-66-NH_2 and MIL-101-SO_3H) were carried out in Material Studio (v5.5.3) prior to use of the SOLV routine in PLATON (v1.17, University of Glasgow, 2013). The crystal density and void volume calculations are performed with a probe radius of 1.2 Å and a grid spacing of0.2 Å. A water density of 0.997 g/ cm^3 (at 25 °C) is used in the calculation.

2.4.5 Breakthrough Curve Analysis of HKUST-1, CoDOBDC and Alumina

Besides what have been discussed in the results and discussion section, there are a few more fundamental parameters that can be read from the breakthrough curves of HKUST-1, CoDOBDC and the industrial benchmark activated alumina (Figure 2.2b): the retention time (T_R), the breakthrough time (T_B), the equilibrium time (T_E), and the number of theoretical plates (N).

The retention time T_R can be read from the breakthrough curve as the value corresponding to half the initial concentration, $0.5C_0$. σ_T and σ_T^* are the standard deviations of the derivative curve which correspond to ($T_{0.5\ C0} - T_{0.159\ C0}$) and ($T_{0.841C0} - T_{0.5C0}$), respectively.

The breakthrough time T_B:

$$T_B = T_R - 2\sigma_T$$

The equilibrium time T_E:

$$T_E = T_R + 2\sigma_T^*$$

The number of theoretical plates, N:

$$N = \frac{T_R(T_R - \sigma_T)}{\sigma_T^2}$$

All values are listed in Table 2.4. The number of theoretical plate (N) is defined as the number of hypothetical stages where the gas and solid sorbent establish an equilibrium with each other. The larger the number N, the more efficient of the sorption process. HKUST-1 and CoDOBDC both have their N more than 40 times larger than that of alumina. Moreover, even though HKUST-1 and CoDOBDC have similar equilibrium time (T_E) as alumina, both of them have much longer retention time (T_R) and breakthrough time (T_B). All the three breakthrough curves have some asymmetry to different extents, which is why the values of σ_T and σ_T^* are different. Due to a faster chemical interaction with water, a faster gas diffusion within the sorbents and less heterogeneity of the packed beds, HKUST-1 and CoDOBDC have a smaller tailing and later initial breakthrough. Therefore, HKUST-1 and CoDOBDC have much better dehumidification performance and effectiveness than alumina.

2.5 **Figures**

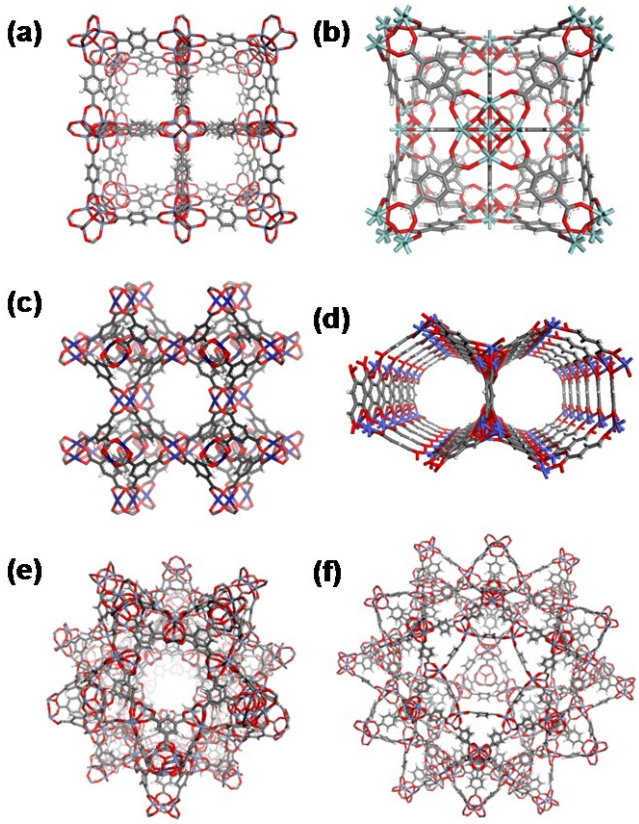

Figure 2.1 Crystal structures of (a) MOF-5, $Zn_4O[C_6H_4(COO)_2]_3$; (b) UiO-66, $Zr_6O_6[C_6H_4(COO)_2]_6$; (c) HKUST-1, $Cu_3[C_6H_3(COO)_3]_2$; (d) Co/DOBDC, $Co_2[C_6H_2O_2(COO)_2]$; (e) MIL-100, $Cr_3XO[C_6H_3(COO)_3]_2$ (X=F, OH); (f) MIL-101, $Cr_3XO[C_6H_4(COO)_2]_3$ (X=F, OH)

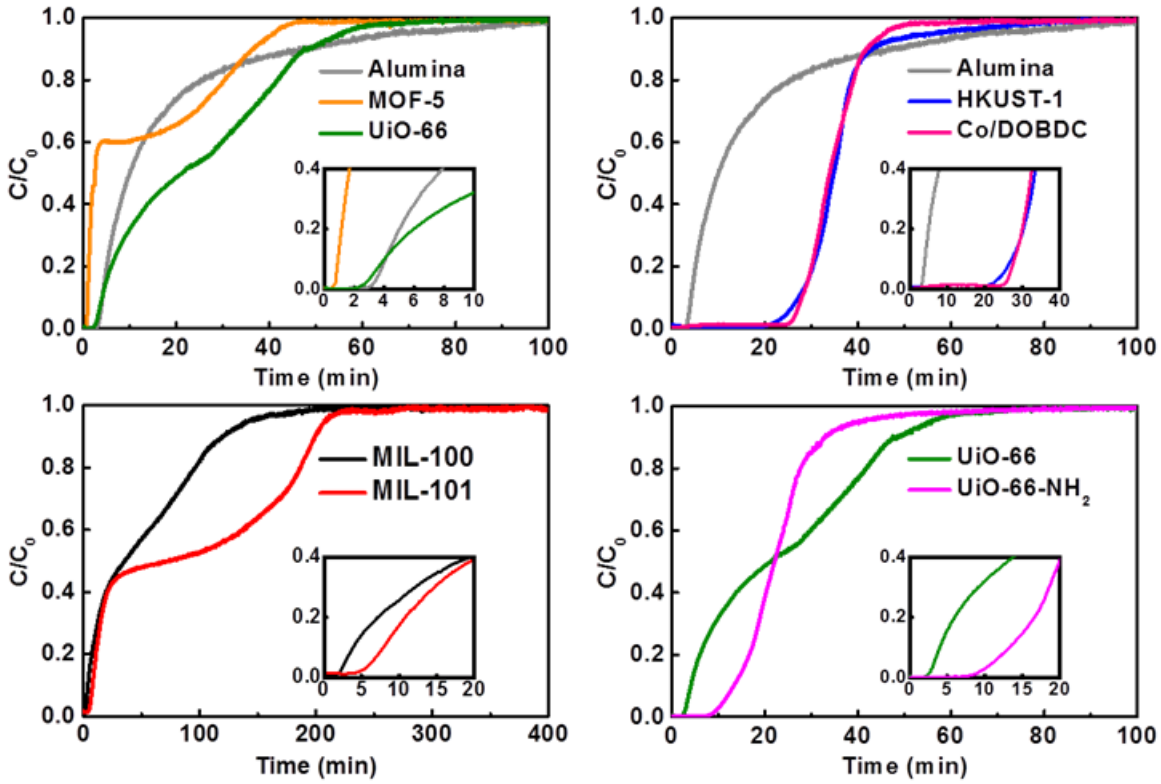

Figure 2.2 Humid air breakthrough curves in packed beds of (a) activated alumina (gray), MOF-5 (orange), UiO-66 (green), (b) activated alumina (gray), HKUST-1 (blue), Co/DOBDC (pink), (c) MIL-100 (black) and MIL-101 (red), (d) UiO-66 (green) and UiO-66-NH_2 (magenta). A humid air stream with a flow rate of 18.8 mL/min and C_0 = 75% relative humidity at 25 °C was employed. Between 10 and 24 mg of a material was used to pack the bed and all data have been normalized to 20 mg of adsorbent.

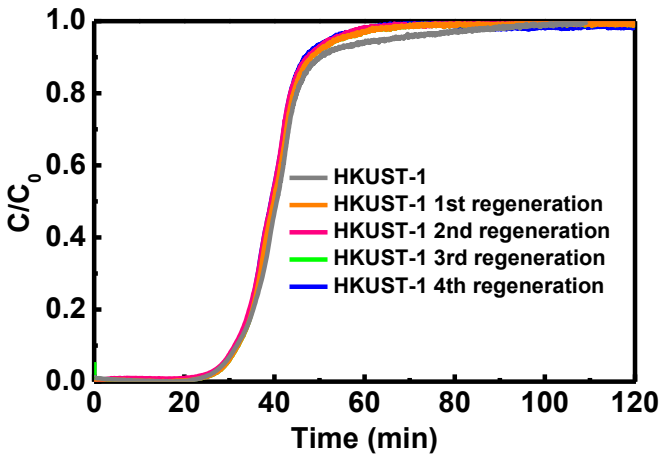

Figure 2.3 Humid air breakthrough curves before and after regeneration cycles of HKUST-1 (23.3 mg). A humid air stream with a flow rate of 18.8 mL/min and C_0 = 75% relative humidity at 25 °C was employed. Regeneration of MCPs was carried out by passing dry air at a flow rate of 10 mL/min through the packed beds, while heating the bed to 80 °C.

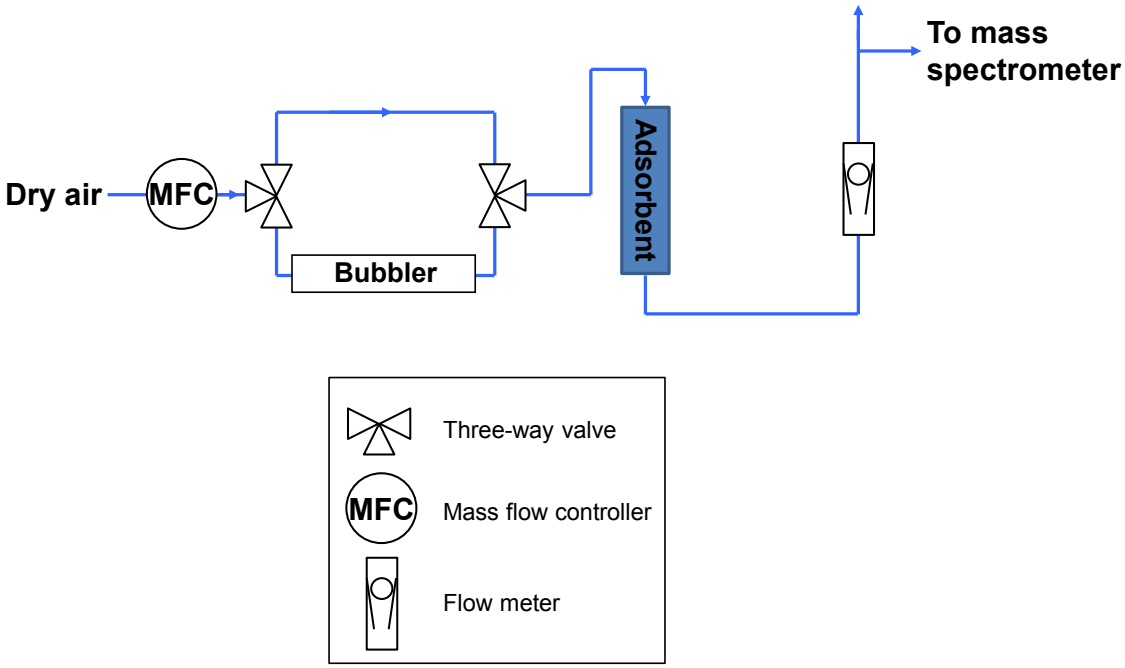

Figure 2.4 Block flow diagram of gas-flow apparatus

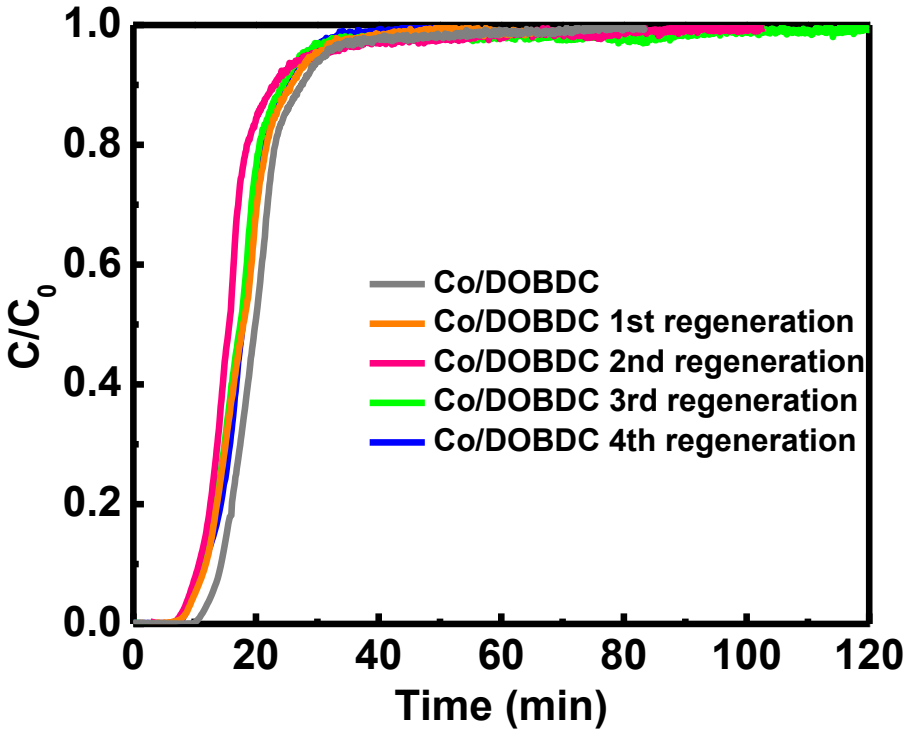

Figure 2.5 Humid air breakthrough curves before and after regeneration cycles of Co/DOBDC (10.0 mg).

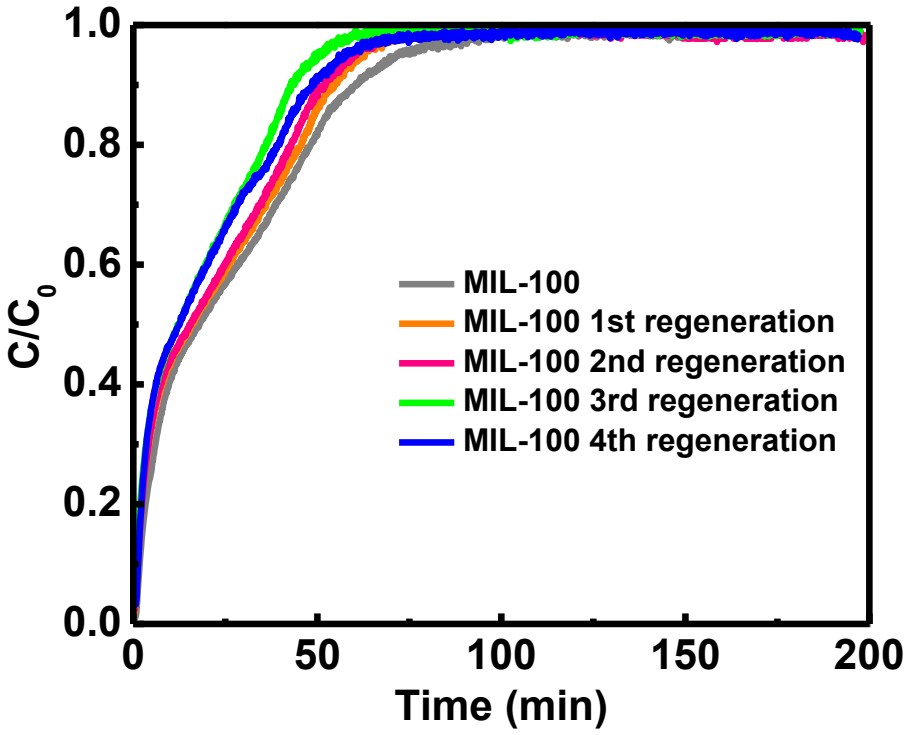

Figure 2.6 Humid air breakthrough curves before and after regeneration cycles of MIL-100 (10.0 mg).

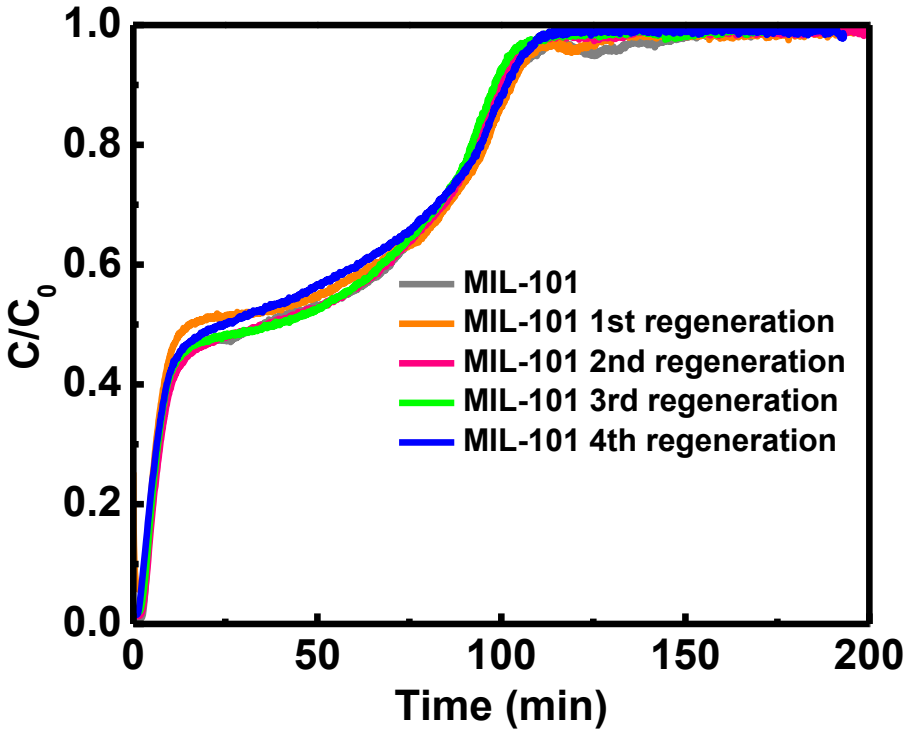

Figure 2.7 Humid air breakthrough curves before and after regeneration cycles of MIL-101 (10.1 mg).

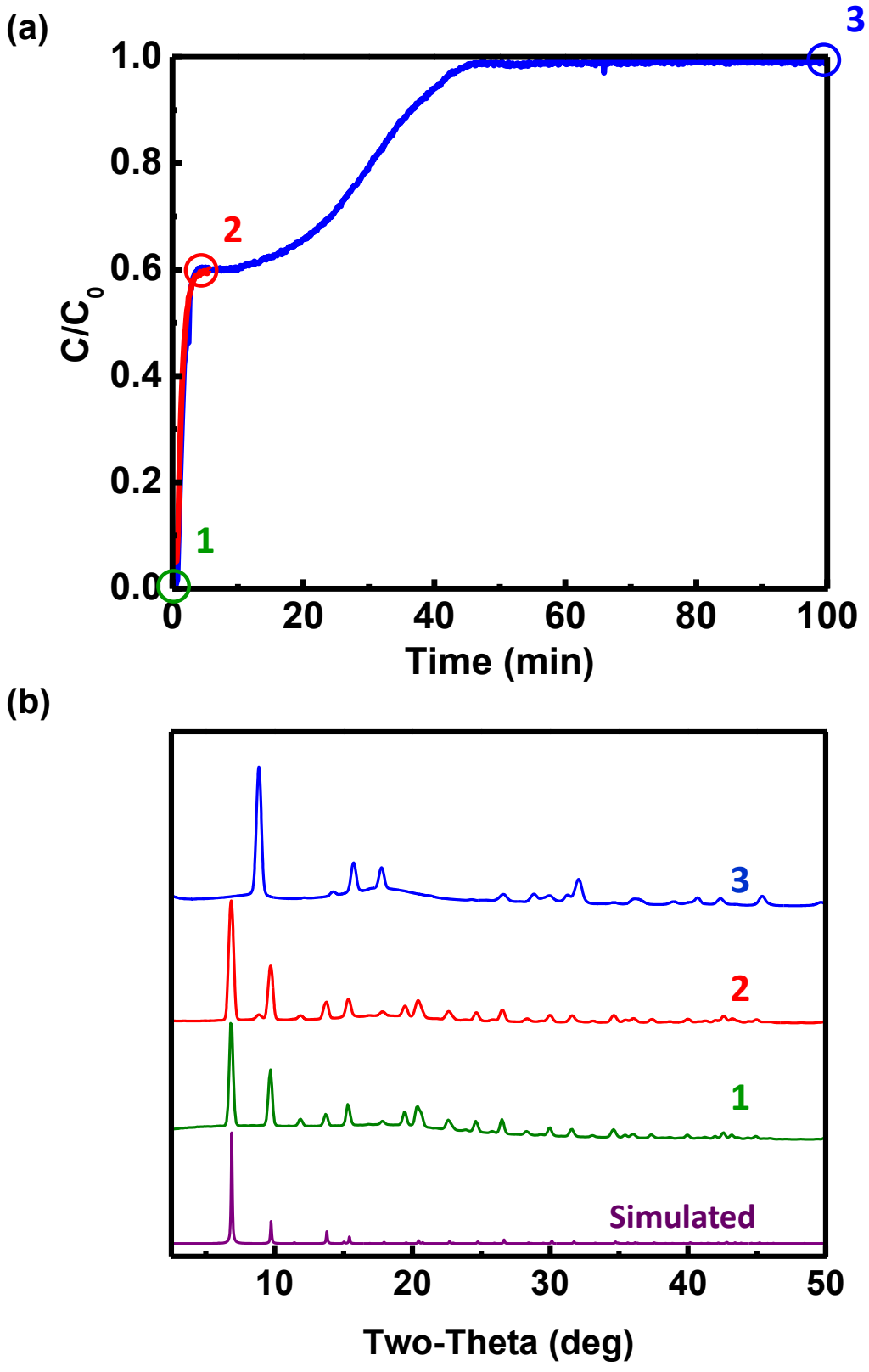
(a)
1.0
0.8
0.6
0.4
0.2
0.0
C/C0
0
20
40
60
80
100
Time (min)
1
2
3
(b)
3
2
1
Simulated
10
20
30
40
50
Two-Theta (deg)

Figure 2.8 (a) Humid air breakthrough curves in packed beds of MOF-5. A humid air stream with a flow rate of 18.8 mL/min and C0 = 75% relative humidity at 25 °C was employed. All data have been normalized to 20 mg of adsorbent. The breakthrough experiments were terminated at different stages, materials were taken out for PXRD analyses immediately. (b) Overlay of simulated PXRD pattern of MOF-5 (purple), patterns of initial activated MOF-5 (green, marked as 1), MOF-5 on the plateau (red, marked as 2) and fully broken through material (blue, marked as 3). The colors indicate to point at which the materials were sampled on the breakthrough curves in (a).

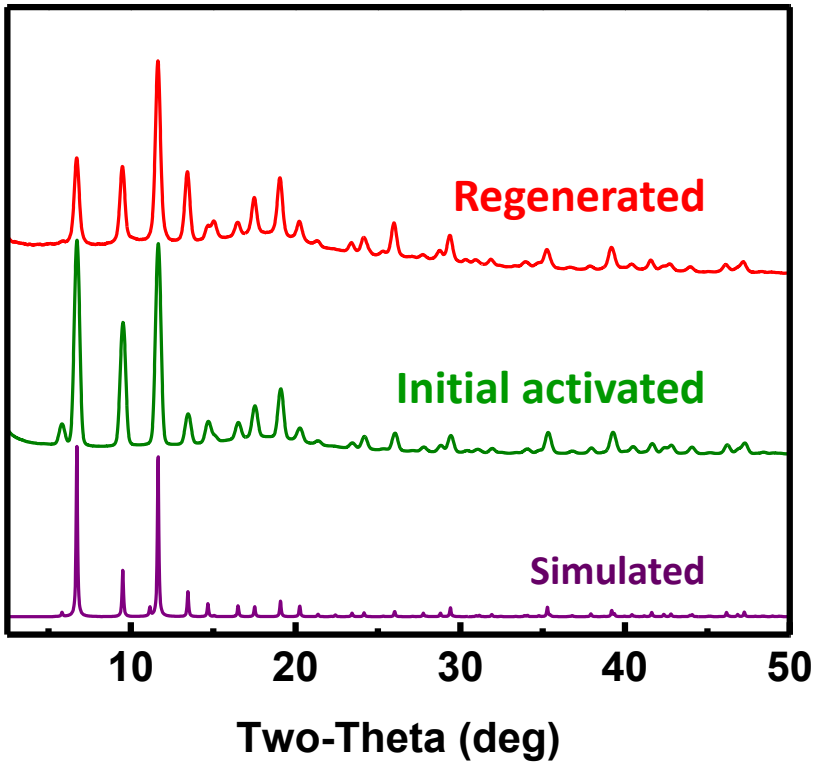

Figure 2.9 Overlay of PXRD patterns of simulated, initial activated HKUST-1 and HKUST-1after four cycles of hydration at 75% RH/ regeneration at 80 °C.

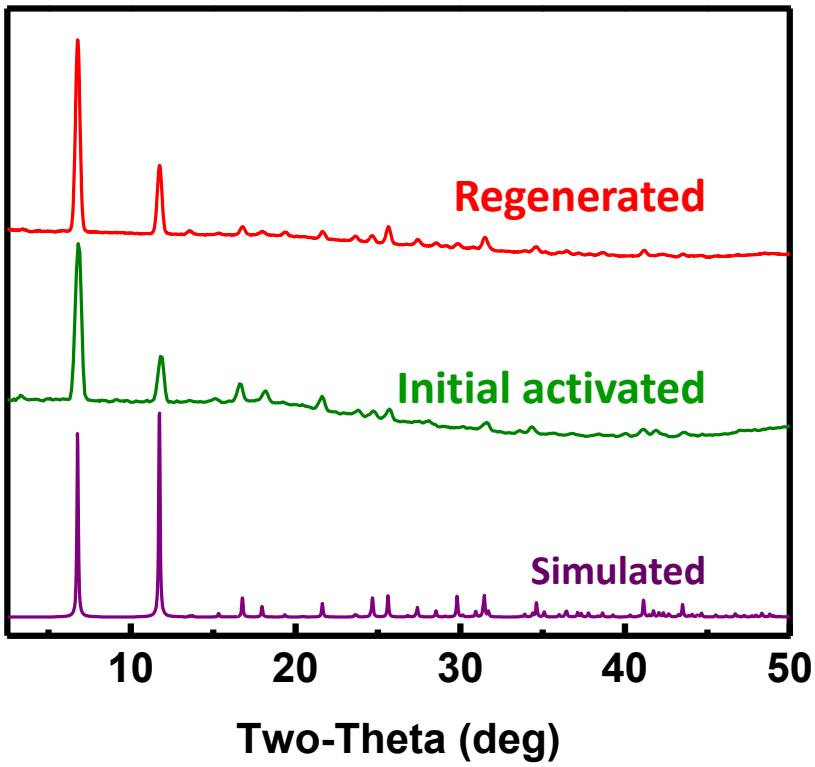

Figure 2.10 Overlay of PXRD patterns of simulated, initial activated Co/DOBDC and Co/DOBDC after four cycles of hydration at 75% RH/ regeneration at 80 °C.

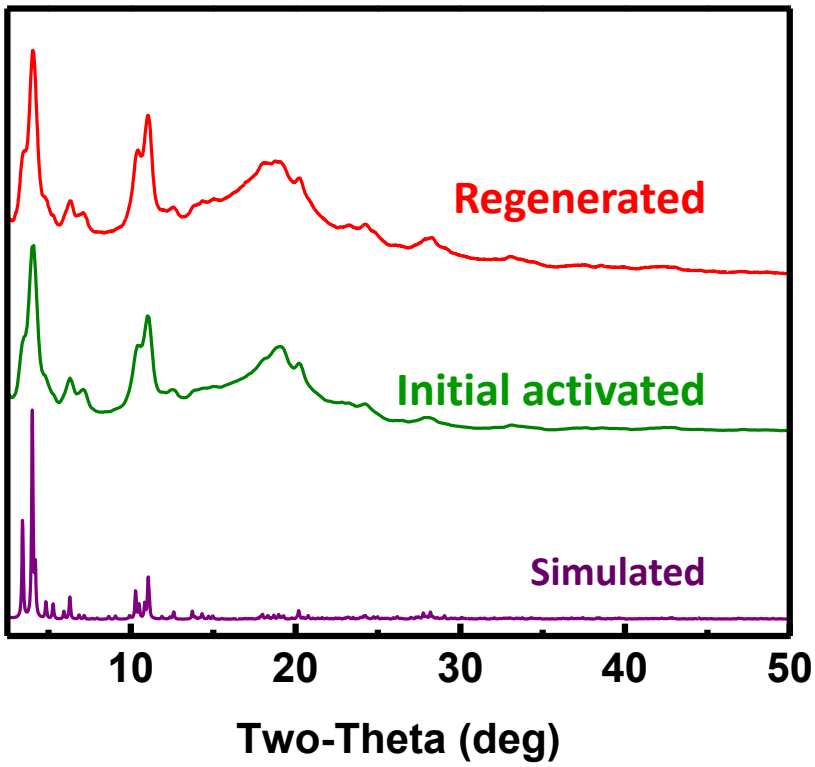

Figure 2.11 Overlay of PXRD patterns of simulated, initial activated MIL-100 and MIL-100 after four cycles of hydration at 75% RH/ regeneration at 80 °C.

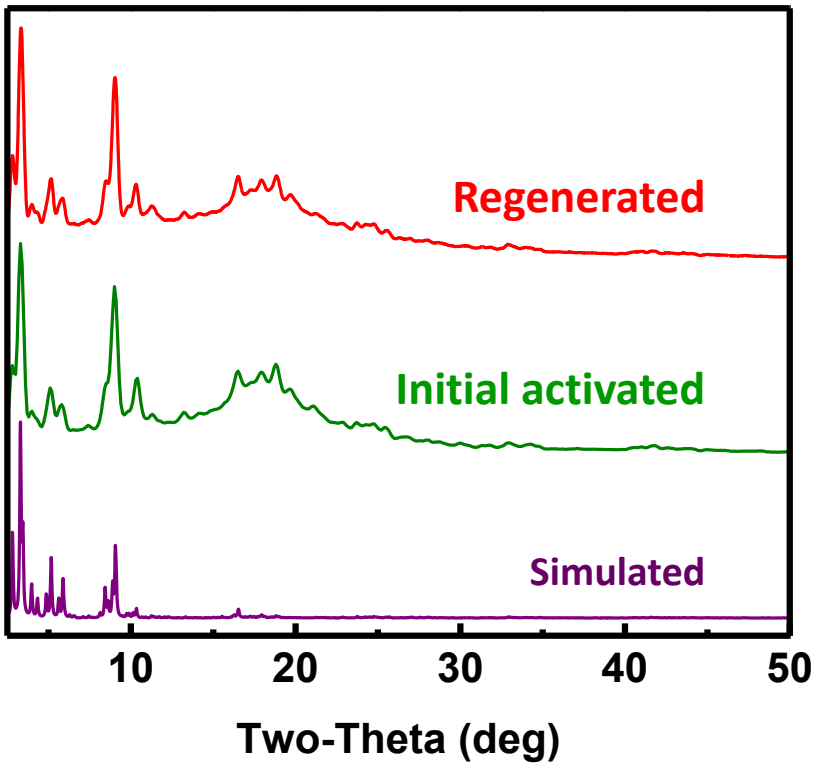

Figure 2.12 Overlay of PXRD patterns of simulated, activated MIL-101 and MIL-101 after four cycles of hydration at 75% RH/ regeneration at 80 °C.

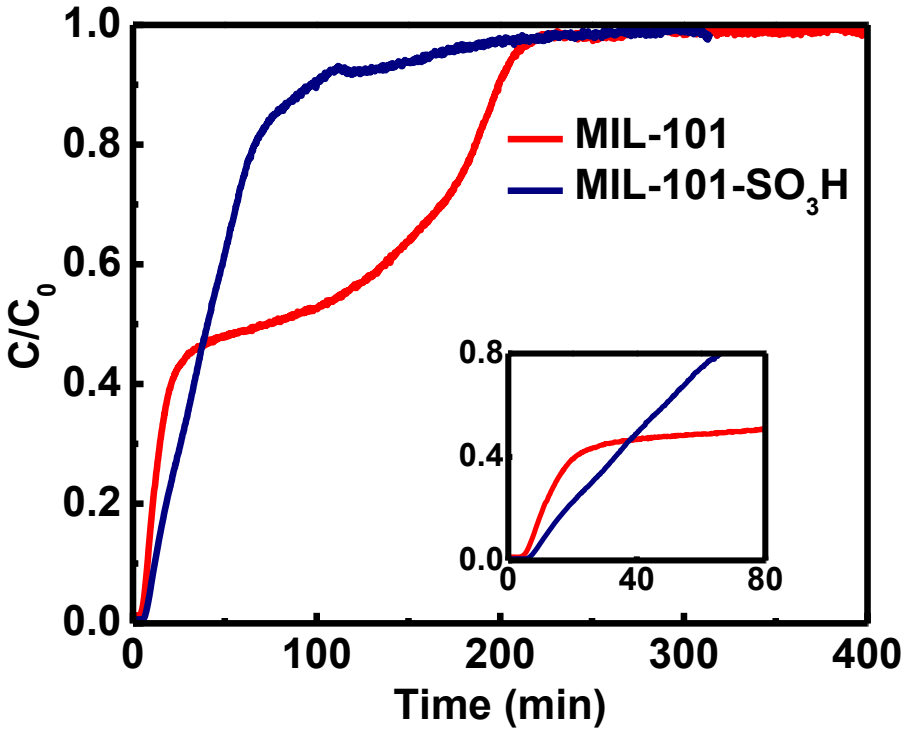

Figure 2.13 Humid air breakthrough curves in packed beds of MIL-101 (red) and MIL-101-SO3H (navy). Inset is the portions of the curves used for breakthrough determination. A humid air stream with a flow rate of 18.8 mL/min and C0 = 75% relative humidity at 25 °C was employed. Data have been normalized to 20 mg of adsorbent.

2.6 **Tables**

Table 2.1 BET surface areas and pore volumes calculated according to the N_2 adsorption isotherms at 77K of all activated MCPs and alumina.

Sample	BET surface area (m^2/g)	Pore volume (cm^3/g) taken at $P/P_0=0.9$
MOF-5	3425	1.517
UiO-66	995	0.523
UiO-66-NH_2	860	0.421
HKUST-1	1747	0.810
Co/DOBDC	1312	0.576
MIL-100	1758	0.907
MIL-101	3026	1.716
MIL-101-SO_3H	1523	0.820
Alumina	249	0.377

Table 2.2 Void volumes (cm^3/g) and maximum water uptake (g H_2O/g MCP) of MCPs.

MCP	CCDC CIF file Ref Code	Crystal density (g/cm^3)	Free volume fraction	Void volume (cm^3/g MCP)	Maximum water uptake (wt%)	Experimental water uptake (wt%)
UiO-66	RUBTAK	1.219	0.515	0.422	42%	32%
UiO-66-NH_2	RUBTAK	1.315	0.477	0.363	36%	30%
HKUST-1	DOTSOV	0.885	0.688	0.777	78%	50%
Co/DOBDC	NAVJAW	1.175	0.587	0.500	50%	52%
MIL-100	UDEMEW	0.683	0.688	1.007	100%	82%
MIL-101	OCUNAC	0.428	0.910	2.126	212%	152%
MIL-101-SO_3H	OCUNAC	0.428	0.833	1.949	194%	86%

The Crystallographic Information File (CIF) files used to calculate void volumes are obtained from the Cambridge Crystallographic Data Centre. Removal of solvent molecules (bound and free), addition of hydrogen atoms and functional groups (UiO-66-NH_2 and MIL-101-SO_3H) were carried out in Material Studio (v5.5.3) prior to use of the SOLV routine in PLATON (v1.17, University of Glasgow, 2013). The crystal density and void volume calculations are performed with a probe radius of 1.2 Å and a grid spacing of 0.2 Å. A water density of 0.997 g/ cm^3 (at 25 °C) is used in the calculation.

Table 2.3 Dynamic capacities at breakthrough and dynamic capacities at equilibrium.

Sample	Dynamic capacities at breakthrough (wt%)	Dynamic capacities at equilibrium (wt%)
MOF-5	1	16
UiO-66	4	32
UiO-66-NH_2	13	30
HKUST-1	31	50
Co/DOBDC	41	52
MIL-100	0	82
MIL-101	4	152
MIL-101-SO_3H	6	82
Alumina	5	21

Table 2.4 Breakthrough curve parameters of HKUST-1, CoDOBDC and alumina.

Material	M (mg)	T_R (min)	σ_T (min)	σ_T^* (min)	T_B	T_E	N
HKUST-1	23.3	40.6	2.3	5.8	36.0	52.2	294
CoDOBDC	23.2	39.3	2.2	6.9	34.9	53.1	301
Alumina	20.6	10.4	3.2	20.8	4.0	52.0	7

2.7 References

(1) Morvay, Z. K.; Gvozdenac, D. D. Compressed Air System. In *Applied Industrial Energy and Environmental Management*; John Wiley & Sons, Ltd, 2009; pp. 323–354.

(2) Ducreux, O.; Lavigne, C.; Nedez, C. Air and Gas Drying with Activated Alumina, 2011.

(3) Derr, R. B. Drying Air and Commercial Gases with Activated Alumina. *Ind Eng Chem* **1938**, *30*, 384–388.

(4) Cychosz, K. A.; Matzger, A. J. Water Stability of Microporous Coordination Polymers and the Adsorption of Pharmaceuticals from Water. *Langmuir* **2010**, *26*, 17198–17202.

(5) Low, J. J.; Benin, A. I.; Jakubczak, P.; Abrahamian, J. F.; Faheem, S. A.; Willis, R. R. Virtual High Throughput Screening Confirmed Experimentally: Porous Coordination Polymer Hydration. *J. Am. Chem. Soc.* **2009**, *131*, 15834–15842.

(6) Schoenecker, P. M.; Carson, C. G.; Jasuja, H.; Flemming, C. J. J.; Walton, K. S. Effect of Water Adsorption on Retention of Structure and Surface Area of Metal–Organic Frameworks. *Ind Eng Chem Res* **2012**, *51*, 6513–6519.

(7) Cavka, J. H.; Jakobsen, S.; Olsbye, U.; Guillou, N.; Lamberti, C.; Bordiga, S.; Lillerud, K. P. A New Zirconium Inorganic Building Brick Forming Metal Organic Frameworks with Exceptional Stability. *J. Am. Chem. Soc.* **2008**, *130*, 13850–13851.

(8) Kim, M.; Cohen, S. M. Discovery, Development, and Functionalization of Zr(iv)-Based Metal–organic Frameworks. *CrystEngComm* **2012**, *14*, 4096–4104.

(9) Ferey, G.; Mellot-Draznieks, C.; Serre, C.; Millange, F.; Dutour, J.; Surblé, S.; Margiolaki, I. A Chromium Terephthalate-Based Solid with Unusually Large Pore Volumes and Surface Area. *Science* **2005**, *309*, 2040–2042.

(10) Seo, Y.-K.; Yoon, J. W.; Lee, J. S.; Hwang, Y. K.; Jun, C.-H.; Chang, J.-S.; Wuttke, S.; Bazin, P.; Vimont, A.; Daturi, M.; et al. Energy-Efficient

Dehumidification over Hierachically Porous Metal–Organic Frameworks as Advanced Water Adsorbents. *Adv. Mater.* **2012**, *24*, 806–810.

(11) Ehrenmann, J.; Henninger, S. K.; Janiak, C. Water Adsorption Characteristics of MIL-101 for Heat-Transformation Applications of MOFs. *Eur. J. Inorg. Chem.* **2011**, *2011*, 471–474.

(12) Kizzie, A. C.; Wong-Foy, A. G.; Matzger, A. J. Effect of Humidity on the Performance of Microporous Coordination Polymers as Adsorbents for CO2 Capture. *Langmuir* **2011**, *27*, 6368–6373.

(13) Küsgens, P.; Rose, M.; Senkovska, I.; Fröde, H.; Henschel, A.; Siegle, S.; Kaskel, S. Characterization of Metal-Organic Frameworks by Water Adsorption. *Microporous Mesoporous Mater.* **2009**, *120*, 325–330.

(14) Min Wang, Q.; Shen, D.; Bülow, M.; Ling Lau, M.; Deng, S.; Fitch, F. R.; Lemcoff, N. O.; Semanscin, J. Metallo-Organic Molecular Sieve for Gas Separation and Purification. *Microporous Mesoporous Mater.* **2002**, *55*, 217–230.

(15) Biemmi, E.; Darga, A.; Stock, N.; Bein, T. Direct Growth of Cu3(BTC)2(H2O)3 · xH2O Thin Films on Modified QCM-Gold Electrodes – Water Sorption Isotherms. *Microporous Mesoporous Mater.* **2008**, *114*, 380–386.

(16) Gutiérrez-Sevillano, J. J.; Vicent-Luna, J. M.; Dubbeldam, D.; Calero, S. Molecular Mechanisms for Adsorption in Cu-BTC Metal Organic Framework. *J. Phys. Chem. C* **2013**, *117*, 11357–11366.

(17) Li, H.; Eddaoudi, M.; O'Keeffe, M.; Yaghi, O. M. Design and Synthesis of an Exceptionally Stable and Highly Porous Metal-Organic Framework. *Nature* **1999**, *402*, 276–279.

(18) Garibay, S. J.; Cohen, S. M. Isoreticular Synthesis and Modification of Frameworks with the UiO-66 Topology. *Chem. Commun.* **2010**, *46*, 7700–7702.

(19) Chui, S. S.-Y.; Lo, S. M.-F.; Charmant, J. P. H.; Orpen, A. G.; Williams, I. D. A Chemically Functionalizable Nanoporous Material $[Cu_3(TMA)_2(H_2O)_3]_n$. *Science* **1999**, *283*, 1148–1150.

(20) Rowsell, J. L. C.; Yaghi, O. M. Effects of Functionalization, Catenation, and Variation of the Metal Oxide and Organic Linking Units on the Low-Pressure

Hydrogen Adsorption Properties of Metal−Organic Frameworks. *J. Am. Chem. Soc.* **2006**, *128*, 1304–1315.

(21) Dietzel, P. D. C.; Morita, Y.; Blom, R.; Fjellvåg, H. An In Situ High-Temperature Single-Crystal Investigation of a Dehydrated Metal–Organic Framework Compound and Field-Induced Magnetization of One-Dimensional Metal–Oxygen Chains. *Angew. Chem. Int. Ed.* **2005**, *44*, 6354–6358.

(22) Caskey, S. R.; Wong-Foy, A. G.; Matzger, A. J. Dramatic Tuning of Carbon Dioxide Uptake via Metal Substitution in a Coordination Polymer with Cylindrical Pores. *J. Am. Chem. Soc.* **2008**, *130*, 10870–10871.

(23) Férey, G.; Serre, C.; Mellot-Draznieks, C.; Millange, F.; Surblé, S.; Dutour, J.; Margiolaki, I. A Hybrid Solid with Giant Pores Prepared by a Combination of Targeted Chemistry, Simulation, and Powder Diffraction. *Angew. Chem. Int. Ed.* **2004**, *43*, 6296–6301.

(24) Akiyama, G.; Matsuda, R.; Sato, H.; Takata, M.; Kitagawa, S. Cellulose Hydrolysis by a New Porous Coordination Polymer Decorated with Sulfonic Acid Functional Groups. *Adv. Mater.* **2011**, *23*, 3294–3297.

(25) Wong-Foy, A. G.; Matzger, A. J.; Yaghi, O. M. Exceptional H_2 Saturation Uptake in Microporous Metal−Organic Frameworks. *J. Am. Chem. Soc.* **2006**, *128*, 3494–3495.

(26) Dincă, M.; Long, J. R. Hydrogen Storage in Microporous Metal–Organic Frameworks with Exposed Metal Sites. *Angew. Chem. Int. Ed.* **2008**, *47*, 6766–6779.

(27) Liu, Y.; Kabbour, H.; Brown, C. M.; Neumann, D. A.; Ahn, C. C. Increasing the Density of Adsorbed Hydrogen with Coordinatively Unsaturated Metal Centers in Metal−Organic Frameworks. *Langmuir* **2008**, *24*, 4772–4777.

(28) Hausdorf, S.; Wagler, J.; Mossig, R.; Mertens, F. O. R. L. Proton and Water Activity-Controlled Structure Formation in Zinc Carboxylate-Based Metal Organic Frameworks. *J Phys Chem A* **2008**, *112*, 7567–7576.

(29) Caskey, S.; Matzger, A. J.; Wong-Foy, A. G. Microporous Coordination Polymers as Novel Sorbents for Gas Separation. US20100258004 A1, October 14, 2010.

(30) Bloch, E. D.; Queen, W. L.; Krishna, R.; Zadrozny, J. M.; Brown, C. M.; Long, J. R. Hydrocarbon Separations in a Metal-Organic Framework with Open Iron(II) Coordination Sites. *Science* **2012**, *335*, 1606–1610.

(31) Xiang, S.; Zhou, W.; Gallegos, J. M.; Liu, Y.; Chen, B. Exceptionally High Acetylene Uptake in a Microporous Metal−Organic Framework with Open Metal Sites. *J. Am. Chem. Soc.* **2009**, *131*, 12415–12419.

(32) Dietzel, P. D. C.; Besikiotis, V.; Blom, R. Application of Metal–organic Frameworks with Coordinatively Unsaturated Metal Sites in Storage and Separation of Methane and Carbon Dioxide. *J Mater Chem* **2009**, *19*, 7362–7370.

(33) Walton, K. S.; Snurr, R. Q. Applicability of the BET Method for Determining Surface Areas of Microporous Metal−Organic Frameworks. *J. Am. Chem. Soc.* **2007**, *129*, 8552–8556.

Chapter 3 **Water Sensitivity in Zn_4O-Based MOFs is Structure and History Dependent**

Unpublished work/Submitted

3.1 **Introduction**

Metal organic frameworks (MOFs) have attracted broad interest from scientists and engineers because their porosity is often maintained in the absence of guests. Furthermore, their regular and controllable crystalline structure offers a level of control over both chemical functionality and pore geometry. Thus MOFs have been investigated as candidates for applications such as H_2 storage[1,2,3,4], CO_2 capture[5,6,7,8,9], liquid phase separations[10,11,12], and catalysis[13]. Commercial applications of MOFs have been slow to develop and one often cited barrier to applications for some of the earliest and most extensively studied classes of MOFs is their instability against moisture.[14] Tremendous advances have been made towards the goal of water-stable/water-resistant MOFs and these advances have primarily been realized by changing the nature of the metal-linker interaction.[15,16,17]

The degradation of some MOFs caused by water has been monitored by powder X-ray diffraction (PXRD)[18,19], post-exposure gas sorption analysis[14,15], and optical microscopy[20]. For example, a PXRD study of the structural integrity of a variety of MOFs exposed to various concentrations of water in organic solvent led to the conclusion that one of the decisive factors in determining water stability of MOFs is their metal clusters.[18] MOFs with $Zn_4O(CO_2R)_6$ metal clusters are less water stable compared to the ones with copper paddlewheel clusters followed by those with trinuclear chromium clusters; this ordering is in general accord with computational predictions from quantum mechanical calculations based upon cluster models[19]. Water stability of MOFs has also been proposed to be influenced by many factors such as the number of metal ions in the

cluster, oxidation state of the metals and metal-oxygen bond strength in the corresponding metal oxides.[19] The effect of linker functionality on MOF humidity stability has received considerable attention.[21] The MOF often becomes less sensitive to moisture when hydrophobic functional groups are incorporated. A critical shortcoming with the previous studies is that the techniques applied so far offer limited understanding of the interaction between water and MOFs. PXRD gives averaged information about bulk crystallinity, but offers little information on disorder; gas sorption analysis can quantitatively measure the accessible internal surface area, but no information on local disorder or porosity inaccessible to the probe gas is obtained. Most importantly, neither of these techniques can characterize disorder and monitor pore structural changes during adsorption in real-time. PXRD is known to sometimes predict high porosity when none is observed[22], and sorption analysis requires halting water exposure and re-evacuating the sample prior to analysis. In other words, the two central techniques for understanding porosity changes upon water exposure are fundamentally inadequate. Here we overcome many of these limitations by utilizing a complementary technique, positronium annihilation lifetime spectroscopy (PALS), integrated into a gas flow-through system (Figure 3.8). Striking results have been found that suggest wide regions of exceptional stability even for those materials previously considered to be quite sensitive. In particular the focus of this study is MOFs based on the Zn_4O cluster and their water induced degradation. $Zn_4O(FMA)_3$,[23] MOF-5,[24] UMCM-8,[25] and IRMOF-3[26] are found to be stable under a certain range of relative humidities for extended time periods and display stabilities not possible to rationalize solely from the chemistry of the isolated metal cluster (Figure 3.1).

PALS has been utilized as a probe for vacancies and pores in crystalline and amorphous materials for over 40 years.[27] However, PALS is quite new to the MOF field, with only a few examples[28,29] validating it as an *in situ* nondestructive technique complementing the traditional probes for MOFs. Characterization of inaccessible pore space,[22] structural evolution in MOFs during heating,[28] porosity information of MOFs during gas adsorption[28,29] have all been successfully studied. Since the positronium (Ps) annihilation lifetime in porous materials can be reliably correlated to the pore diameter using the Tao-Eldrup model[27,30,31] (Figure 3.9), PALS is an ideal technique to

characterize changes in pore size or pore size distribution due to degradation by water. Water vapor can break down the coordination bonds in MOFs leading to local framework collapse.[32] As a result, the relative amount of intact framework pores will be reduced and this can be detected in the PALS spectrum as a decrease in the intensity of Ps annihilating in the framework pores (Ps with the characteristic framework lifetime). Therefore, PALS is well suited to monitor pore evolution of MOFs in real-time under humid conditions.

3.2 **Results and Discussion.**

When a steady nitrogen flow at 20 mL/min with 40% relative humidity at 25 °C is flowed through a bed of ~80 mg MOF-5, the Ps framework lifetime (representing the size of framework pores) decreases from 13.0 ns to 12.4 ns within the first 19 hours (green symbols in Figure 3.21). This slight decrease in Ps framework lifetime is consistent with some minimal accumulation of water molecules in the pores prior to their collapse. While the intensity of framework Ps, which indicates the relative population of intact framework pores in the material, decreases from 32% to 9%. This indicates that the typical MOF-5 crystals have only 28% of its original porosity remaining after 19 hours exposure to 40% relative humidity. The decrease in both Ps framework lifetime and Ps intensity correlates with the structural rearrangement/degradation of MOF-5. After the initial slight decrease, the Ps framework lifetime dramatically drops from 12.4 ns to 6.3 ns with wider error bars of ±2.1 ns, the Ps intensity keeps going downward from 9% to 0.15%, indicating that the MOF-5 framework collapses catastrophically. Based on the correlation between Ps framework lifetime (ns) and cubic pore side length (nm) (Figure 3.9), the aforementioned lifetime drop suggests that 40% relative humidity causes the size of MOF-5 framework cell changes from a uniform 1.3 nm to a collection of different sizes ranging from 1.02 nm to 0.69 nm at the end of the experiment. PXRD of MOF-5 after the 40% relative humidity exposure shows obvious structural transformation (Figure 3.11). The change of MOF-5 crystallinity reveals that the framework collapses and transforms into $ZnBDC \cdot xH_2O$ (BDC=benzene-1,4-dicarboxylate, where x is between 1 and 2) with little porosity.[32] The decrease of the framework intensity from 32% down to 0.15% is due to irreversible local cell collapse instead of water condensing and filling the

cells based on the BET surface area of MOF-5 after the 40% relative humidity exposure experiment (Figure 3.15). No amount of drying or gentle heating could recover the framework Ps signal.

Repeating the above experiment with a relative humidity of 30%, the Ps intensity and Ps framework lifetime do not change after 200 hours of exposure. The BET surface area of MOF-5 after 200 hours of 30% relative humidity treatment (red symbols in Figure 3.15) is very close to that of initially activated MOF-5 (black symbols in Figure 3.15). After 43 hours of exposure to 40% relative humidity, MOF-5 loses 99.5% of the framework pores, while no degradation is observed at 30% relative humidity. This difference in degradation behavior of MOF-5 under different humidities is not a dose effect. To illustrate this point Ps intensity (%) is plotted against total H_2O charged per mass of MOF (g/g) (Figure 3.20). With 5.94 g of H_2O charged per gram of MOF-5 under a relative humidity of 40%, corresponding to 43 hours of humidity treatment, the Ps intensity goes down to 0.15% (green symbols in Figure 3.20) indicating collapse of the lattice. Under a relative humidity of 30%, after a similar dose of H_2O charged per gram of MOF-5 (black symbols in Figure 3.20) which corresponds to 57.5 hours of humidity treatment, the Ps intensity stays around 32% and MOF-5 remains intact. Thus relative humidity, not water dosage, is key to the water degradation process.

To more precisely define the region of stability for MOF-5, a series of relative humidities were explored and the Ps intensity and Ps framework lifetimes collected. The framework intensities (Figure 3.3a) and framework Ps lifetimes (Figure 3.21) are plotted against flow time of the humid nitrogen with different relative humidities. For all cases the intensities of MOF-5 framework Ps follow a universal sigmoidal trend. The MOF-5 “half degradation time” defined as the number of hours required for the framework intensity to decrease to half of its original value shows a nominally exponential dependence on relative humidity as shown in Figure 3.3b. Once the time factor is removed by plotting Ps framework lifetime against framework intensity, the entire degradation processes coincide with each other (Figure 3.25). However, the lower the relative humidity, the longer time it takes for the Ps intensity to start to decay. It also shows that at 30% relative humidity, even after 189 hours of exposure to humidity, the Ps intensity is hardly altered (black symbols in Figure 3.3a), while for the same amount of

time, at a slightly higher relative humidity (34%) the Ps intensity already decreases to 11.5%, which correspond to 40% of the framework being damaged (red symbols in Figure 3.3a). The results imply that how early the framework degradation happens depends on the concentration of water (i.e relative humidity of gas flow) in stark contrast to the typical methods of degradation for water sensitive metal complexes. The higher the relative humidity, the longer MOF-5 has been exposed to the humidity, and the larger the amount of water the framework has been exposed to, the faster degradation occurs and proceeds.

An induction period manifested in the initiation phase of the sigmoidal degradation curve has been discovered, suggesting a relative humidity window for long-term stability for MOF-5. To further test this hypothesis, additional experiments were conducted to assess the long-term stability of MOF-5. Little change in powder X-ray diffraction patterns is seen after 6 months of exposure to humid air with relative humidity up to 11% (Figure 3.28). This indicates that in applications such as hydrogen storage, where the water concentration would be low, moisture instability is not a concern for MOF-5. This finding runs counter to countless assertions in the literature which, though perhaps intuitive, do not have any long term stability testing of relevance to support them.

There is a dramatic change in the stability of MOF-5 within a small window of relative humidity. Under a relative humidity of 36% (blue symbols in Figure 3.3a), the Ps intensity of MOF-5 framework was not observed to be reduced after 11 hours because there are few hydrophilic groups present in the intact MOF-5: all the carboxylate groups are coordinatively bonded to Zn_4O^{6+} metal clusters. At longer times, the Ps intensity decreases slowly. The reduction of Ps intensity accelerates progressively as the degradation proceeds and the amount of broken coordination bonds between linkers and metal clusters increases exposing more hydrophilic functional groups. This can be explained considering that the broken bonds from the decomposition reactions on the framework in turn promote the degradation of the crystal. Decomposition again slows down towards the end of the curve due to the shrinkage of the number of hydrolysis-prone spots in the framework at the end of the curve.

In light of these observations, we hypothesized that other MOFs based on the basic Zn_4O cluster might also have regions of stability under humid conditions. UMCM-8

is composed of $Zn_4O(CO_2R)_6$ metal clusters and a 1:1 ratio of the linear linkers benzene-1,4-dicarboxylate (BDC) and naphthalene-2,6-dicarboxylate (NDC). It has a structure similar to MOF-5 but instead of having cubic cages of a single size, it has two cubic cages and two tetragonal cages (Figure 3.1) and larger voids than MOF-5. The larger the pores, the longer the Ps framework lifetime (less rapid the Ps annihilation) because of the reduced overlap of the Ps wave function with the surrounding electrons of the pore walls. It is generally observed, within a homologous series, that MOFs with larger void spaces display less stability due to a tendency towards structural collapse.[33] On this basis the larger pores of UMCM-8 might be expected to engender reduced stability towards water. However, the degradation of UMCM-8 in fact requires higher relative humidity than MOF-5 (Figure 3.4a). At 36% relative humidity, conditions that can initiate the decomposition of MOF-5, does almost nothing to the Ps intensity （blue symbols in Figure 3.4a） or Ps framework lifetime (Figure 3.22) in UMCM-8 for 200 hours. The Ps framework lifetime of UMCM-8 remains at 16 ns which corresponds to an average pore diameter of 1.4 nm and Ps intensity stays at 32% which corresponds to an intact framework. When the relative humidity is increased to 44%, the Ps framework lifetime drops from 16 ns to 12 ns in 120 hours (pink symbols in Figure 3.22), the Ps intensity shows a sigmoidal trend similar to MOF-5. These results imply that with the same concentration of water, MOFs with same metal clusters but different pore sizes/hydrophilicity tolerate water vapor to different extent. In combination with recent studies demonstrating that more sterically demanding ligands improving kinetic stability towards humidity degradation[21,34], this suggests a two-fold approach to overcoming water instability for this large class of MOFs. The proposed explanation for the greater stability of UMCM-8 is that the attack of water on the MOF does not happen through interaction of a single water molecule with a metal cluster breaking/disturbing the interaction of the Zn-O tetrahedron. The size of the pore and the hydrophilicity of linkers play important roles as well. The hypothesis is that degradation must be triggered by a certain amount of accumulation of water in the pore, a mechanism similar to capillary condensation. The larger the inner diameter of the pore, the higher the partial pressure of water (relative humidity of gas stream in the present case) is needed to accumulate sufficient water

molecules to hydrolyze coordination bonds between linkers and metal ions. The hydrophilicity of linkers may also contribute to the stability difference between MOF-5 and UMCM-8. The computed logP (calculation see Supporting Information) value of benzene (1.97) is lower than that of naphthalene (2.96) which means that BDC is more hydrophilic than NDC. Even though a fraction of cages in UMCM-8 have the same size as MOF-5, UMCM-8 does not start degrading at the same time with MOF-5. This observation implies that the degradation of the series of Zn_4O-based MOFs does not start unless accumulation of water molecules takes place in multiple cages. Otherwise, UMCM-8 and MOF-5 should have started to decompose at the same relative humidity.

To further explore the factors dictating hydrolytic stability, the IRMOF $Zn_4O(FMA)_3$ was studied using the same approach with PALS under 30% relative humidity and the results compared to MOF-5 (Figure 3.5). This material, reported by Chen and coworkers, is constructed from the $Zn_4O(CO_2R)_6$ metal clusters and fumarate linkers; it is among the smallest pore members of the IRMOF series. The logP value of ethene is 1.11 suggesting that fumarate is much less hydrophobic than either BDC or NDC. Moreover, with a theoretical cage side-length of 1.08 nm, $Zn_4O(FMA)_3$ is smaller than MOF-5 and therefore can shed light upon the issue of pore size in promoting decomposition (framework Ps lifetime of 8.9 ns vs. 13.5 ns for MOF-5). In Figure 3.5, the framework porosity of $Zn_4O(FMA)_3$ is severely reduced under the conditions of 30% relative humidity-the Ps intensity decreases to 0% within 6 hours whereas MOF-5 shows almost no reduction in framework intensity even after 200 hours under these conditions. The BET surface area of as-synthesized $Zn_4O(FMA)_3$ is 2009 m^2/g (previously reported: 1120 m^2/g; theoretical surface area: 2835 m^2/g, see Supporting Information) whereas after hydration, its BET surface area decreases to 30 m^2/g (Figure 3.17). Based on the fact that the Ps framework intensity of $Zn_4O(FMA)_3$ decreases by an absolute value of 1.7% after 45 h of 16% relative humidity treatment and keeps decreasing slowly with time, the relative humidity region of water stability for $Zn_4O(FMA)_3$ is much lower than that of MOF-5 and UMCM-8 (Figure 3.27). The comparison of the region of water stability for $Zn_4O(FMA)_3$, MOF-5 and UMCM-8 illustrates the range of different behaviors that can be seen for hydrocarbon linkers within the same basic coordination motif and suggests larger pores lead to greater resistance to hydrolysis.

The functionality of linkers can influence water stability of Zn_4O-based MOFs. Hydrophilic functional groups are expected to reduce water stability. Aniline, the core of the linker yielding IRMOF-3, has a logP of 1.14, a value lower than 1.97 for benzene due to the presence of the $–NH_2$ group. It has been reported that IRMOF-3 is more stable than MOF-5 in ambient air.[35] However, continuous monitoring of porosity by PALS indicates that IRMOF-3 is in fact more sensitive to humidity than MOF-5. Figure 3.6 plots the intensity of Ps annihilating inside the IRMOF-3 crystals as a function of exposure time for various values of relative humidity. This intensity is the sum of the intensity of Ps annihilating in surviving pristine lattice (Ps lifetime=8-10.3 ns) and the intensity of Ps (Ps lifetime =13-28 ns) trapped in larger voids generated near regions of lattice collapse, representing all Ps annihilating inside the IRMOF-3 crystals. The fitted framework lifetime is reduced because of the additional effect of it disappearing into the intermediate component. At short exposure times, this trapped void component is impossible to resolve because its Ps lifetime is very close to the pristine lattice Ps lifetime and its intensity is very low. At long exposure times, this void component grows in to comprise ~2/3 of the (decaying) residual total intensity with lifetimes that range from 17 ns for 20% relative humidity to 28ns for 30% relative humidity (corresponding to void diameters of 1.7 nm and 2.2 nm, respectively). The sum of intensities plotted in Figure 3.6 is robust and nominally corresponds to the relative residual porosity as plotted in Figure 3.3a and Figure 3.4a.

The black symbols in Figure 3.6 shows that the Ps intensity of IRMOF-3 drops dramatically within 24 hours of exposure to 30% relative humidity in a quasi-exponential fashion; this shape contrasts dramatically with the sigmoidal shapes seen in the MOF-5 and UMCM-8 experiments. The Ps intensity of IRMOF-3 then stabilizes around 7%. The differences in water stabilities and degradation trends between IRMOF-3 and MOF-5 are attributable to the fact that the linker of IRMOF-3, 2-aminoterephthalate, has a higher water affinity than the linker of MOF-5 and, perhaps more critically, the water-induced decomposition product of IRMOF-3 is amorphous whereas it is crystalline for MOF-5. There is no apparent induction period for the degradation of IRMOF-3 exposed to 30% relative humidity; this suggests that the hydrophilic nature of the functional groups, and the perhaps even the participation of these groups in decomposition, eliminates the need

for clusters of water molecules and existing framework damage. The rate of degradation decreases over time as a result of the loss in the number of intact pores although the fact that the damage levels out suggests that the decomposition process is somewhat self-protective of inner porosity.

Under a lower relative humidity of 24%, the degradation of IRMOF-3 caused by water follows the same trend as described above although the Ps intensity stabilizes at a higher level, around 16% after 70 hours (pink symbols in Figure 3.6). Red symbols in Figure 3.31 shows the relative intensity of the peak at $2\theta=6.86°$ in IRMOF-3 PXRD patterns changing with time under 30% relative humidity. The intensity of the primary PXRD peak at $2\theta=6.86°$ goes down quickly to 0.4% of the original intensity and then plateaus which agrees with how the porosity changes based on Ps intensity information (black symbols in Figure 3.31). With a relative humidity of 24%, the intensity of the primary peak in IRMOF-3 PXRD patterns decreases and plateaus around 33% of the original intensity, which is in accord with Ps intensity trend as well (Figure 3.32). These experiments demonstrate that the porosity evolution is correlated with the evolution of crystallinity. This can be explained by a model wherein IRMOF-3 degrades into an amorphous phase with no new crystallinity appearing (Figure 3.18) and the amorphous continuous layer protects the interior crystalline material from further contact with water, a mechanism analogous to self-protective oxide formation in certain metals. In contrast to MOF-5, which transforms into another crystalline phase ($ZnBDC \cdot xH_2O$)[32] upon water exposure apparently with gaps for water to pass through and continue degradation the remaining MOF-5, IRMOF-3 acts differently upon encountering water. The observation of a preservation of the bulk crystal morphology of IRMOF-3 in previous studies[36] also supports a mechanism where protection by an amorphous layer for the IRMOF-3 prevents complete loss of crystallinity. All the curves asymptotically approach equilibrium framework intensities that are stable at the given relative humidities and are lower as the humidity increases.

Water-induced decomposition in MOFs leads to higher sensitivity to humidity. To illustrate this point, MOF-5 was treated for 100 hours with 36% relative humidity at 20 mL/min until the Ps framework intensity decreased to 13% (a 60% reduction from the

pristine material). The humidity was then decreased to 30%. Unlike the almost unchanged framework intensity of pristine MOF-5 treated with 30% relative humidity right from the beginning (black symbols in Figure 3.7), the framework intensity of damaged MOF-5 now decreases much more rapidly, at a rate of 0.068% Ps framework intensity per hour. This is slow compared to 0.49% per hour before the switch (Figure 3.7) but there is clearly no induction period at the 100 hour turning point of relative humidity. This indicates that the defects created by water lead to faster degradation kinetics. In other words the history of the sample, in terms of previous exposure to moisture, influences the amount of defects in the MOF and therefore the time required for degradation at a given humidity.

3.3 **Conclusions**

PALS incorporated within a flow-through system allows monitoring structural degradation of MOFs in real-time under dynamic humid conditions. For MOF-5 and UMCM-8, the evolution rate of porosity depends sensitively (exponentially) on relative humidity and proceeds by a universal sigmoidal decrease. This indicates that the damage mechanism(s) and evolution of structure are the same under different relative humidities. An induction period consistent with exponentially long MOF degradation has been revealed for a group of MOFs with $Zn_4O(CO_2R)_6$ metal clusters. Controlling the relative humidity, even over a fairly large and operationally relevant window, allows for long-term stability of these MOFs against water vapor. The water stability of Zn4O-based MOFs with cubic structure was found to be related to pore size and linker hydrophilicity, as demonstrated by comparison of the behavior of UMCM-8, MOF-5, $Zn_4O(FMA)_3$ and IRMOF-3. These results deepen the understanding of the stability of MOFs against water and demonstrate that water stability is strongly dependent on relative humidity such that appropriate process parameters can be chosen for long term stability in applications such as fuel gas storage, separations, and catalysis.

3.4 Experimental Methods

3.4.1 Synthesis of MOFs

$Zn_4O(FMA)_3$[23], MOF-5,[24] UMCM-8[16] and IRMOF-3[37] were synthesized and activated using previously reported methods. The BET surface areas and pore volumes were calculated from N_2 sorption isotherms at 77K and given in Table S1.[38,39]

3.4.2 PALS Incorporated with Flow-through System

The apparatus has been designed and built to get the desirable result of *in situ* porosity of MOFs under humidity treatment. N_2 (extra dry purity 99.98%) was purchased from Cryogenic Gasses and used as received. GFC Mass flow controllers are purchased from Aalborg with a flow rate range from 0 to 20 mL/min and calibrated to N_2. H_2O bubbler was designed and constructed in-house to have gas dispersion tube and 100 cm of water. Needle valve is to purge the system and protect sample with dry N_2 when needed. The four-way valve switches between mixed humid N_2 and dry purging N_2. The two ball valves and MOF sample holder can be detached from the system and brought to glovebox for sample loading. The humidity sensors are placed before and after MOF sample to monitor the relative humidity of inlet and outlet N_2 streams. The PALS spectrometer is a typical start-stop ^{22}Na coincidence system using 5.08 cm diameter fast plastic scintillators and constant fraction timing discriminators. With the discriminator levels set for maximum count rate the system time resolution is observed to be 290 ps.

3.4.3 Fresh and Post-Hydration-PALS MOFs Analyzed by PXRD

Samples of each material were coated in mineral oil, then loaded onto a CryoLoop™ and mounted onto a Rigaku R-axis Spider diffractometer with an image plate detector and graphite monochromated Cu-Kα radiation (λ= 1.54187 Å). Images were collected at room temperature for 5 minutes in transmission mode with χ set at 45°, φ rotating at 10°/sec and ω oscillating between 80° and 140° at 1°/sec. Integration of the resulting images was performed in the AreaMax software package (version 2.3.8., Rigaku 2008). Images were integrated from 2.5° to 50° with a 0.01°step size using AreaMax software package (version 2.3.8., Rigaku 2008). Powder patterns were processed using JADE Plus v9.5 and OriginLab 8.6.

The Crystallographic Information File (CIF) files used to simulate powder patterns are obtained from the Cambridge Crystallographic Data Centre. All patterns have been normalized to match maximum counts to clearly show the crystallinity of MOF samples after each hydration-PALS experiment.

3.4.4 Initial Activated and Post-Hydration-PALS MOFs Analyzed by N_2 Adsorption Measurement

N_2 adsorption isotherms were measured by a volumetric method at 77 K on a NOVA 4200 by Quantachrome Instruments (Boynton Beach, Florida, USA). Ultra-high purity N_2 (99.999%) was purchased from Cryogenic Gasses and used as received. The relative pressure ranges for calculating the surface area satisfy the criteria for applying BET theory.[40] The fitting correlation coefficients ≥ 0.9999.

3.4.5 Positronium framework intensity of MOF-5 as a function of total H_2O charged per MOF

$$\text{Total } H_2O \text{ charged per MOF} = \frac{\text{Absolute humidity} \times \text{Flow rate} \times \text{Time}}{\text{Mass of MOF}}$$

$$\text{Absolute humidity} = \frac{6.112 \times e^{\frac{17.67 \times T}{T+243.5}} \times \frac{Relative\ humidity}{100\%}}{RT} \times M.W.of\ water$$

Water vapor is considered as ideal gas. The ideal gas equation PV=nRT is applied.

3.4.6 LogP Calculation- Comparison of Linker Hydrophobicity

The partition coefficient is a ratio of concentrations of an un-ionized compound in the two phases of immiscible solvents (water and n-octanol) at equilibrium. logP is the 10-base logarithmic measure of the coefficient. The lower the value of logP the more hydrophilic the solute is. For instance, The computed logP value of benzene (1.97) is lower than that of naphthalene (2.96) which means that benzene is more hydrophilic than naphthalene.

$$\log P = \log\left(\frac{[solute]_{octanol}}{[solute]_{unionized\ water}}\right)$$

3.4.7 Long-Term Water Stability Experiments of MOF-5

In a typical experiment, 50 mg of as-synthesized and activated MOF-5 was loaded in a 4 mL small vial. The small vial was then quickly put inside a 20 mL scintillation vial with 2 mL of saturated salt solution to provide an environment with a specific relative humidity (Figure 3.28). Salt LiCl, $CaBr_2$, LiI, $CaCl_2$ saturated salt solutions were used to provide 11%, 17%, 18% and 32% relative humidity at 23 °C, respectively. A small amount of the solid as initially activated, after 1 month, 3 months and 6 months was transferred to mineral oil, grinded into powder and analyzed by powder X-ray diffraction.

3.4.8 Calculation of Theoretical BET Surface Area of $Zn_4O(FMA)_3$

The crystallographic information of $Zn_4O(FMA)_3$ (XOZXOA.cif) was obtained from the Cambridge Crystallographic Data Centre. Removal of solvent molecules (bound and free), addition of hydrogen atoms and geometry optimization (Forcite module, Quality: Ultra-fine, Forcefield: Universal) were carried out in Material Studio (v5.5.3) prior to theoretical BET surface area calculation from the model structure using the accessible surface area method established by Snurr and co-workers[41].

3.5 Figures

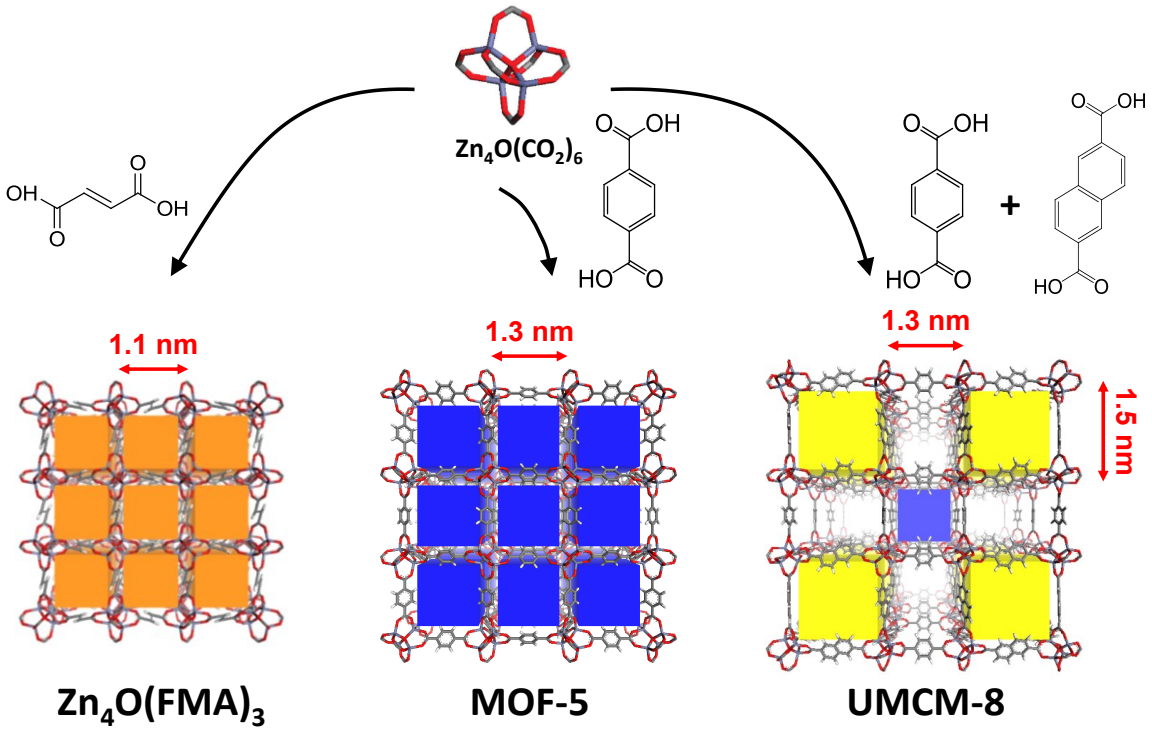

Figure 3.1 Compositions and structure comparison of $Zn_4O(FMA)_3$ (Zn_4O(fumarate)$_3$), MOF-5 (Zn_4O(benzene-1,4-dicarboxylate)$_3$), UMCM-8 (Zn_4O(benzene-1,4-dicarboxylate)$_{1.5}$(naphthalene-2,6-dicarboxylate)$_{1.5}$). The accessible cubic pore spaces are depicted by colored cubes. The cage metrics are marked accordingly.

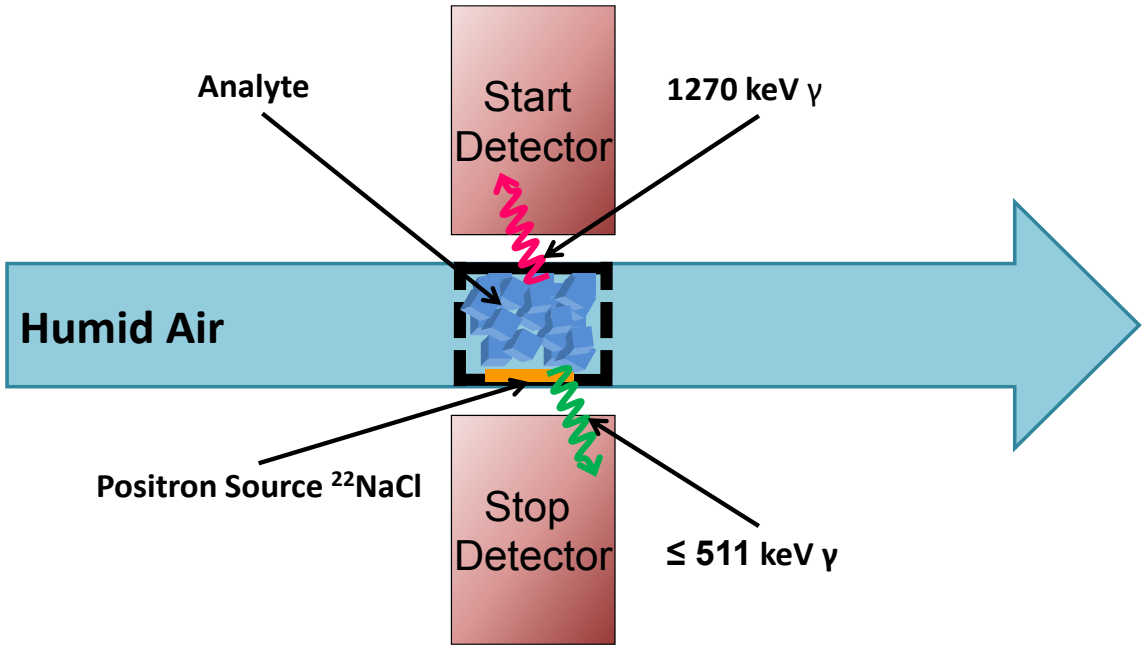

Figure 3.2 Illustration of the flow-through PALS apparatus.

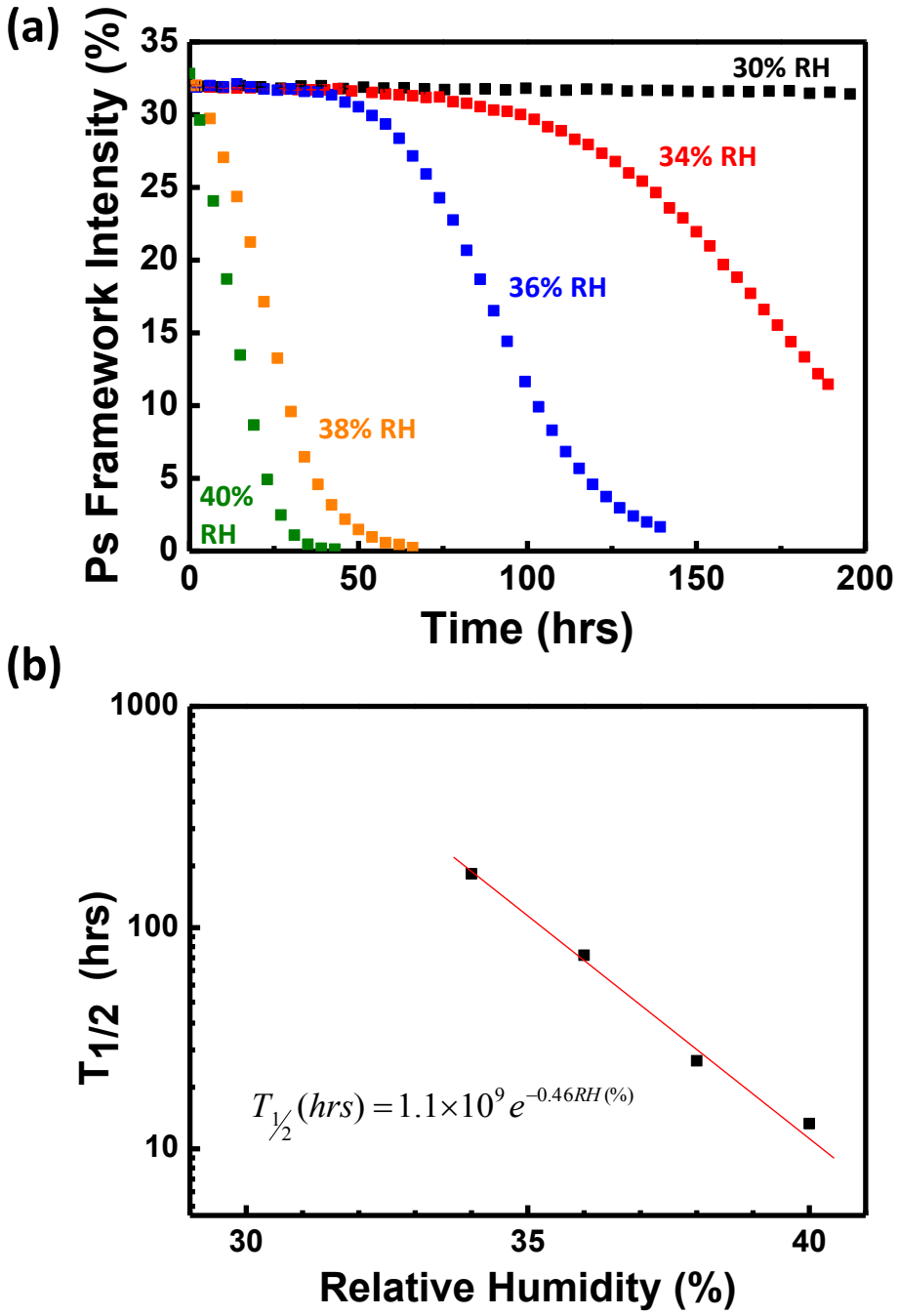

Figure 3.3 (a) Ps framework intensity of MOF-5 against time (hours) under the relative humidities (RHs) of 30% (black), 34% (red), 36% (blue), 38% (orange) and 40% (green) at 25 °C. (b) The time required for the Ps framework intensity to decrease to half its starting value ($T_{1/2}$) as a function of relative humidity.

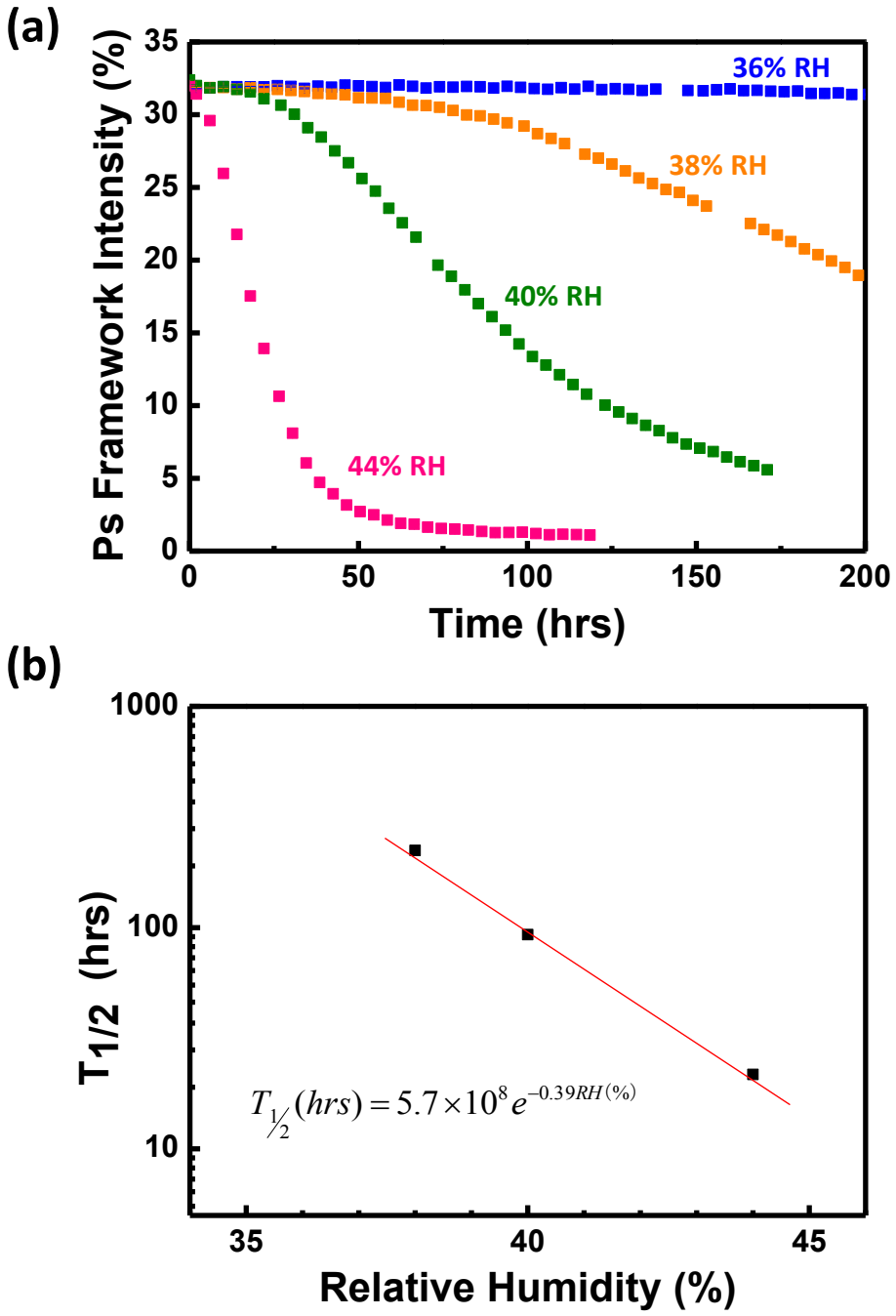

Figure 3.4 (a) Ps framework intensity of UMCM-8 as a function of time under the relative humidities (RHs) of 36% (blue), 38% (orange), 40% (green) and 44% (pink) at 25 °C. (b) The correlation between half degradation time ($T_{1/2}$) of UMCM-8 and relative humidity.

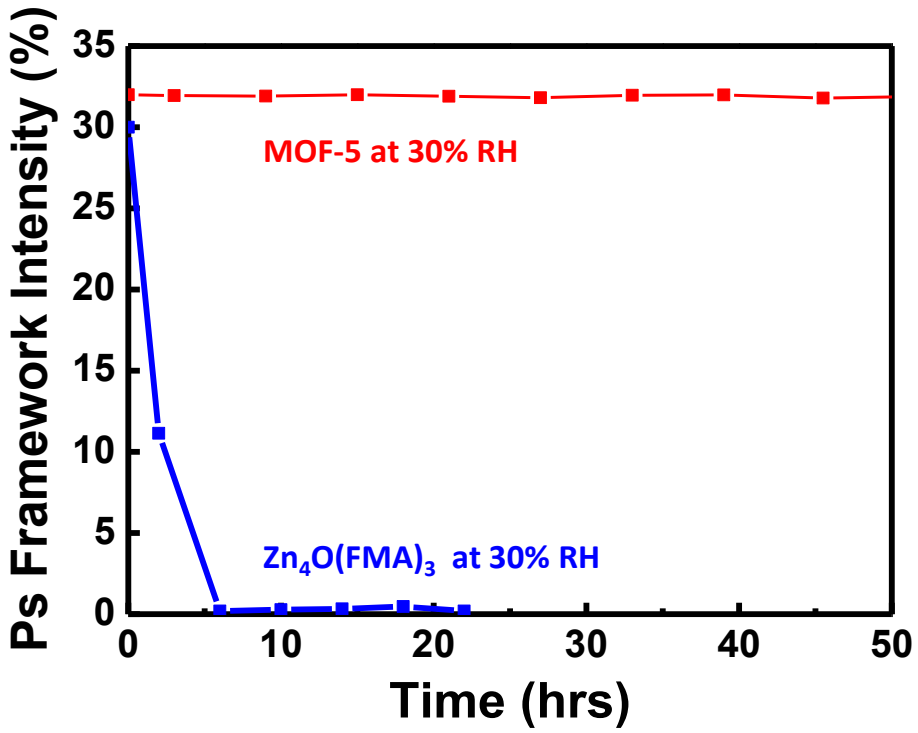

Figure 3.5 Comparison of Ps framework intensities between $Zn_4O(FMA)_3$ (blue) and MOF-5 (red) at 30% relative humidity (RH) at 25 °C.

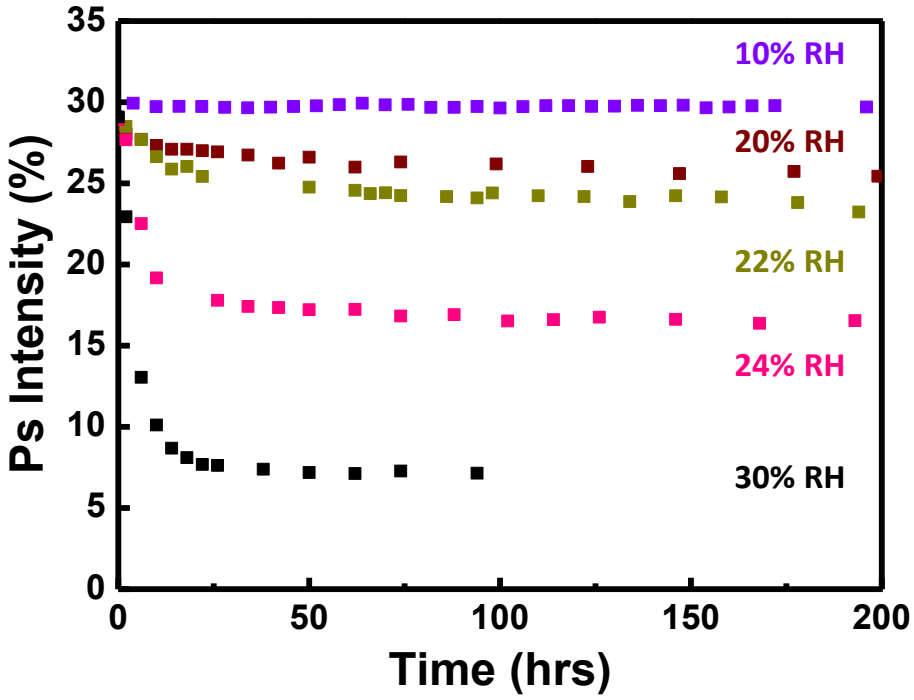

Figure 3.6 Ps intensity of IRMOF-3 against time under the relative humidities (RHs) of 10% (violet), 20% (burgundy), 22% (dark yellow), 24% (pink) and 30% (black) at 25 °C.

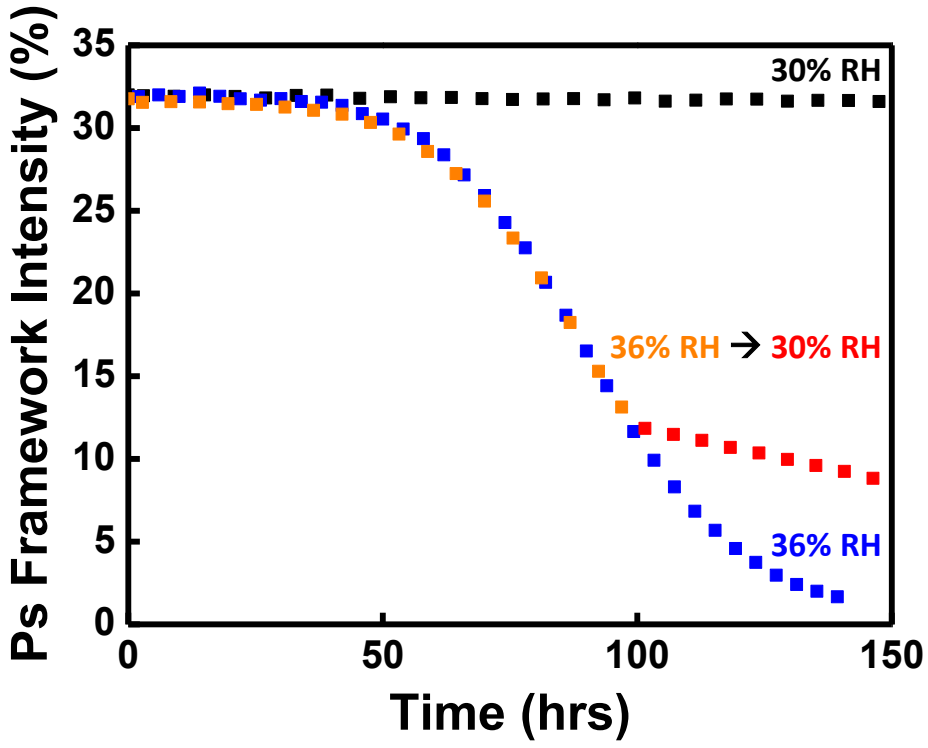

Figure 3.7 Ps framework intensity of MOF-5 against time under the relative humidities of 36% (orange) then 30% (red) at 25 °C. Ps framework intensities of MOF-5 under the relative humidity of only 36% (blue) and only 30% (black) are plotted for comparison.

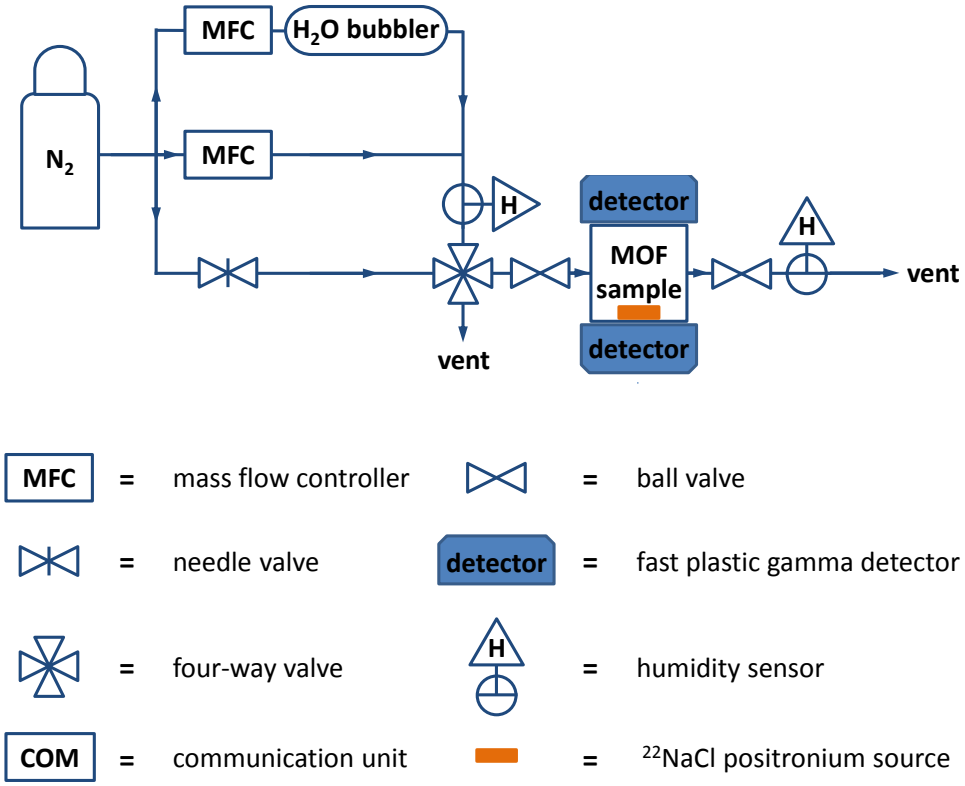

Figure 3.8 Block flow diagram of PALS flow-through system.

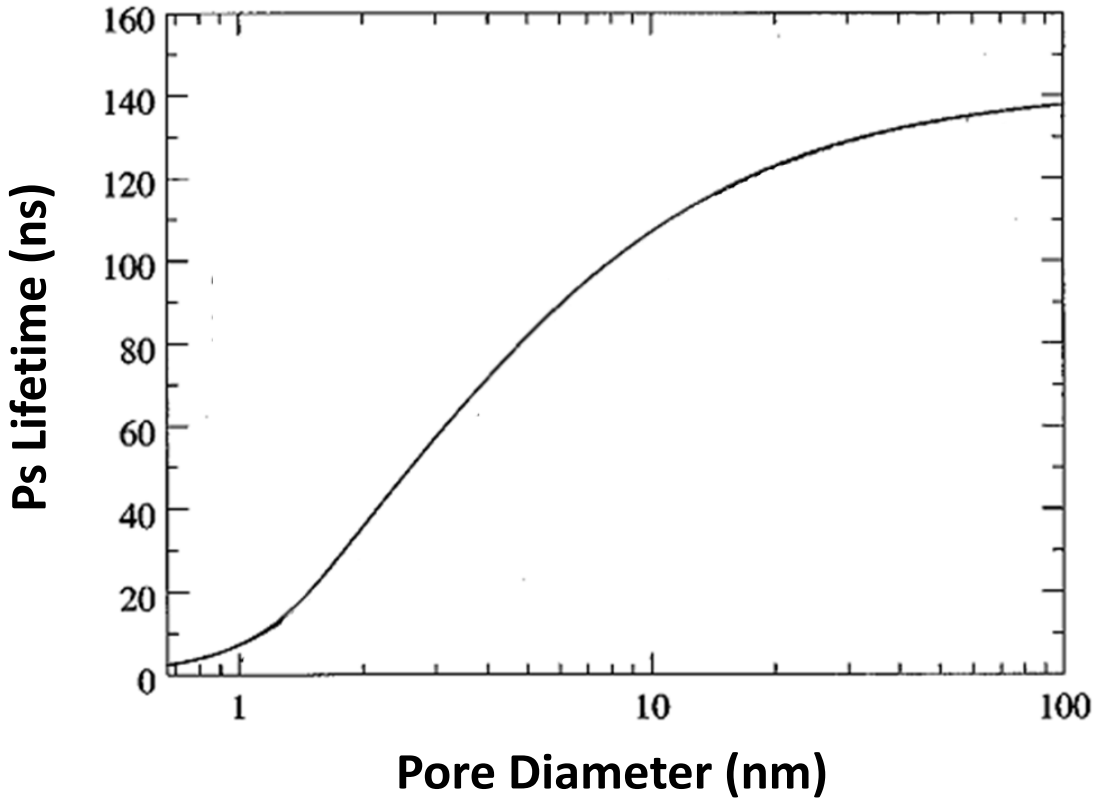

Figure 3.9 Theoretical correlation between Ps lifetime (ns) and pore diameter (nm) for the temperature of 298K. Reprinted with permission from Ref [27].

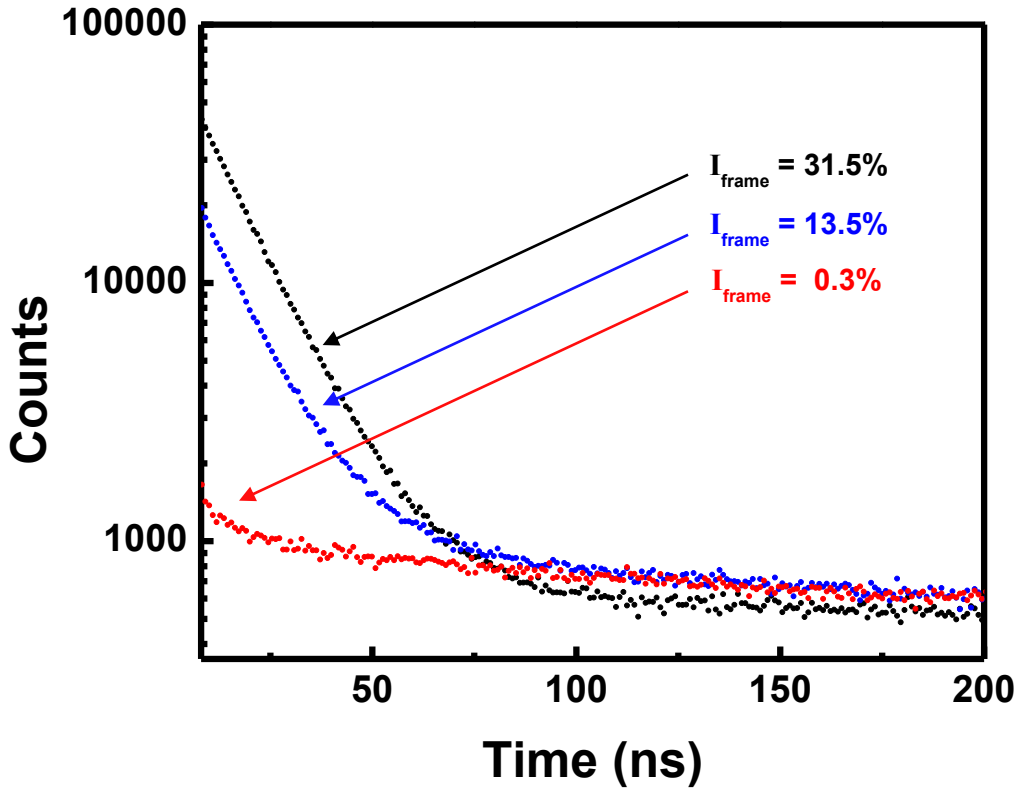

Figure 3.10 Typical PALS lifetime histograms for MOF-5 exposed to 38% relative humidity (RH) at three different points in the RH-induced degradation process: early in the induction period (black with no decrease in the Ps framework intensity); just past the 50% decay time (blue); and almost completely collapsed (red). The prompt peak of positron decays at t=0 is, for clarity, not shown, nor is it fitted in the data analysis. The data shown for t>8 ns are fitted for Ps lifetime components plus a constant background of uncorrelated events (~500 counts).[27,28]

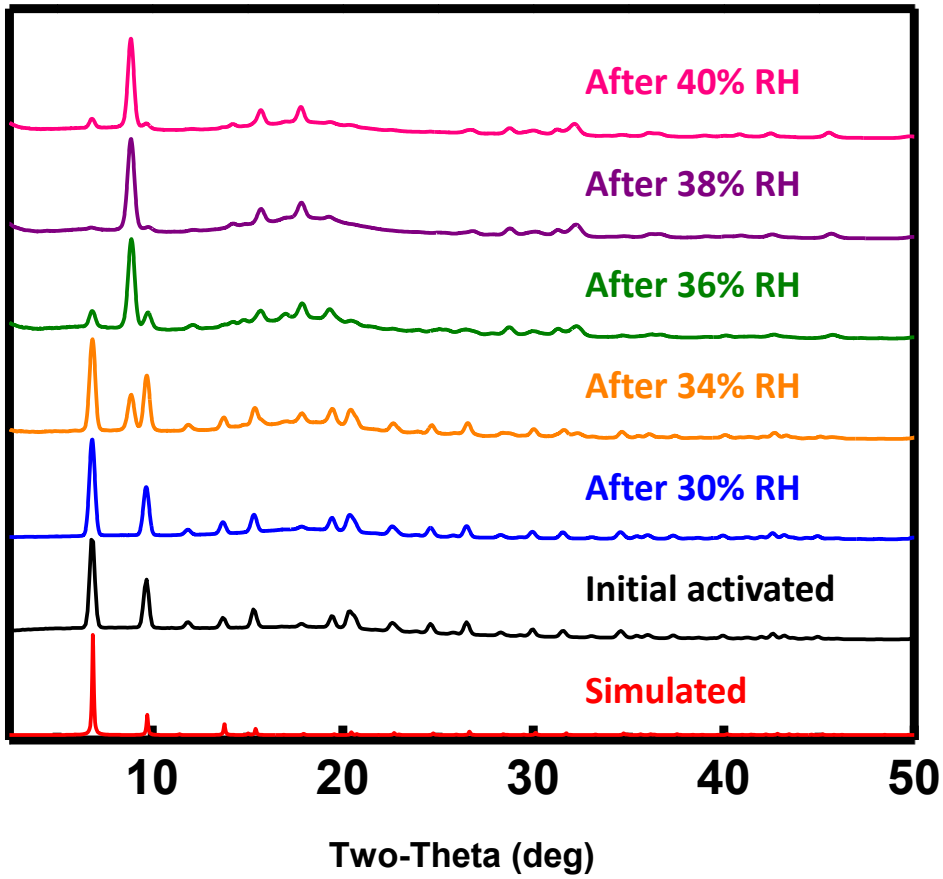

Figure 3.11 Overlay of PXRD patterns of simulated (SAHYIK.cif), initial activated MOF-5, and MOF-5 after hydration-PALS experiments at 30% relative humidity, 34% relative humidity, 36% relative humidity, 38% relative humidity and 40% relative humidity.

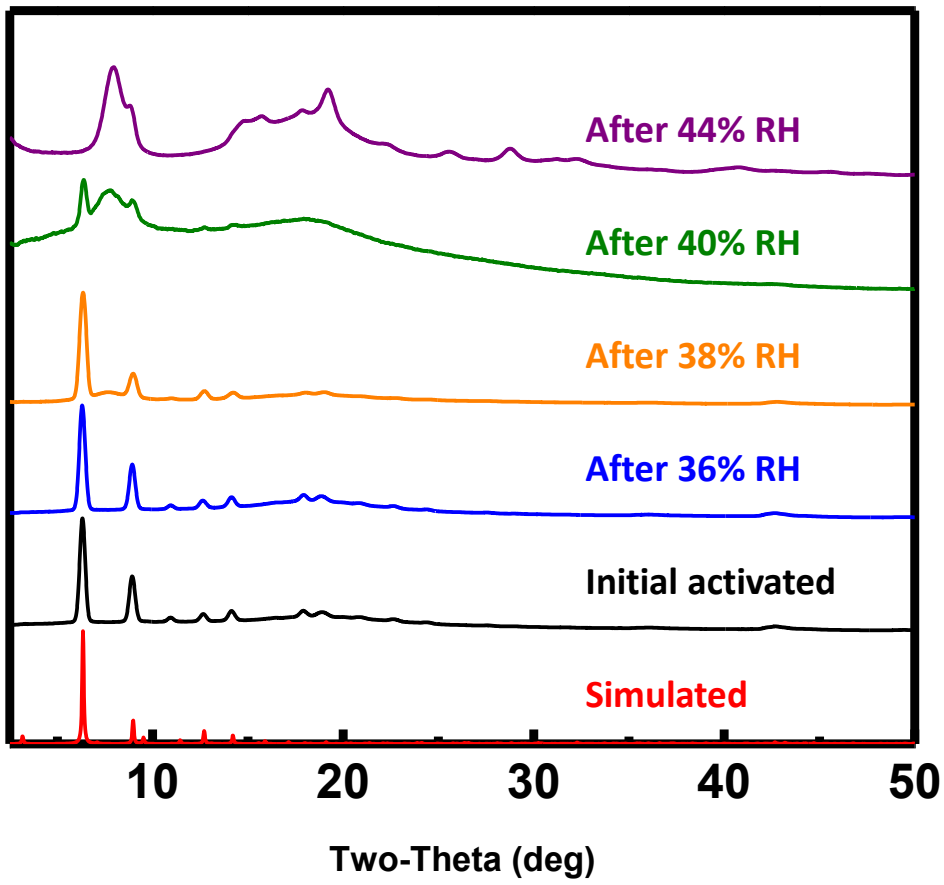

Figure 3.12 Overlay of PXRD patterns of simulated[25], fresh UMCM-8, and UMCM-8 after hydration-PALS experiments at 36% relative humidity, 38% relative humidity, 40% relative humidity and 44% relative humidity.

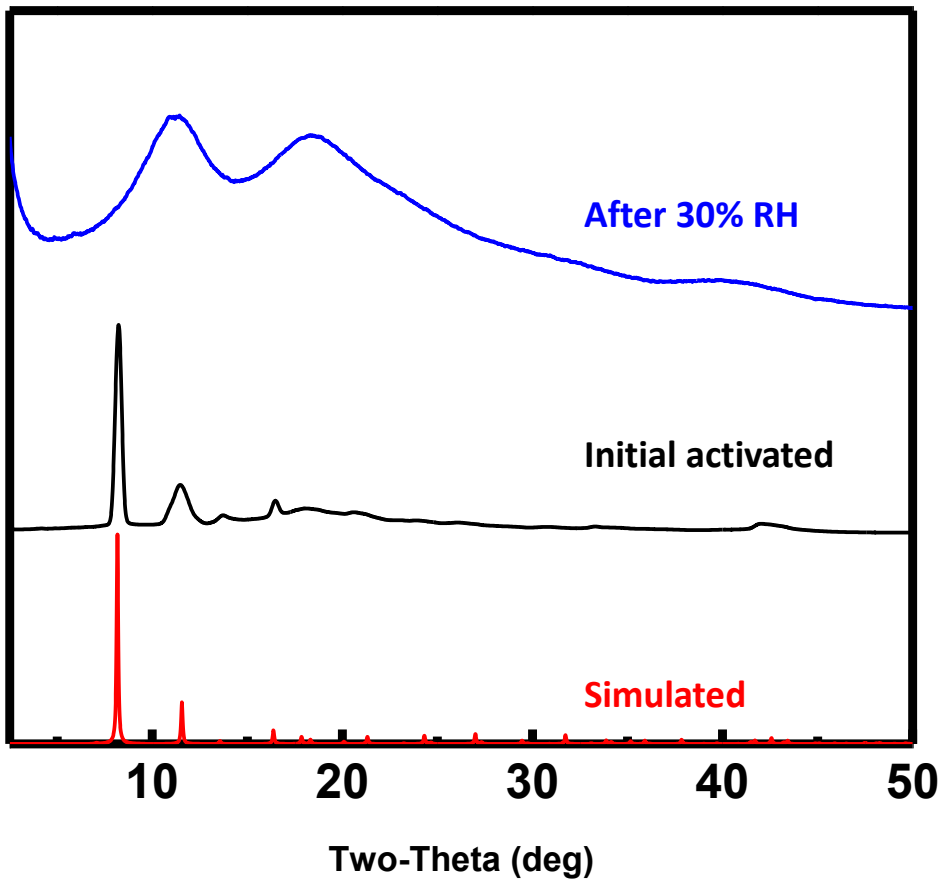

Figure 3.13 Overlay of PXRD patterns of simulated (XOZXOA.cif), initial activated Zn4O(FMA)3, and Zn4O(FMA)3 after hydration-PALS experiments at 30% relative humidity.

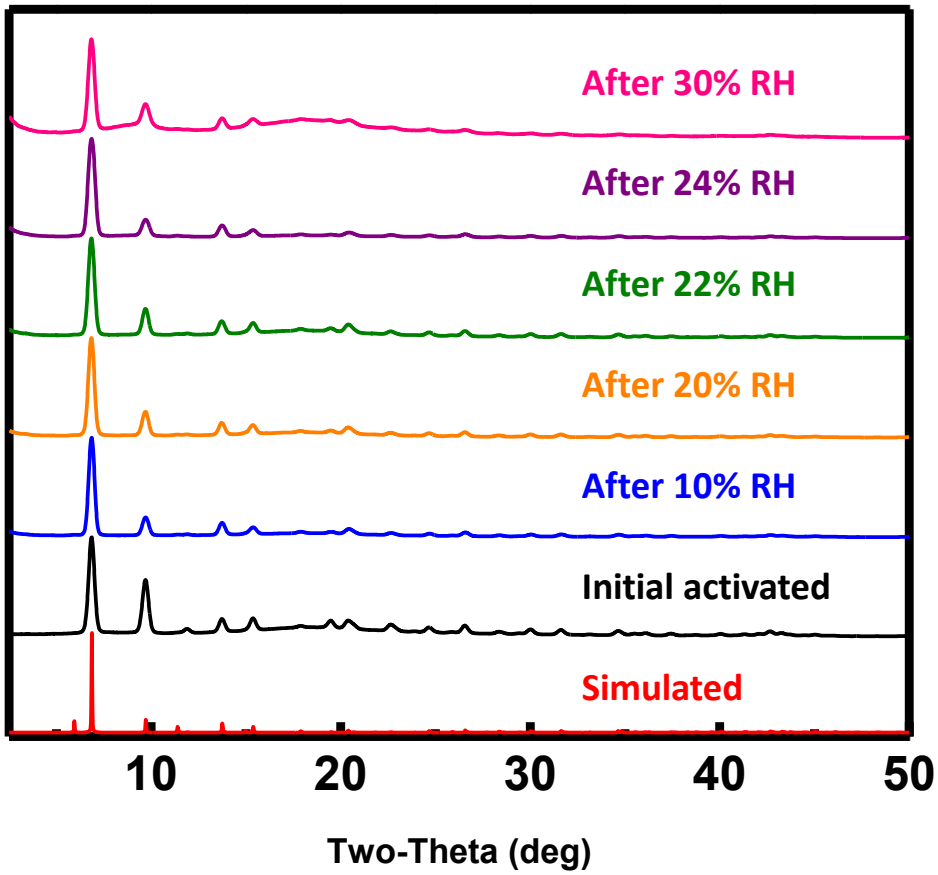

Figure 3.14 Overlay of PXRD patterns of simulated (EDUSUR.cif), initial activated IRMOF-3, and IRMOF-3 after hydration-PALS experiments at 10% relative humidity, 20% relative humidity, 22% relative humidity, 24% relative humidity and 30% relative humidity.

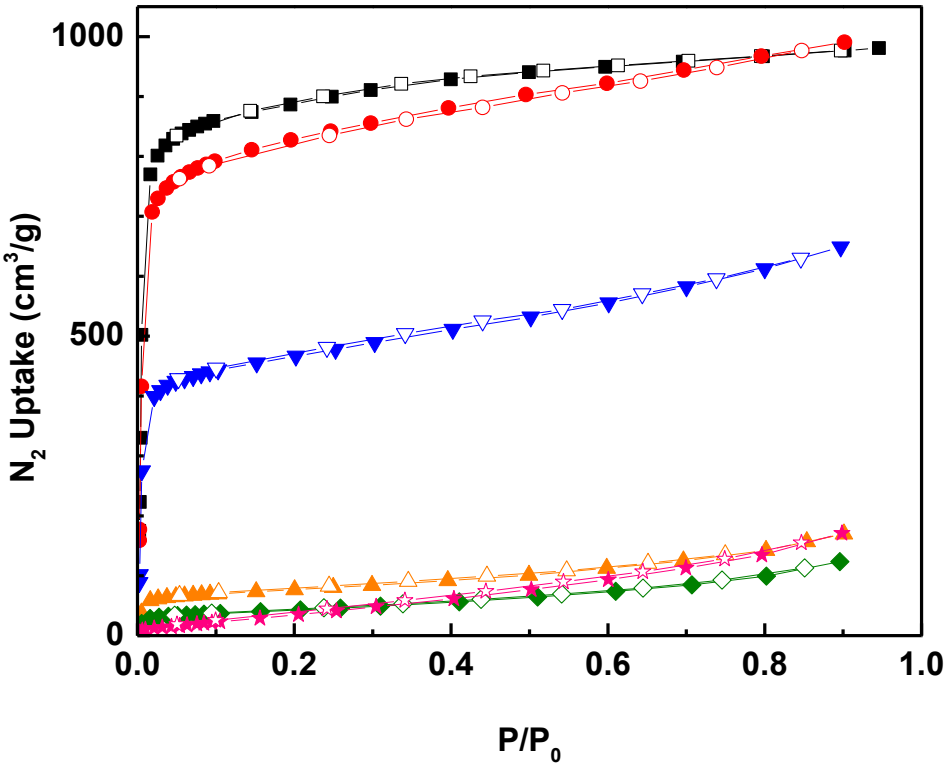

Figure 3.15 Overlay of N_2 sorption isotherms of initial activated MOF-5 (black, BET SA=3425 m^2/g) and MOF-5 after hydration-PALS experiments at 30% relative humidity (red, BET SA=3131 m^2/g), 34% relative humidity (blue, BET SA=1777 m^2/g), 36% relative humidity (orange, BET SA=278 m^2/g), 38% relative humidity (green, BET SA=148 m^2/g), and 40% relative humidity (pink, BET SA=63 m^2/g).

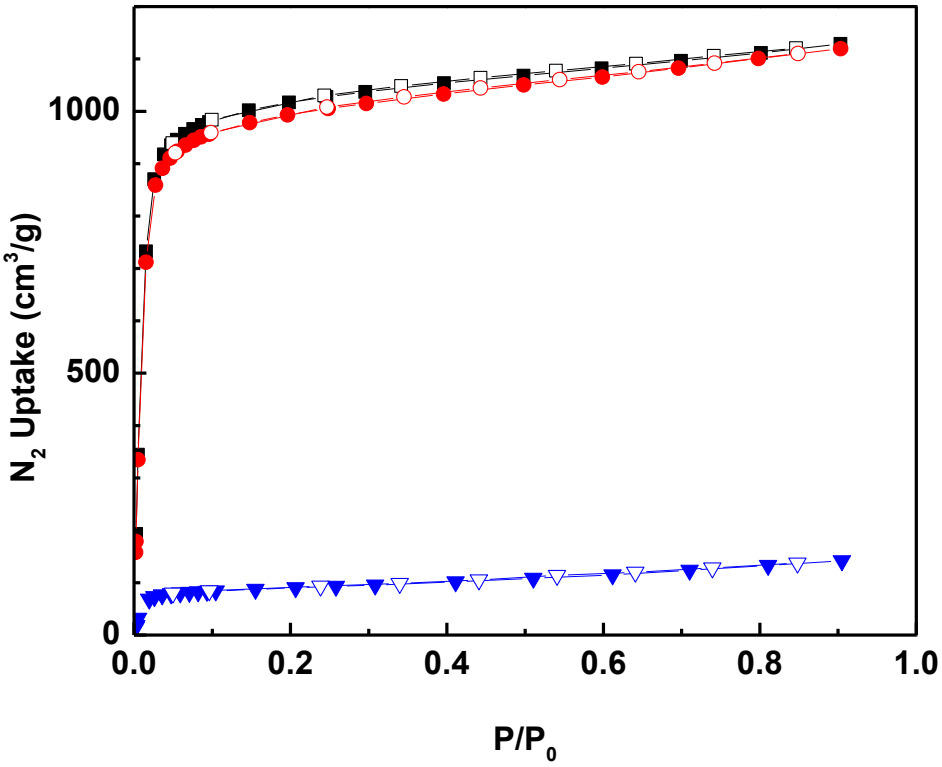

Figure 3.16 Overlay of N_2 sorption isotherms of initial activated UMCM-8 (black, BET SA=3893 m^2/g), and UMCM-8 after hydration-PALS experiments at 36% relative humidity (red, BET SA= 3884 m^2/g), and 44% relative humidity (blue, BET SA=330 m^2/g).

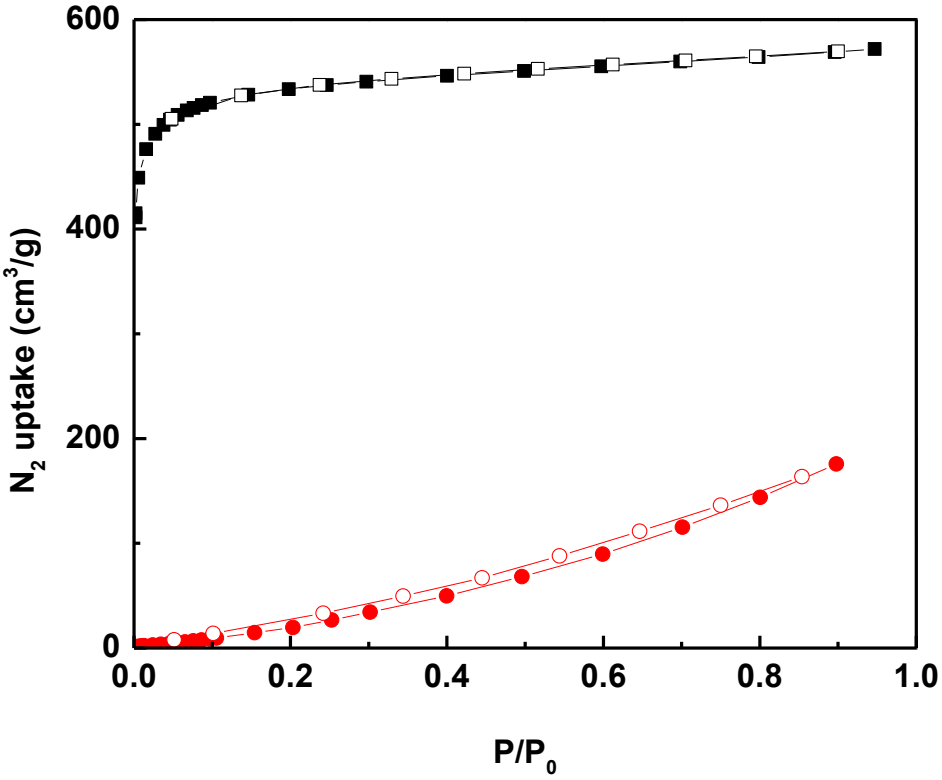

Figure 3.17 Overlay of N_2 sorption isotherms of initial activated $Zn_4O(FMA)_3$ (black, SA=2009 m^2/g), and $Zn_4O(FMA)_3$ after hydration-PALS experiments at 30% relative humidity (red, SA=30 m^2/g).

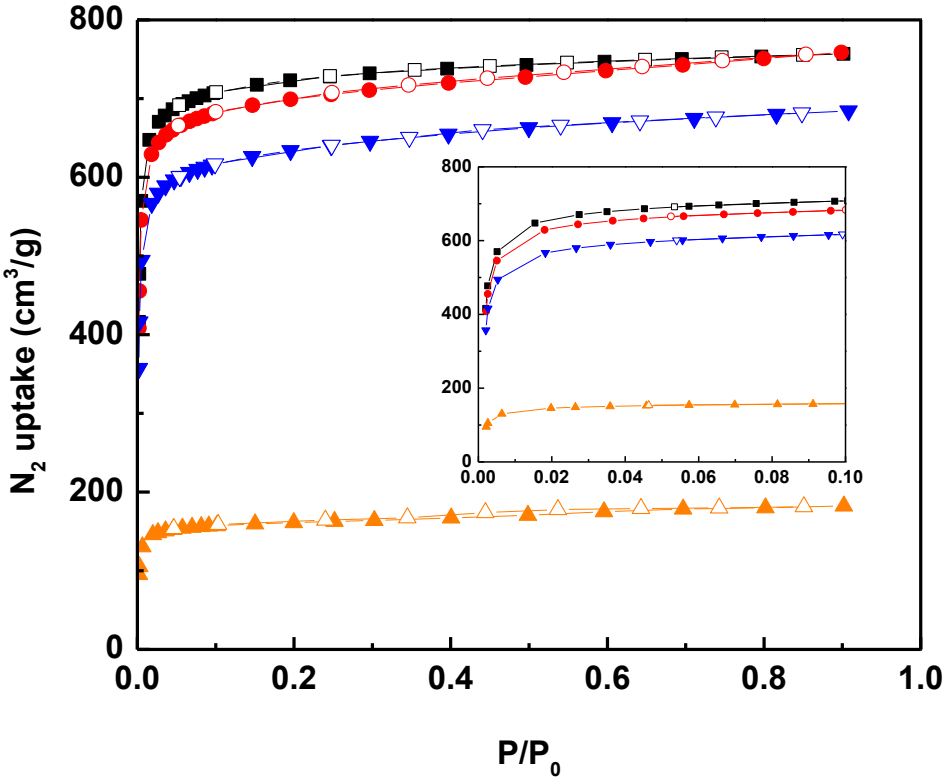

Figure 3.18 Overlay of N_2 sorption isotherms of initial activated IRMOF-3 (black, BET SA=2788 m^2/g), and IRMOF-3 after hydration-PALS experiments at 10% relative humidity (red, BET SA=2778 m^2/g), 20% relative humidity (blue, BET SA=2383 m^2/g), and 30% relative humidity (orange, BET SA=626 m^2/g). All isotherms are type I.

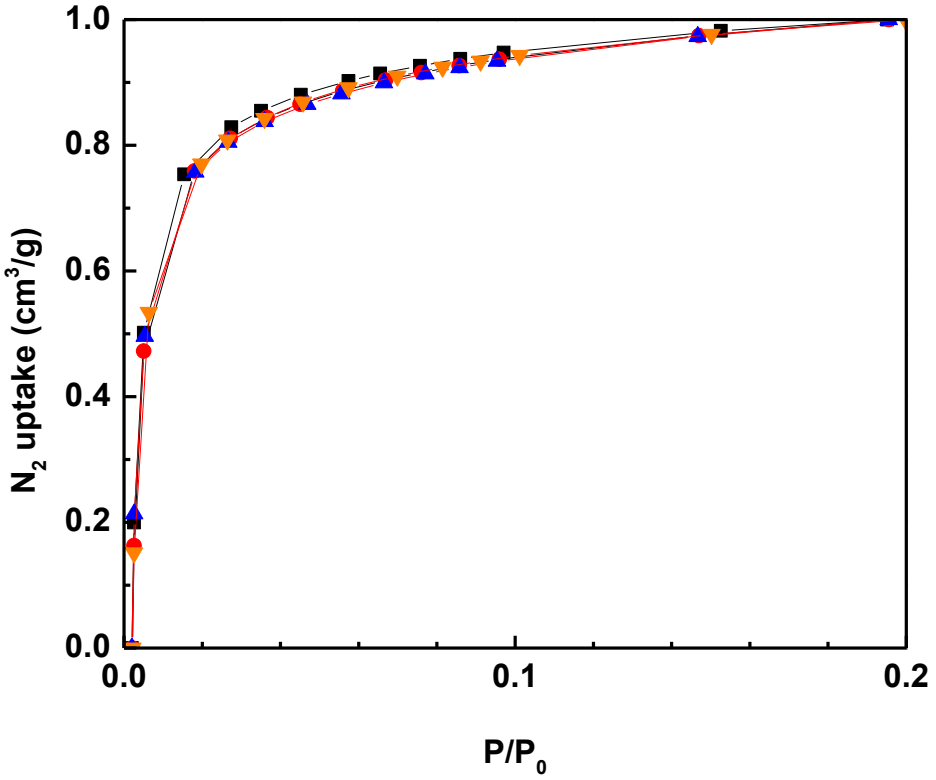

Figure 3.19 Overlay of normalized N_2 sorption isotherms of initial activated IRMOF-3 (black, BET SA=2788 m^2/g), and IRMOF-3 after hydration-PALS experiments at 10% relative humidity (red, BET SA=2778 m^2/g), 20% relative humidity (blue, BET SA=2383 m^2/g), and 30% relative humidity (orange, BET SA=626 m^2/g). Adsorption behaviors for all the samples are identical.

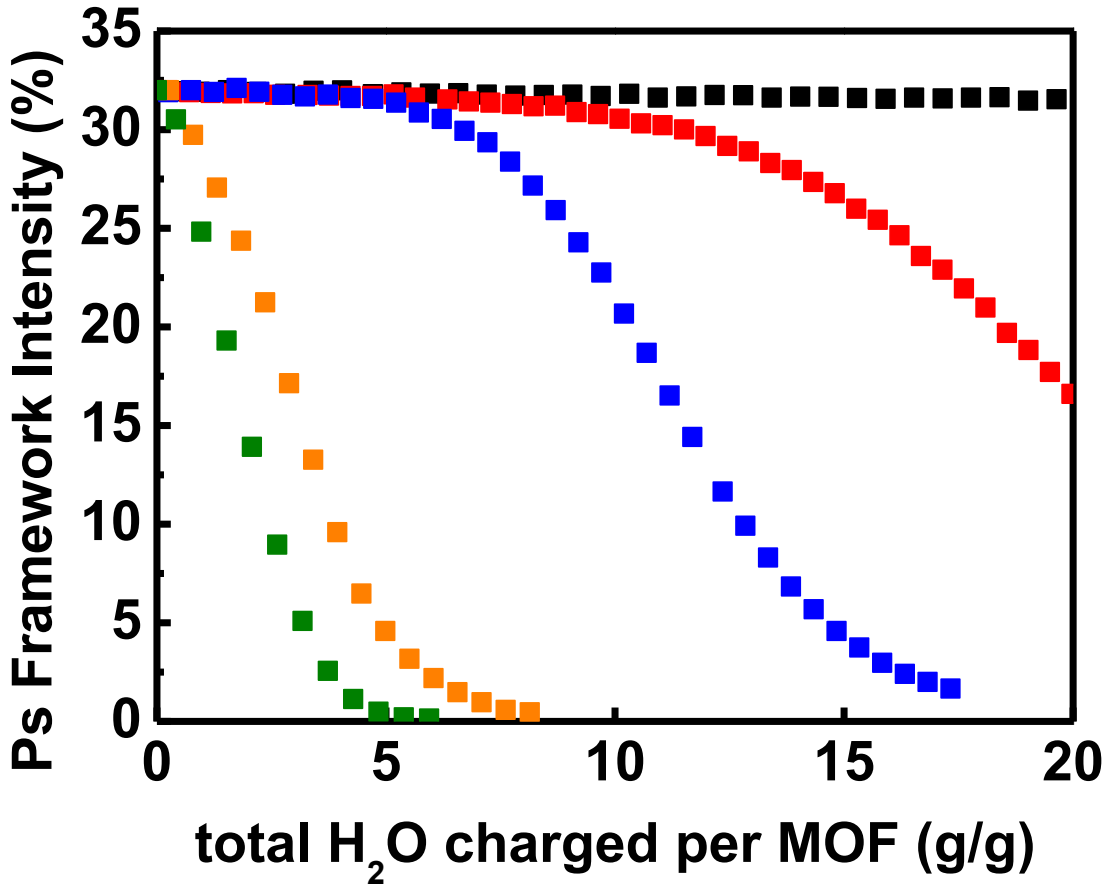

Figure 3.20 Ps framework intensity of MOF-5 against total water charged per MCP (g/g) under the relative humidities of 30% (black), 34% (red), 36% (blue), 38% (orange) and 40% (green) at 25 °C.

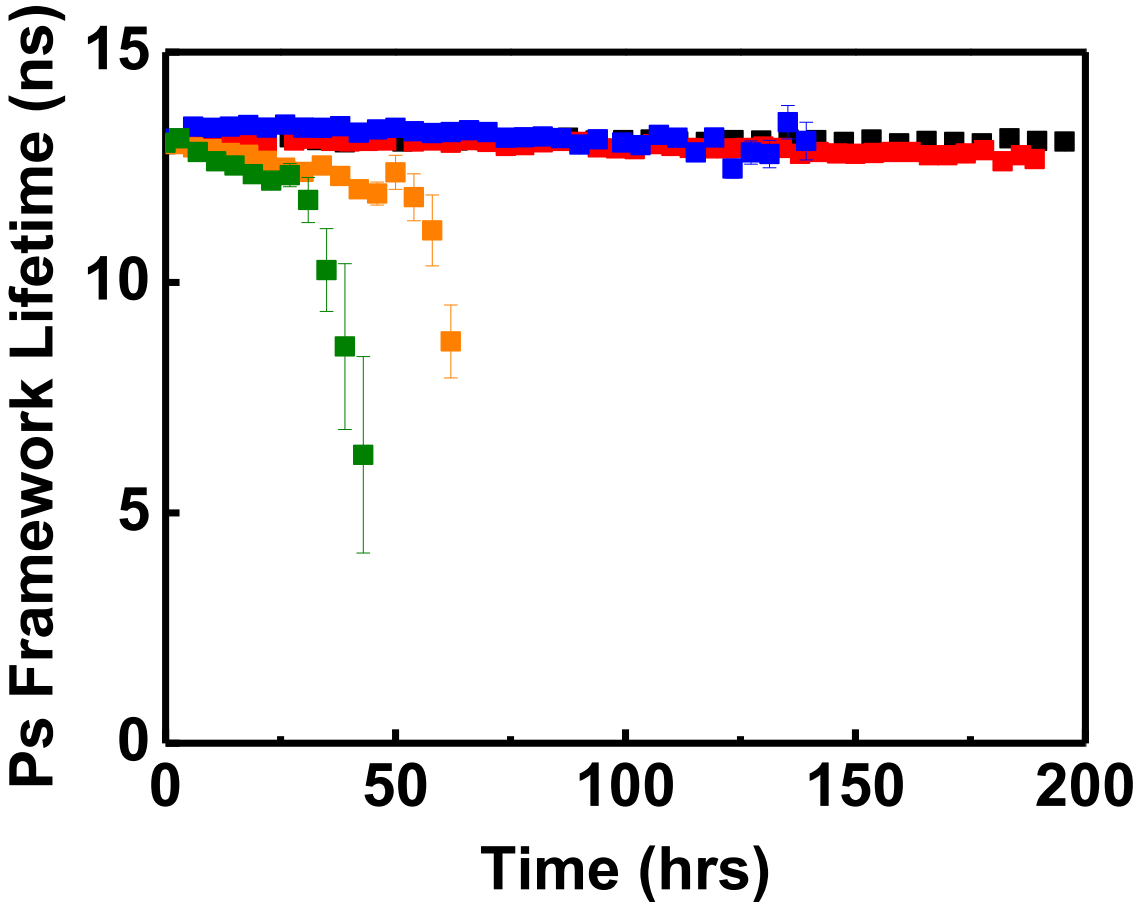

Figure 3.21 Ps framework lifetime (ns) of MOF-5 against time (hrs) under the relative humidities of 30% (black), 34% (red), 36% (blue), 38% (orange) and 40% (green) at 25 °C.

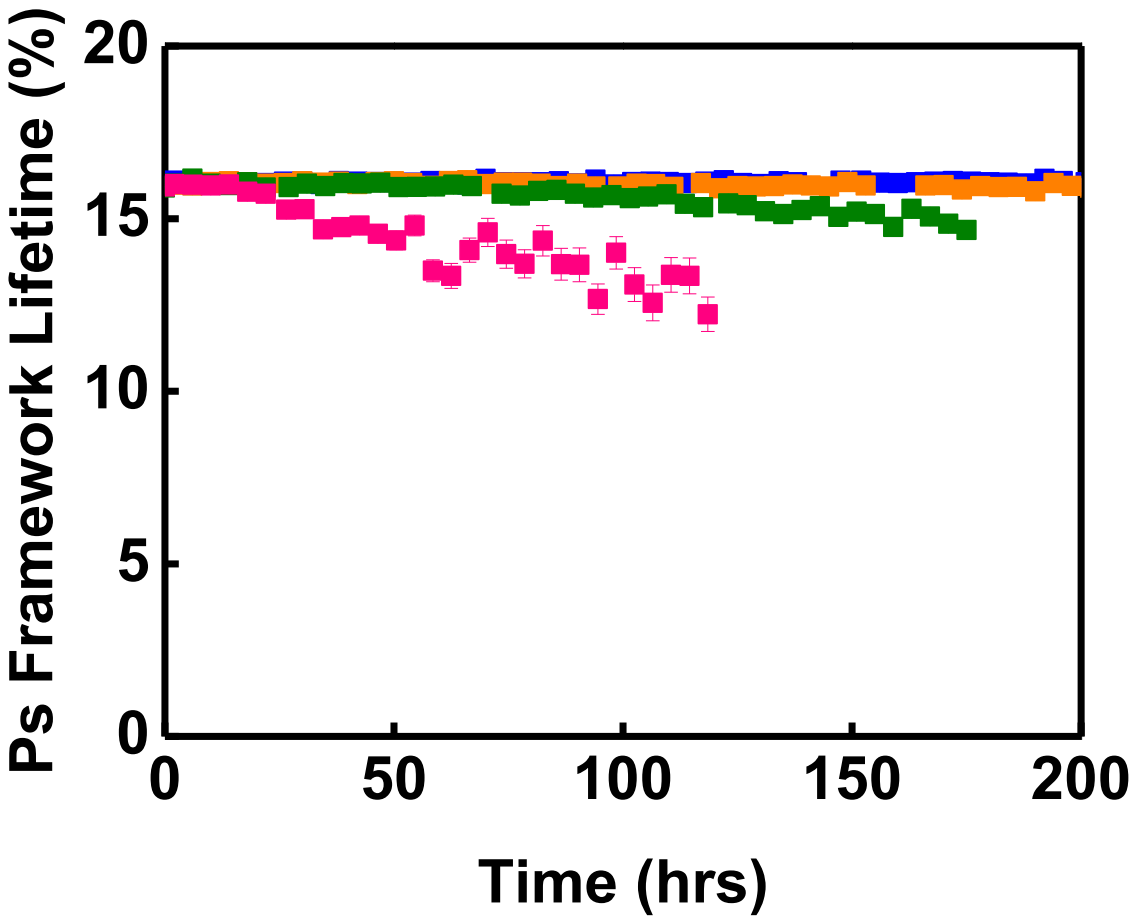

Figure 3.22 Ps framework lifetime (ns) of UMCM-8 against time (hrs) under the relative humidities of 36% (blue), 38% (orange), 40% (green) and 44% (pink) at 25 °C.

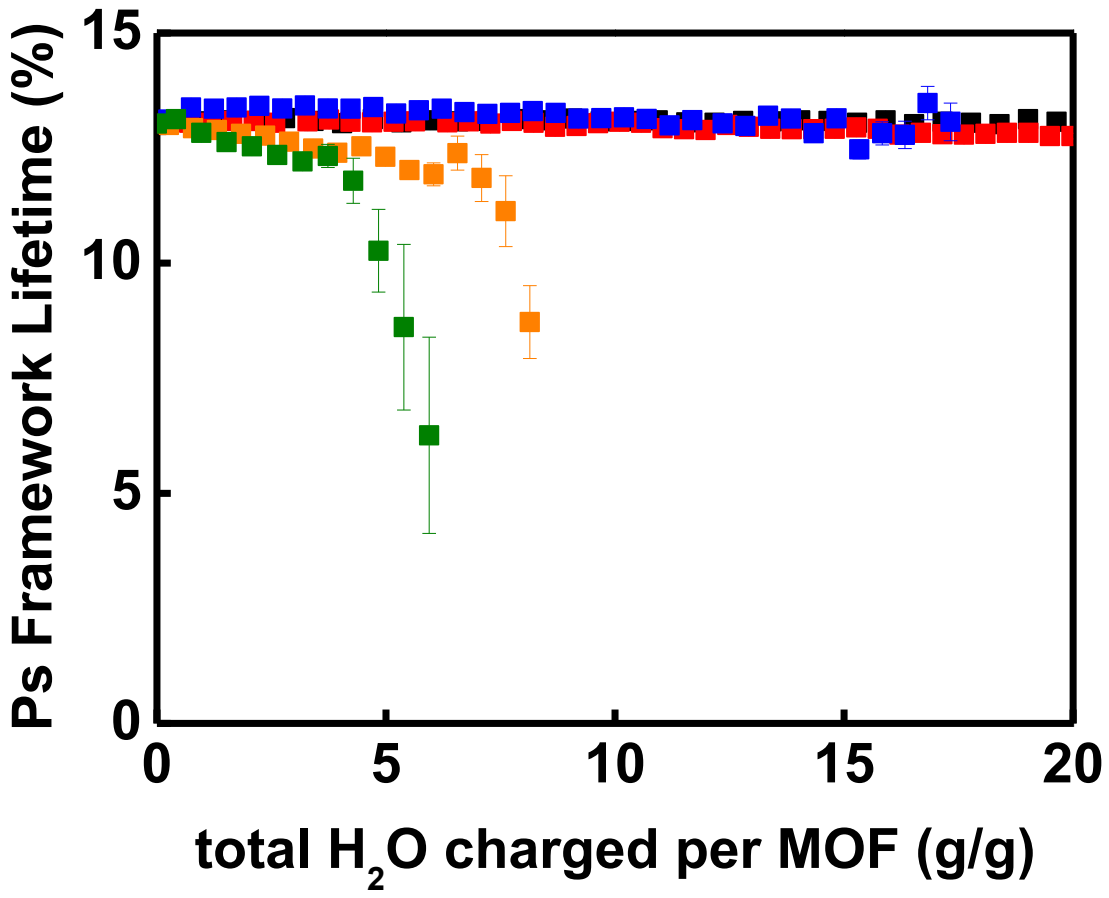

Figure 3.23 Ps framework lifetime (ns) of MOF-5 against total water charged per MCP (g/g) under the relative humidities of 30% (black), 34% (red), 36% (blue), 38% (orange) and 40% (green) at 25 °C.

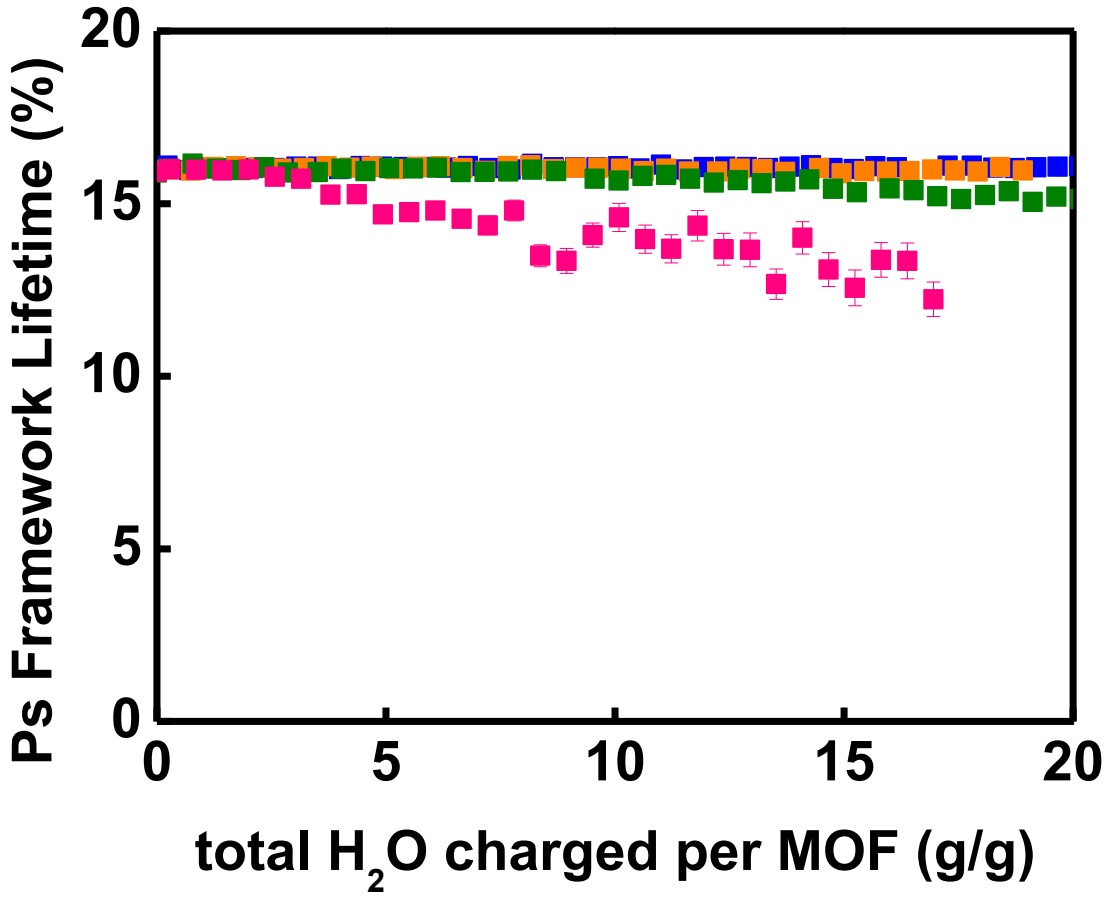

Figure 3.24 Ps framework lifetime (ns) of UMCM-8 against total water charged per MCP (g/g) under the relative humidities of 36% (blue), 38% (orange), 40% (green) and 44% (pink) at 25 °C.

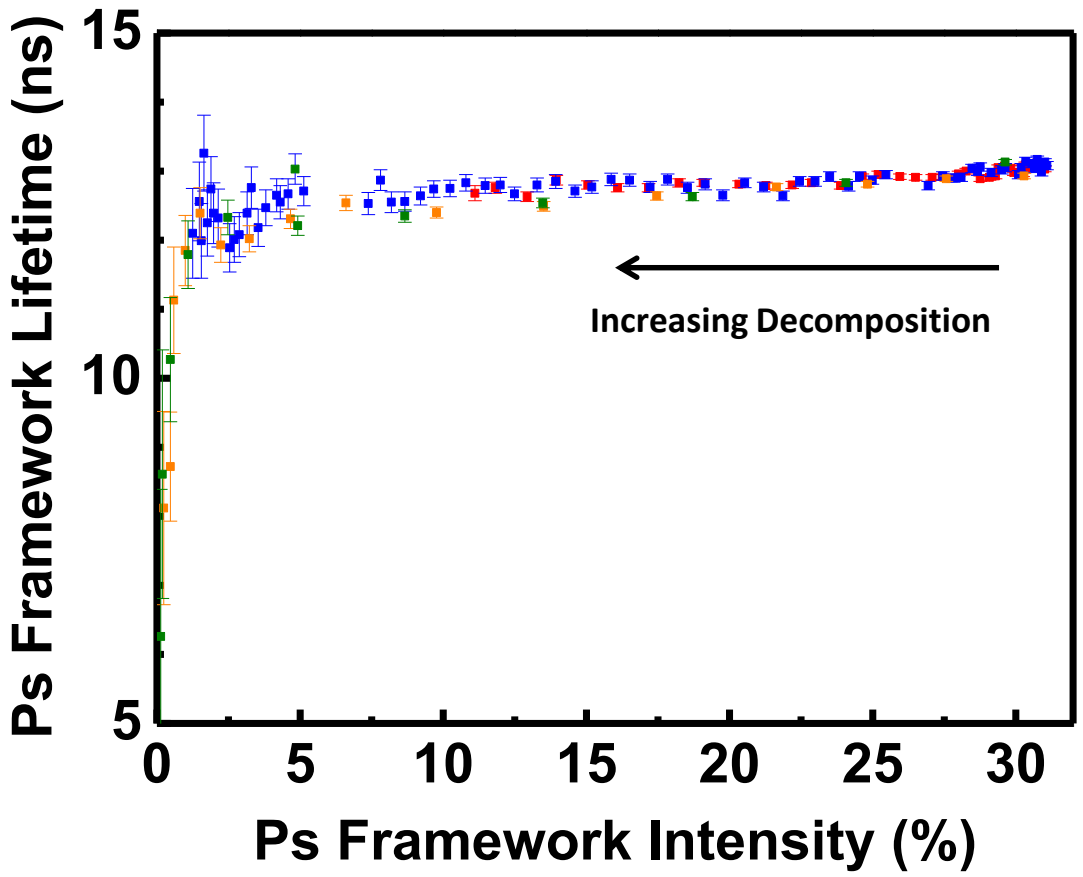

Figure 3.25 Ps framework lifetime of MOF-5 as a function of Ps framework intensity under the relative humidity of 34% (red), 36% (blue), 38% (orange) and 40% (green) at 25 °C.

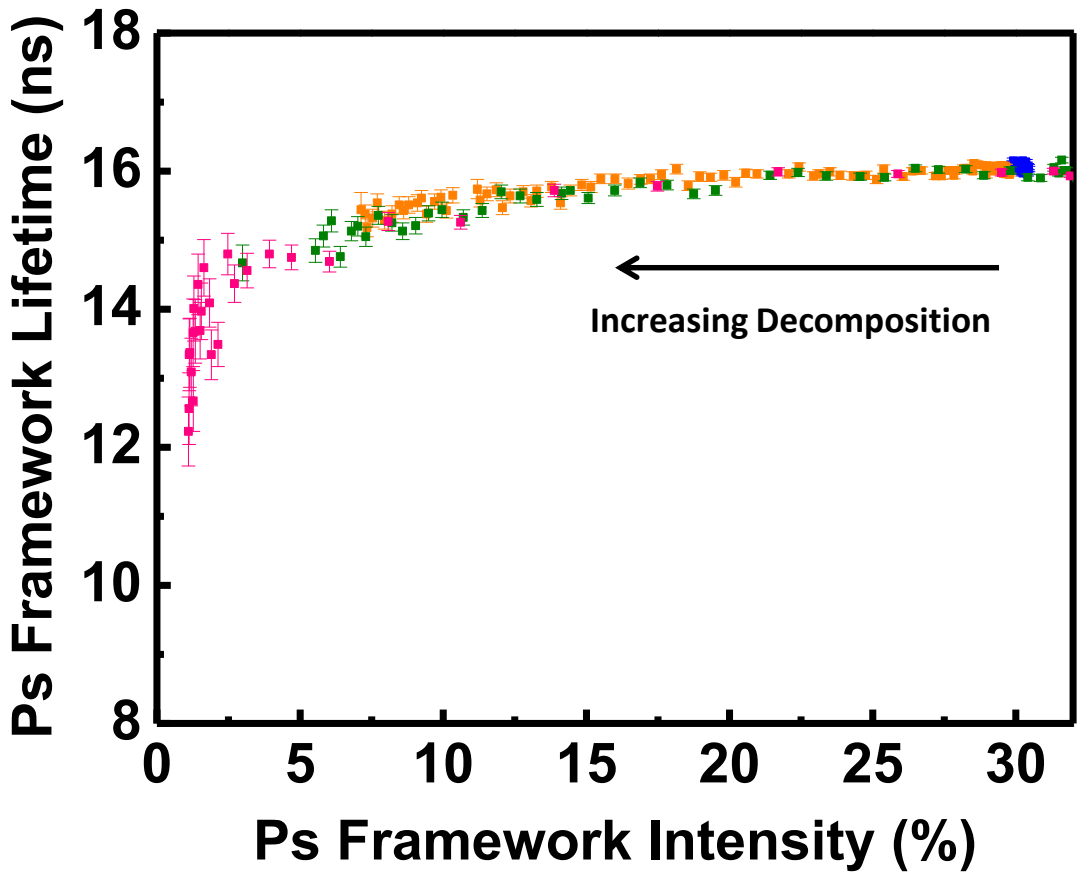

Figure 3.26 Ps framework lifetime of UMCM-8 as a function of Ps framework intensity under the relative humidities of 36% (blue), 38% (orange), 40% (green) and 44% (pink) at 25 °C.

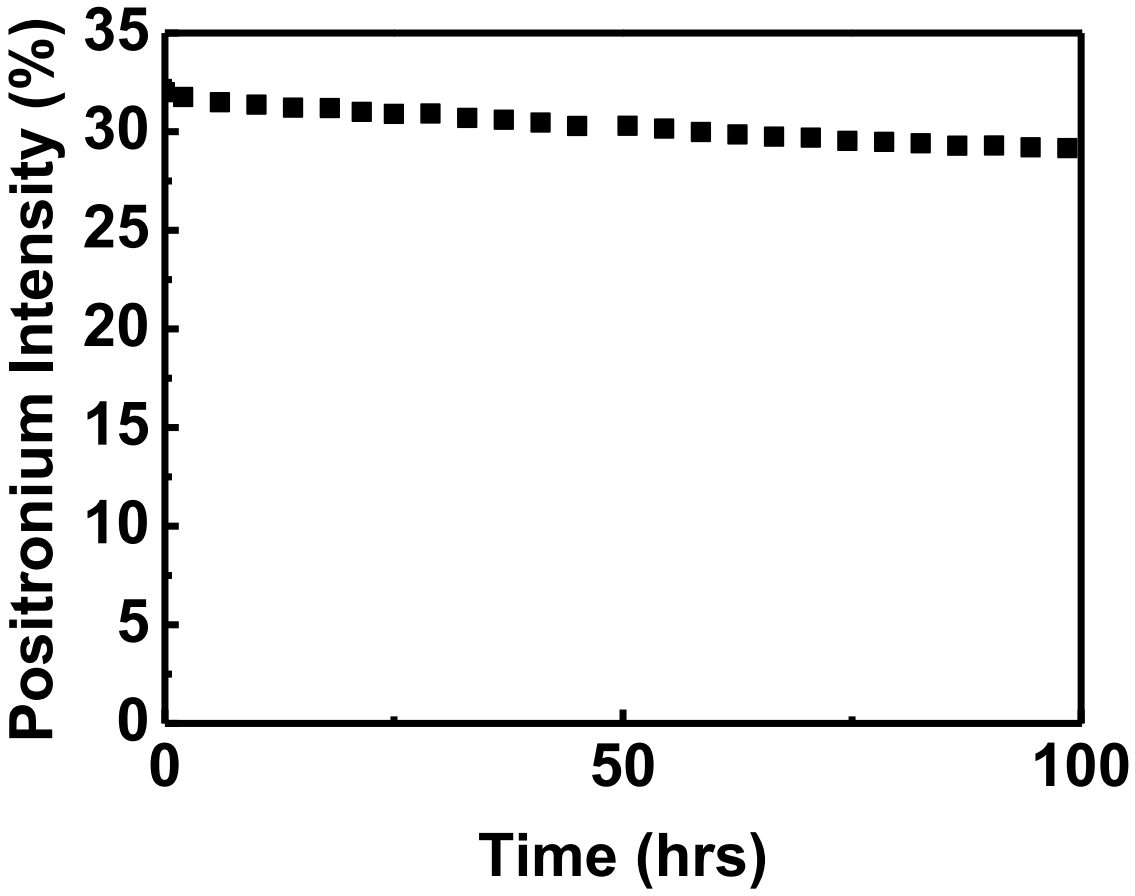

Figure 3.27 Ps framework intensity of $Zn_4O(FMA)_3$ against time (hrs) under the relative humidities of 16%.

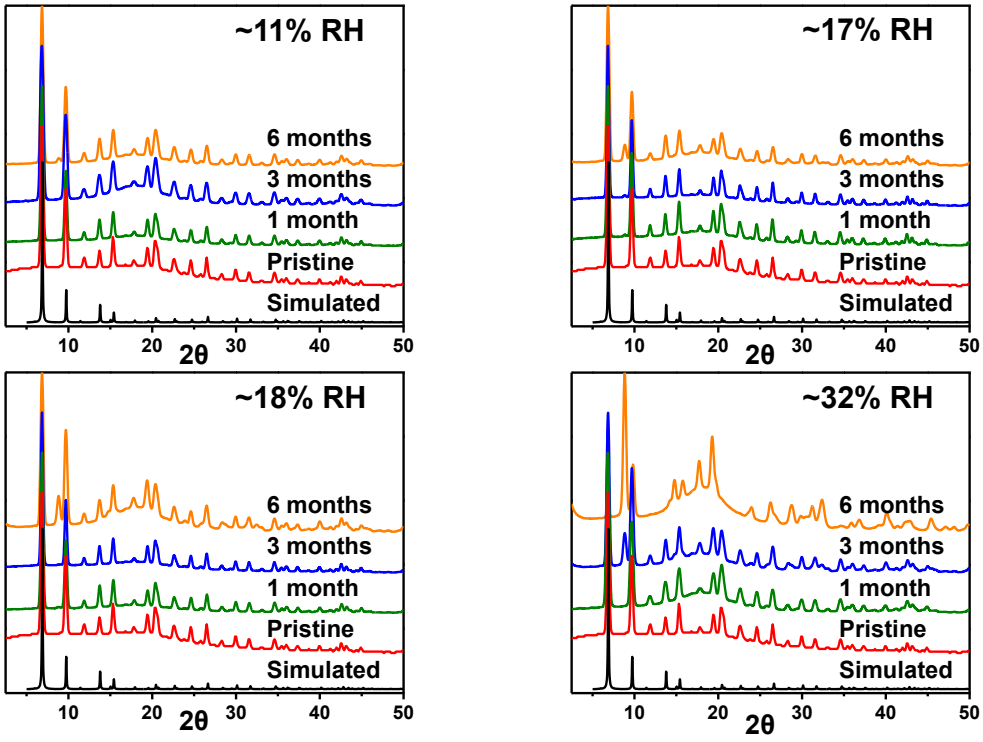

Figure 3.28 PXRD patterns for MOF-5 in the presence of varying relative humidity and time.

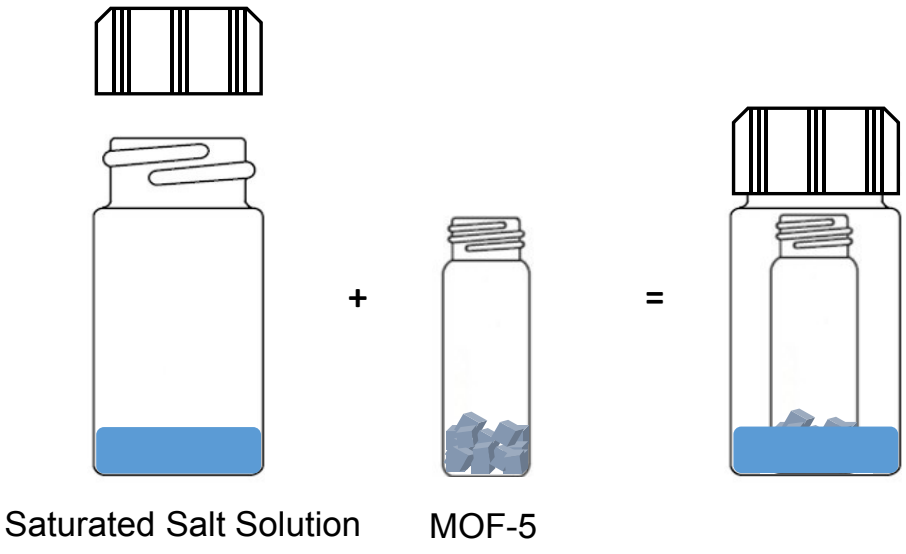

Figure 3.29 Long-term water stability of MOF-5 experiment setup.

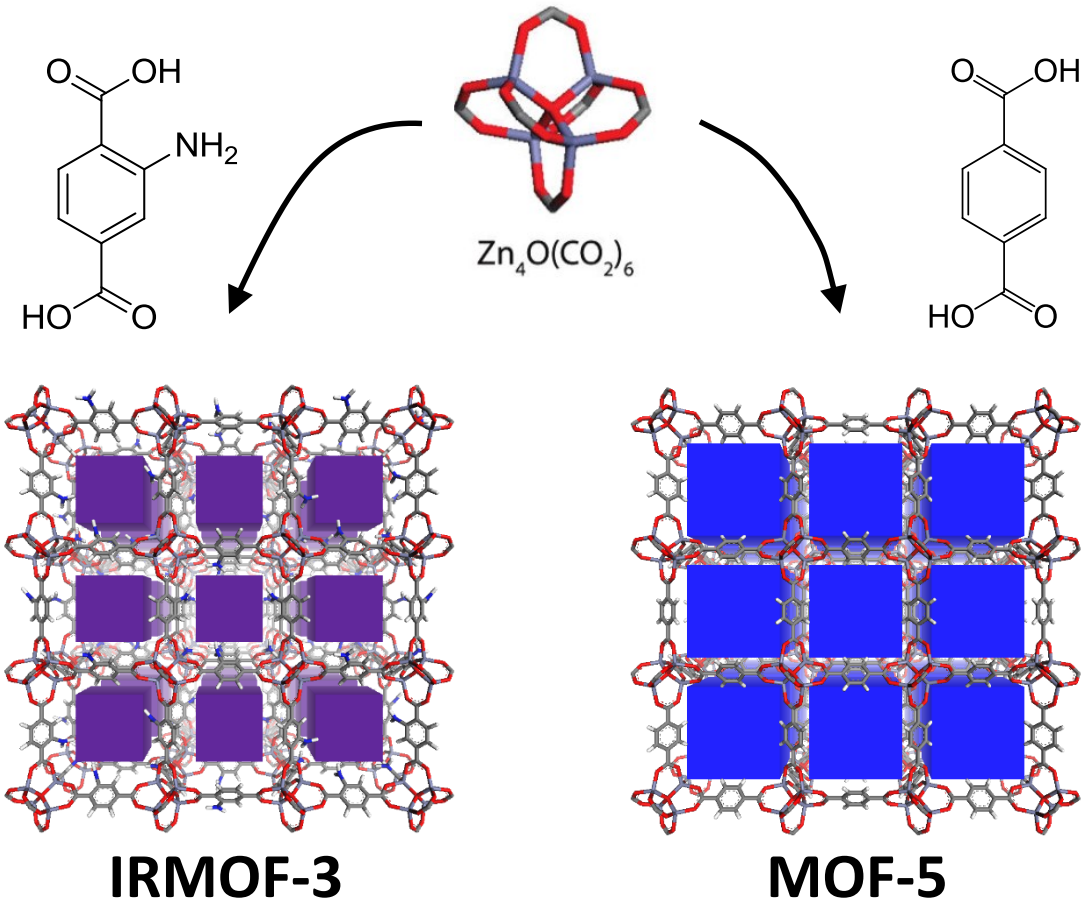

Figure 3.30 Compositions and structure comparison of IRMOF-3 (Zn_4O(aminoterephthalate)$_3$) and MOF-5 (Zn_4O(benzene-1,4-dicarboxylate)$_3$). Colored cubes show the accessible pore space.

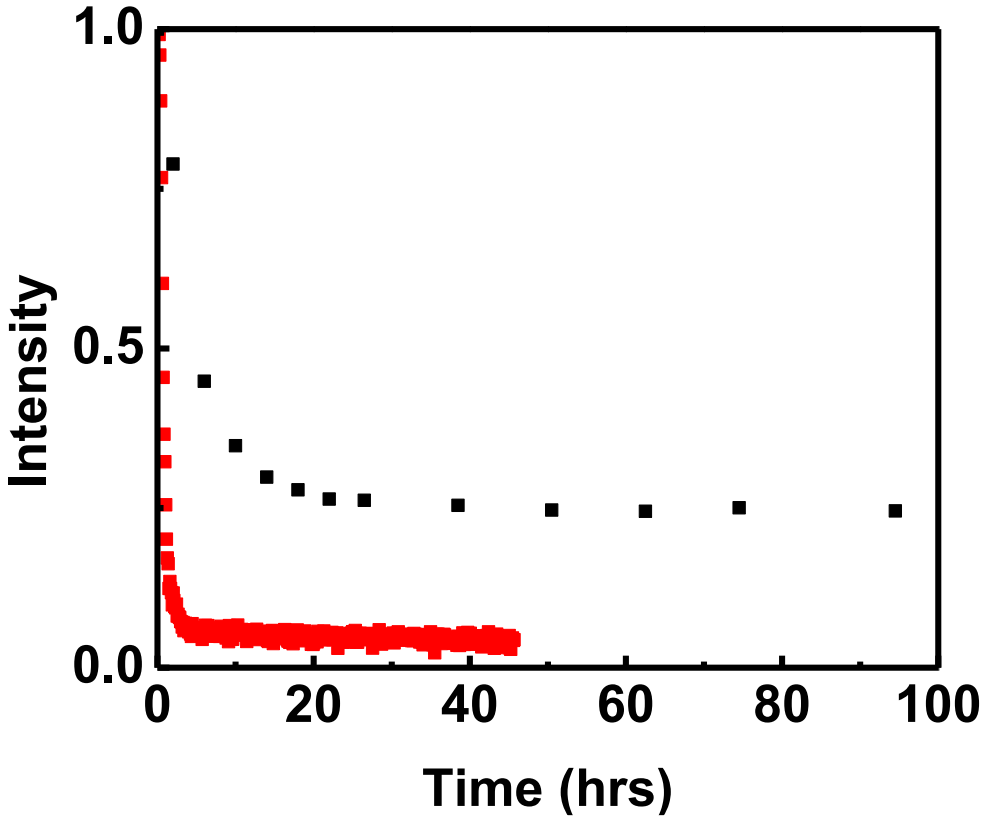

Figure 3.31 The intensity of PXRD primary peak (2θ=6.86°) of IRMOF-3 (red) and Ps framework intensity (black) as a function of time at 30% relative humidity.

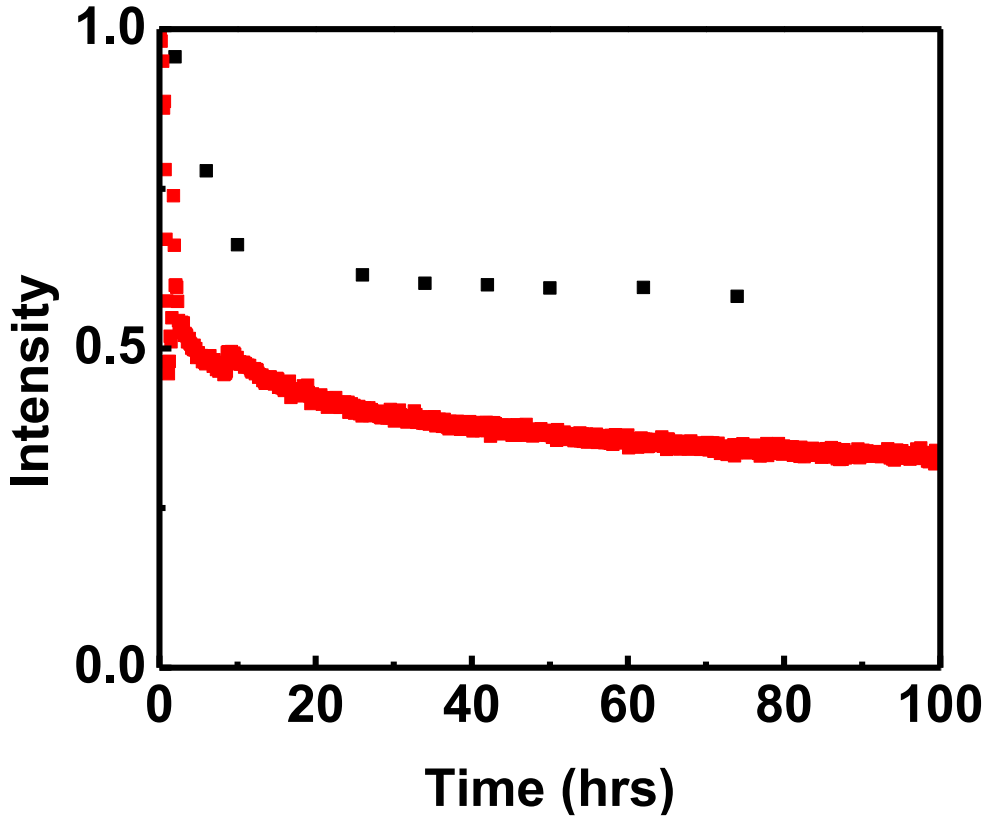

Figure 3.32 The intensity of PXRD primary peak (2θ=6.86°) of IRMOF-3 (red) and Ps framework intensity (black) as a function of time at 24% relative humidity.

3.6 References

(1) Rosi, N. L.; Eckert, J.; Eddaoudi, M.; Vodak, D. T.; Jaheon Kim; O'Keeffe, M.; Yaghi, O. M. Hydrogen Storage in Microporous Metal-Organic Frameworks. *Science* **2003**, *300*, 1127–1129.

(2) Murray, L. J.; Dincă, M.; Long, J. R. Hydrogen Storage in Metal–organic Frameworks. *Chem Soc Rev* **2009**, *38*, 1294–1314.

(3) Suh, M. P.; Park, H. J.; Prasad, T. K.; Lim, D.-W. Hydrogen Storage in Metal–Organic Frameworks. *Chem. Rev.* **2012**, *112*, 782–835.

(4) Liu, Y.; Kabbour, H.; Brown, C. M.; Neumann, D. A.; Ahn, C. C. Increasing the Density of Adsorbed Hydrogen with Coordinatively Unsaturated Metal Centers in Metal−Organic Frameworks. *Langmuir* **2008**, *24*, 4772–4777.

(5) Millward, A. R.; Yaghi, O. M. Metal−Organic Frameworks with Exceptionally High Capacity for Storage of Carbon Dioxide at Room Temperature. *J Am Chem Soc* **2005**, *127*, 17998–17999.

(6) Caskey, S.; Matzger, A. J.; Wong-Foy, A. G. Microporous Coordination Polymers as Novel Sorbents for Gas Separation. US20100258004 A1, October 14, 2010.

(7) Bloch, E. D.; Queen, W. L.; Krishna, R.; Zadrozny, J. M.; Brown, C. M.; Long, J. R. Hydrocarbon Separations in a Metal-Organic Framework with Open Iron(II) Coordination Sites. *Science* **2012**, *335*, 1606–1610.

(8) Dietzel, P. D. C.; Besikiotis, V.; Blom, R. Application of Metal–organic Frameworks with Coordinatively Unsaturated Metal Sites in Storage and Separation of Methane and Carbon Dioxide. *J Mater Chem* **2009**, *19*, 7362–7370.

(9) Lin, L.-C.; Kim, J.; Kong, X.; Scott, E.; McDonald, T. M.; Long, J. R.; Reimer, J. A.; Smit, B. Understanding CO_2 Dynamics in Metal–Organic Frameworks with Open Metal Sites. *Angew. Chem. Int. Ed.* **2013**, *52*, 4410–4413.

(10) Cychosz, K. A.; Wong-Foy, A. G.; Matzger, A. J. Enabling Cleaner Fuels: Desulfurization by Adsorption to Microporous Coordination Polymers. *J. Am. Chem. Soc.* **2009**, *131*, 14538–14543.

(11) Cychosz, K. A.; Ahmad, R.; Matzger, A. J. Liquid Phase Separations by Crystalline Microporous Coordination Polymers. *Chem. Sci.* **2010**, *1*, 293–302.

(12) Li, J.-R.; Kuppler, R. J.; Zhou, H.-C. Selective Gas Adsorption and Separation in Metal–organic Frameworks. *Chem Soc Rev* **2009**, *38*, 1477–1504.

(13) Lee, J.; Farha, O. K.; Roberts, J.; Scheidt, K. A.; Nguyen, S. T.; Hupp, J. T. Metal–organic Framework Materials as Catalysts. *Chem Soc Rev* **2009**, *38*, 1450–1459.

(14) Schoenecker, P. M.; Carson, C. G.; Jasuja, H.; Flemming, C. J. J.; Walton, K. S. Effect of Water Adsorption on Retention of Structure and Surface Area of Metal–Organic Frameworks. *Ind. Eng. Chem. Res.* **2012**, *51*, 6513–6519.

(15) Küsgens, P.; Rose, M.; Senkovska, I.; Fröde, H.; Henschel, A.; Siegle, S.; Kaskel, S. Characterization of Metal-Organic Frameworks by Water Adsorption. *Microporous Mesoporous Mater.* **2009**, *120*, 325–330.

(16) Cavka, J. H.; Jakobsen, S.; Olsbye, U.; Guillou, N.; Lamberti, C.; Bordiga, S.; Lillerud, K. P. A New Zirconium Inorganic Building Brick Forming Metal Organic Frameworks with Exceptional Stability. *J. Am. Chem. Soc.* **2008**, *130*, 13850–13851.

(17) Demessence, A.; D'Alessandro, D. M.; Foo, M. L.; Long, J. R. Strong CO_2 Binding in a Water-Stable, Triazolate-Bridged Metal−Organic Framework Functionalized with Ethylenediamine. *J. Am. Chem. Soc.* **2009**, *131*, 8784–8786.

(18) Cychosz, K. A.; Matzger, A. J. Water Stability of Microporous Coordination Polymers and the Adsorption of Pharmaceuticals from Water. *Langmuir* **2010**, *26*, 17198–17202.

(19) Low, J. J.; Benin, A. I.; Jakubczak, P.; Abrahamian, J. F.; Faheem, S. A.; Willis, R. R. Virtual High Throughput Screening Confirmed Experimentally: Porous Coordination Polymer Hydration. *J. Am. Chem. Soc.* **2009**, *131*, 15834–15842.

(20) Klinowski, J.; Paz, F. A. A.; Silva, P.; Rocha, J. Microwave-Assisted Synthesis of Metal–Organic Frameworks. *Dalton Trans.* **2010**, *40*, 321–330.

(21) Yang, J.; Grzech, A.; Mulder, F. M.; Dingemans, T. J. Methyl Modified MOF-5: A Water Stable Hydrogen Storage Material. *Chem. Commun.* **2011**, *47*, 5244–5246.

(22) Feldblyum, J. I.; Liu, M.; Gidley, D. W.; Matzger, A. J. Reconciling the Discrepancies between Crystallographic Porosity and Guest Access As Exemplified by Zn-HKUST-1. *J. Am. Chem. Soc.* **2011**, *133*, 18257–18263.

(23) Xue, M.; Liu, Y.; Schaffino, R. M.; Xiang, S.; Zhao, X.; Zhu, G.-S.; Qiu, S.-L.; Chen, B. New Prototype Isoreticular Metal−Organic Framework $Zn_4O(FMA)_3$ for Gas Storage. *Inorg Chem* **2009**, *48*, 4649–4651.

(24) Li, H.; Eddaoudi, M.; O'Keeffe, M.; Yaghi, O. M. Design and Synthesis of an Exceptionally Stable and Highly Porous Metal-Organic Framework. *Nature* **1999**, *402*, 276–279.

(25) Koh, K.; Van Oosterhout, J. D.; Roy, S.; Wong-Foy, A. G.; Matzger, A. J. Exceptional Surface Area from Coordination Copolymers Derived from Two Linear Linkers of Differing Lengths. *Chem. Sci.* **2012**, *3*, 2429.

(26) Rowsell, J. L. C.; Yaghi, O. M. Effects of Functionalization, Catenation, and Variation of the Metal Oxide and Organic Linking Units on the Low-Pressure Hydrogen Adsorption Properties of Metal−Organic Frameworks. *J Am Chem Soc* **2006**, *128*, 1304–1315.

(27) Gidley, D. W.; Peng, H.-G.; Vallery, R. S. Positron Annihilation as a Method to Characterize Porous Materials. *Annu. Rev. Mater. Res.* **2006**, *36*, 49–79.

(28) Liu, M.; Wong-Foy, A. G.; Vallery, R. S.; Frieze, W. E.; Schnobrich, J. K.; Gidley, D. W.; Matzger, A. J. Evolution of Nanoscale Pore Structure in Coordination Polymers During Thermal and Chemical Exposure Revealed by Positron Annihilation. *Adv. Mater.* **2010**, *22*, 1598–1601.

(29) Feldblyum, J. I.; Dutta, D.; Wong-Foy, A. G.; Dailly, A.; Imirzian, J.; Gidley, D. W.; Matzger, A. J. Interpenetration, Porosity, and High-Pressure Gas Adsorption in Zn_4O(2,6-Naphthalene dicarboxylate)$_3$. *Langmuir* **2013**, *29*, 8146–8153.

(30) Eldrup, M.; Lightbody, D.; Sherwood, J. N. The Temperature Dependence of Positron Lifetimes in Solid Pivalic Acid. *Chem. Phys.* **1981**, *63*, 51–58.

(31) Tao, S. J. Positronium Annihilation in Molecular Substances. *J. Chem. Phys.* **1972**, *56*, 5499–5510.

(32) Hausdorf, S.; Wagler, J.; Mossig, R.; Mertens, F. O. R. L. Proton and Water Activity-Controlled Structure Formation in Zinc Carboxylate-Based Metal Organic Frameworks. *J Phys Chem A* **2008**, *112*, 7567–7576.

(33) Farha, O. K.; Hupp, J. T. Rational Design, Synthesis, Purification, and Activation of Metal−Organic Framework Materials. *Acc. Chem. Res.* **2010**, *43*, 1166–1175.

(34) Jasuja, H.; Huang, Y.; Walton, K. S. Adjusting the Stability of Metal-Organic Frameworks under Humid Conditions by Ligand Functionalization. *Langmuir* **2012**.

(35) Nguyen, J. G.; Cohen, S. M. Moisture-Resistant and Superhydrophobic Metal−Organic Frameworks Obtained via Postsynthetic Modification. *J. Am. Chem. Soc.* **2010**, *132*, 4560–4561.

(36) Nguyen, J. G.; Cohen, S. M. Moisture-Resistant and Superhydrophobic Metal−Organic Frameworks Obtained via Postsynthetic Modification. *J Am Chem Soc* **2010**, *132*, 4560–4561.

(37) Rowsell, J. L. C.; Yaghi, O. M. Effects of Functionalization, Catenation, and Variation of the Metal Oxide and Organic Linking Units on the Low-Pressure Hydrogen Adsorption Properties of Metal−Organic Frameworks. *J. Am. Chem. Soc.* **2006**, *128*, 1304–1315.

(38) Brunauer, S.; Emmett, P. H.; Teller, E. Adsorption of Gases in Multimolecular Layers. *J. Am. Chem. Soc.* **1938**, *60*, 309–319.

(39) Walton, K. S.; Snurr, R. Q. Applicability of the BET Method for Determining Surface Areas of Microporous Metal−Organic Frameworks. *J. Am. Chem. Soc.* **2007**, *129*, 8552–8556.

(40) Walton, K. S.; Snurr, R. Q. Applicability of the BET Method for Determining Surface Areas of Microporous Metal−Organic Frameworks. *J. Am. Chem. Soc.* **2007**, *129*, 8552–8556.

(41) Düren, T.; Millange, F.; Férey, G.; Walton, K. S.; Snurr, R. Q. Calculating Geometric Surface Areas as a Characterization Tool for Metal−Organic Frameworks. *J. Phys. Chem. C* **2007**, *111*, 15350–15356.

Chapter 4 **Conclusions and Future Directions**

4.1 **Summary**

In this thesis, the efficacy of air dehumidification by MCPs and the water sensitivity in Zn_4O-based MOFs were scrutinized with the aim of a deep understanding of the interaction between water and microporous coordination polymers. Using packed bed breakthrough method, a cross-section of currently available MCPs were investigated in Chapter 2 for their total water capacities and breakthrough water capacities as candidates for air dehumidification. It was discovered that MCPs possessing coordinatively unsaturated metal sites, HKUST-1 and Co/DOBDC in particular, demonstrated excellent water total capacities and breakthrough capacities, exceeding those of commercial activated alumina. Some well-studied MCPs with exceeding good water stability, such as UiO-66, MIL-100 and MIL-101, however, are found to be unsuitable for gas drying applications due to their poor breakthrough capacities. Employing hydrophilic functionality on the linkers of the aforementioned water-stable MCPs has been proven to be able to optimize their breakthrough capacities while retaining comparable total water capacities. Full cyclic thermal regeneration of MCPs with dry air was achieved using significantly less energy compared to alumina, suggesting that there are great opportunities for MCPs in the field of energy-efficient gas dehumidification.

Chapter 3 highlighted the need to understand the details of structural collapse of Zn_4O-based MOFs caused by moisture with regard to pore size evolution, consequently, there remains a strong driving force to utilize a complementary technique that can overcome the limitations of conventional characterization techniques, PXRD and sorption analysis, which cannot characterize disorder and monitor pore structural changes during adsorption in real-time. PALS, as an *in situ* nondestructive probe for pore sizes, was utilized to characterize changes in pore size during water degradation for a series of

Zn_4O-based MOFs. MOF-5 is one of the most well-studied Zn_4O-based MOFs and is reported to have be extremely sensitive to water with the detailed mechanism remaining unclear. PALS incorporated in tandem with a flow-through system was applied to MOF-5 to acquire porosity evolution information under controlled relative humidity. In stark contrast to the commonly believed extreme sensitivity to water, an induction period for water degradation of MOF-5 was observed by PALS from the decrease in porosity signaling a much greater stability. MOF-5 is able to maintain its framework porosity, crystallinity and surface area after 200 hours exposure to 30% relative humidity. Under the relative humidities of 34%, 36%, 38% and 40%, the population of intact pores in MOF-5 was found to follow a universal sigmoidal trend, however, the "half degradation time ($T_{1/2}$)" of MOF-5 defined as the number of hours required for the framework intensity to decrease to half of its original value was nominally exponential dependent on relative humidity. A dramatic difference in the water stability of MOF-5 was found in a very small window of relative humidity. UMCM-8, composed of $Zn_4O(CO_2R)_6$ metal clusters and a 1:1 ratio of the linear linkers benzene-1,4-dicarboxylate (BDC) and naphthalene-2,6-dicarboxylate (NDC), has a structure similar to MOF-5 with two cubic cages and two tetragonal cages which are larger than MOF-5. Against the general observation that MOFs, within a homologous series, exhibits less stability due to a tendency towards structural collapse, UMCM-8 was detected by PALS to maintain intact at a higher relative humidity than MOF-5. This suggested that pore size and linker hydrophilicity are decisive factors for MOFs water stability and the degradation must be triggered by a certain amount of accumulation of water in the pore, a mechanism similar to capillary condensation. A higher relative humidity is needed for sufficient accumulation of water molecules to hydrolyze coordination bonds to break down the structure when the pores of MOF has a larger inner diameter. IRMOF-3 was found to be more sensitive to humidity than MOF-5 resulting from the amine groups according to continuous monitoring of porosity by PALS. Residual porosity and crystallinity after humidity treatment were observed. One explanation for the residual porosity is that IRMOF-3 degrades into an amorphous continuous layer which protests the interior crystalline material from further contact with water. The water stability of Zn_4O-based

MOFs was also demonstrated to be history-dependent as evidenced by the fact that the defects in MOF-5 generated by water lead to a faster degradation.

4.2 **Further Work: Development of MCPs for dehumidification**

In Chapter 2, some archetypical MCPs have displayed superior gas dehumidification performance. Challenges for MCPs to serve as industrially viable sorbents lie in their robustness under extended cycling regeneration and the cost of the MCP sorbents. The sorbent robustness under process conditions has been actively studied by scientists and engineers mainly via the discovery of new MCPs with improved stability. High-throughput[1,2] methods are ideal to speed up the discovery of MCPs. The issue of MCP sorbent cost is actively being pursued in industry and academia by developing scale-up synthesis procedure.[3]

High-throughput methods applied to MCPs discovery allowing systematic investigation of compositional and process parameters with the consumption of a very small amount of starting materials have attracted much attention recently.[1,4,5,6] MCPs with high water stability, large pore volume and potential water capacity have been successfully achieved via a high-throughput methodology.[2,5,7] 9600 reactions were performed by Banerjee, Yaghi and co-workers and allowed establishing the optimal synthesis conditions for ZIFs using a high-throughput protocol.[6] MIL-101,[8] $Cr_3XO[C_6H_4(COO)_2]_3$ (X=F, OH) has been scrutinized as potential sorbents for different applications due to its high surface area, possession of both microporosity and mesoporosity and high stability against water. The high water stability of MIL-101 is attributed to its trinuclear chromium metal clusters[9], An isoreticular mesoporous MCP replacing 1,4-benzenedicarboxylate by 2,6-naphthalenedicarboxylate in the MIL-101 has been achieved with optimized synthesis conditions after more than 600 individual reactions performed employing a 24-well high-throughput reactor system.[10] We have demonstrated that MCPs, such as HKUST-1 possessing paddle-wheel coordinatively unsaturated metal sites, have excellent water total capacities and breakthrough capacities in Chapter 2. Using high-throughput methods, four Ni-based paddle-wheel containing porous MCPs were synthesized with a comprehensive screening of compositional and

process parameters.[11] These Ni-based MCPs can potentially be good candidates for air drying due to their high water affinity and acceptable stability. We anticipate that the powerful high-throughput method will provide access to a broad range of materials with high robustness for applications in a number of fields.

The challenges for the utilization of MCPs for industrial applications, such as dehumidification, lie in their production as well as their properties. Availability and cost of the starting materials, synthesis conditions, activation process, yields and environmental toxicity are factors to be considered when MCPs are evaluated for certain industrial applications.[2] Solvothermal synthesis[12], as the most commonly used method, have made a large collection of MCPs in lab-scale, however, is not cost effective for industry-scale synthesis due to the extensive solvent exchange activation process. Hence, intensive investigation should be launched for scaleup MCP synthesis. A scaleup synthesis route was first developed for HKUST-1 by Bülow and co-workers in 2002.[13] Fe-MIL-100 has been successfully synthesized on large scale via a fluorine-free route satisfying both the industrial requirements for yield and environmental toxicity.[14] Recently some well-studied MCPs, such as MOF-5,[15] Zn/DOBDC, MOF-177, HKUST-1[16] and ZIF-8[17], synthesized from non-solvothermal synthetic routes and the commercially available MCPs demonstrate the promising future for scaleup synthesis of MCPs for industrial dehumidification.

4.3 **Future Work: Polymer Coating on MCPs**

Porous solids offer unique opportunities for a wide variety of potential applications. Zeolites[18,19] and activated carbon[20] currently dominate small molecule adsorption and separation applications; combining these types of materials with polymers to form hybrids[21,22] can lead to enhanced properties and an increase of structural tunability.[23,24] Interfacing polymers with zeolites or activated carbon is difficult because of the lack of tethered initiators on these porous materials for polymer grafting. However, MCPs have the ability to carry tethered initiators due to the tunability of the linker.[25] Recently, hybrid materials combining MCPs and other types of materials have emerged to expand their field of applications, given the incredible diversity of transition metals

and organic linkers used to synthesize MCPs[26,27,28,29], a variety of pre- and post- synthetic modification possibility on MCPs and a wide selection of other materials, such as polymers,[30] metal nanoparticles,[29,31] carbon nanotubes,[32] graphite oxide,[27] semiconductor quantum dots[33] and peptide[28].

Preliminary results for the novel synthesis methodology for polymer@MCP in which the polymer chains are tethered to the outer shell of MCP using polystyrene@MOF-5 (hereafter referred to as PS@MOF-5) as an example is presented. The introduction of polymer coating is demonstrated to be a promising approach to increase the water stability of MCPs. Synthetic parameters for polymer@MCP were chosen to obtain uniform polymer coating on the surface of the MCP while maintaining its internal porosity. "Grafting from" polymerization is used since it involves polymer growth from an already formed MCP structure to preserve its crystallinity to the maximum extent, also allows for control over the position of polymer propagation and the thickness of the polymer coating.

MOF-5,[34] $Zn_4O[C_6H_4(COO)_2]_3$, was chosen because it has been extensively scrutinized and reported to have consistently high surface area, simple cubic geometry, and a broad use as a benchmark material in the past by our group.[35,36,37] However, 1,4-benzene dicarboxylate, the linker in MOF-5, has no functional group available to facilitate polymerization. IRMOF-3[38] is a derivative of MOF-5 with 2-amino-1,4-benzenedicarboxylate which compromises its porosity and surface area due to the volume addition from the functional groups but maintains same lattice constant as MOF-5. The amine in IRMOF-3 does not participate in the coordination bond supporting the framework, and thereby can readily undergo post-synthetic modification.[39] Core-shell arrangement of linkers[40] has been applied to achieve IRMOF-3@MOF-5 in order to preserve high porosity and provide a shell of handles for polymer initiator functionalization with controlled thickness. Monomers will propagate only from the initiator carrying linkers and therefore the resulting polymers are confined to the surface of the crystals. In this way, the depth of polymer layer can be controlled by the thickness of IRMOF-3 shell in addition to other parameters for polymer growth.

Powder X-ray diffraction (PXRD) and N_2 adsorption analysis were performed after each step of synthesis to investigate the preservation of crystallinity and porosity of

the MCP. Figure 4.2 shows that the PXRD patterns of MOF-5, IRMOF-3@MOF-5, and PS@MOF-5 are identical, indicating the MOF-5 framework maintains its crystallinity upon core-shell formation, post synthetic modification, and polymer coating. This well-retained original crystallinity is critical for practical applications. In addition, thermogravimetric analysis (TGA) of PS@MOF-5 under N_2 after thorough washing and solvent removal shows the de-polymerization of polystyrene by a single decomposition process at ~415 °C and subsequent degradation of MOF-5 at ~515 °C (Figure 4.4) validating the existence of polystyrene coating on MOF-5.Well-retained internal surface area of hybrid MCPs is one of the foremost highly desirable characteristics in many potential applications. Here we applied the Brunauer-Emmett-Teller (BET) approximation to the N_2 adsorption isotherms of MOF-5, IRMOF-3@MOF-5 and PS@MOF-5 to study the effect of core-shell formation, post synthetic modification, and polymer coating on their gas-accessible surface area. IRMOF-3@MOF-5 has a BET surface areas of 3358 m^2/g, which is a good indication of intact MOF-5 core and porosity preservation. PS@MOF-5 has a BET surface area of 2184 m^2/g which loses ~35% from the initial activated MOF-5 (BET surface area=3425 m^2/g). This can be explained by the additional mass from polystyrene which does not contribute to the surface area and makes up ~30 wt% of PS@MOF-5 according to TGA (Figure 4.4).

The depth of polymerization was verified by Raman spectroscopy. A cross section of PS@MOF-5 was mapped by Raman spectroscopy (Figure 4.5) showing that polystyrene only appears on the surface of the crystal and its depth (8-10 μm) is consistent with the thickness of IRMOF-3 shell (Figure 4.6) by Raman mapping of fluorescence signal from IRMOF-3 at the wavenumber of 1494 cm^{-1}.

A major barrier to applications for a class of well-studied MCPs is their instability against moisture.[41] Although MOF-5 has been intensively investigated in Chapter 2 and Chapter 3 to have long-term stability against water vapor over a fairly large and operationally relevant relative humidity window, there is still a large room for improvement in terms of its water stability. In order to test if the polystyrene coating shields interior crystallinity of PS@MOF-5 from water damage, experiments were conducted to assess the kinetic stability of PS@MOF-5 against water vapor. Figure 4.7 demonstrates that PS@MOF-5 maintained its crystallinity after two weeks of exposure to

humid air with relative humidity of 33% while MOF-5 has transformed into ZnBDC·xH_2O[42] completely. These results mean that the polystyrene coating on MOF-5 is able to effectively protect internal MOF-5 structure from water attack.

Although PS@MOF-5, a hybrid polymer@MCP composite is successfully synthesized and some characterization and moisture stability of the material is presented; details of polymerization mechanism are still unclear. Future work will focus on elucidating the unique case of polymerization in framework with control experiments. Additional characterization such as scanning electron microscopy (SEM), N_2 sorption analysis, and contact angle measurement of the pristine and polymer coated MCPs before and after moisture treatment will assist to understand the stability kinetic of these hybrid materials. Applications such as small molecule separation, heterogeneous catalysis with polymer@MCP will be studied with a hope to shed light on the effects of polymer coating on the selectivity for gases. A wide selection of monomer and MCP combination will also be explored for new opportunities with hybrid polymer@MCP composites.

4.4 **Figures**

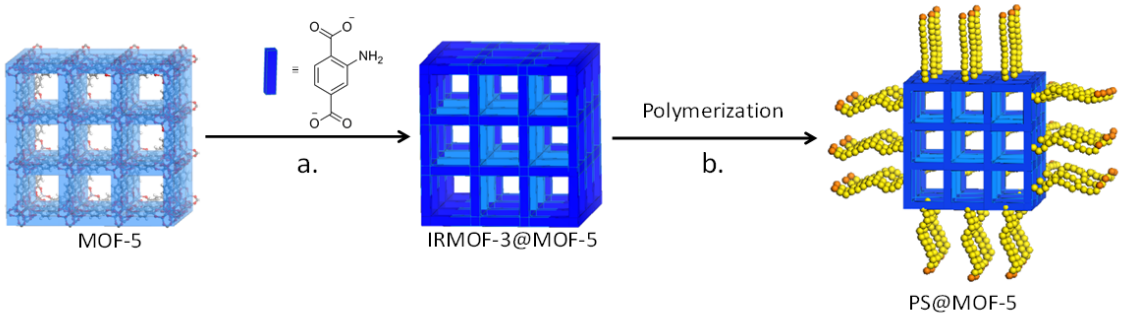

Figure 4.1 Synthetic route to the PS@MOF-5 material: (a) Core-shell formation on MOF-5 by crystallization with IRMOF-3 linker (IRMOF-3@MOF-5), (b) Polymerization to achieve MOF-5 with polystyrene coating (PS@MOF-5).

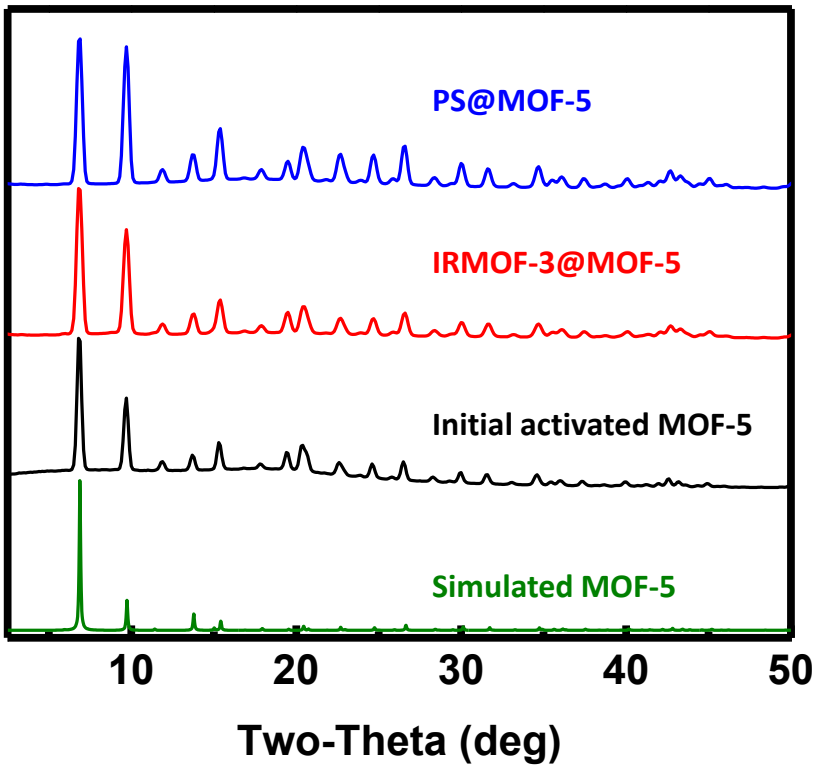

Figure 4.2 Overlay of PXRD patterns of simulated (SAHYIK.cif), initial activated MOF-5, IRMOF-3@MOF-5 and polystyrene@MOF-5 (PS@MOF-5).

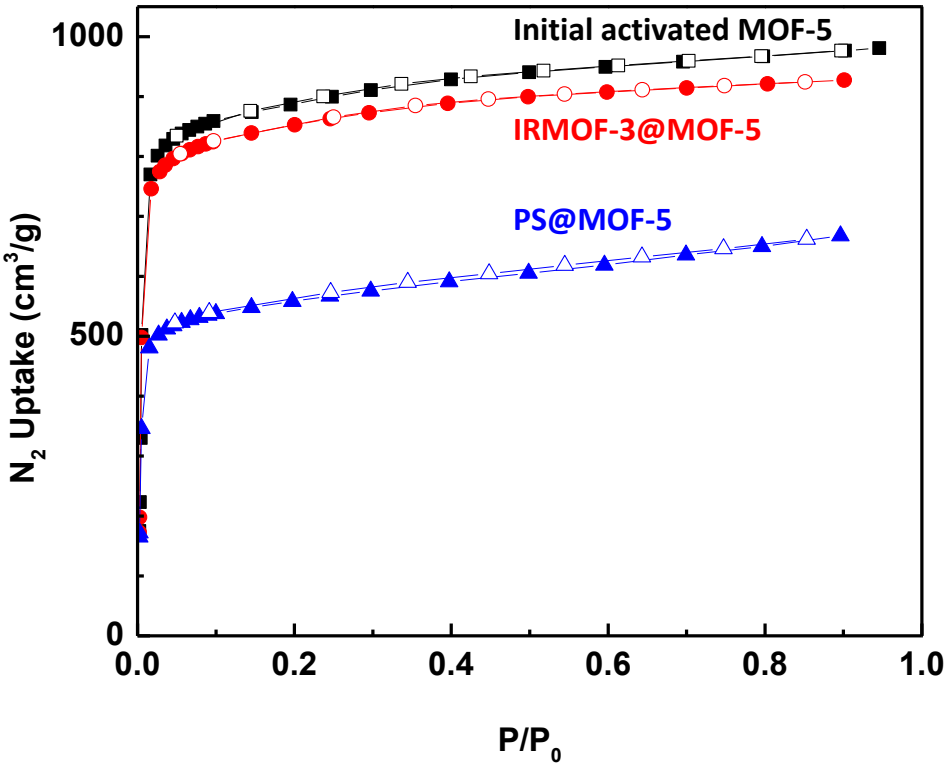

Figure 4.3 Overlay of N_2 sorption isotherms of initial activated MOF-5 (black, BET SA=3425 m^2/g), IRMOF-3@MOF-5 (red, BET SA=3358 m^2/g) and polystyrene@MOF-5 (PS@MOF-5, orange, BET SA=2184 m^2/g).

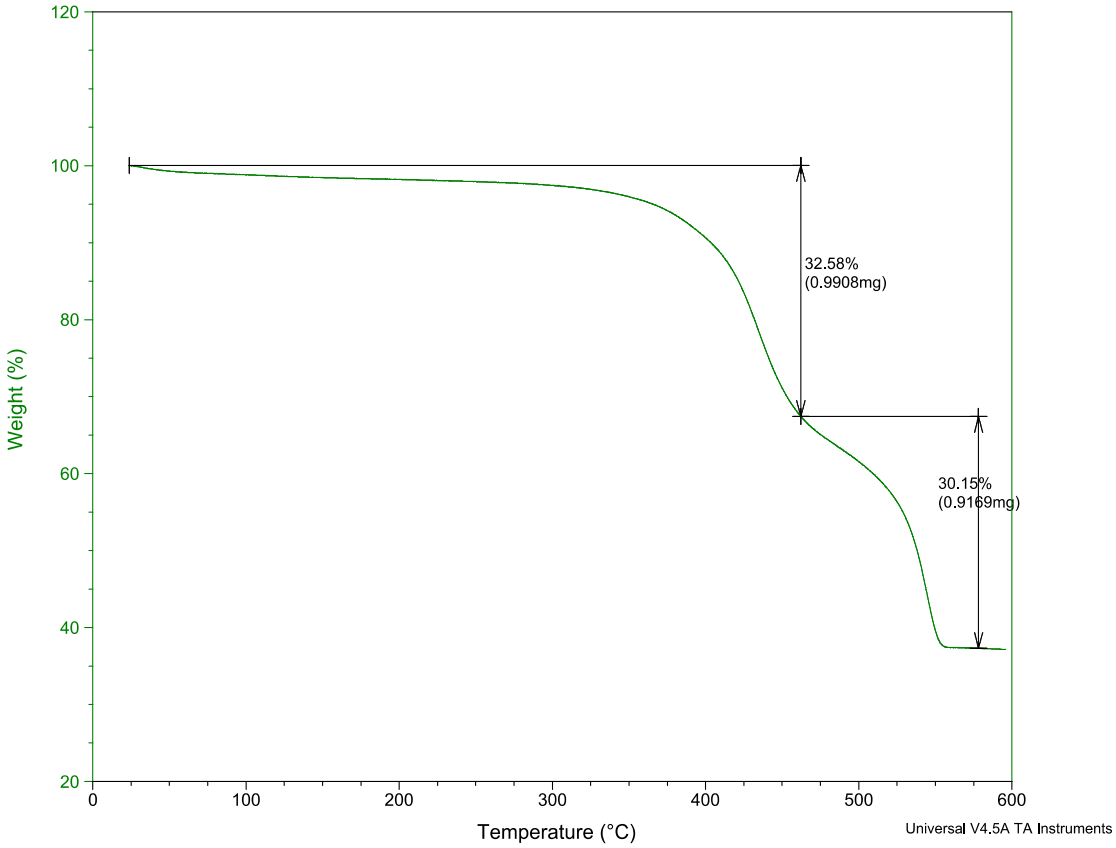

Figure 4.4 Thermogravimetric analysis of PS@MOF-5 under a N_2 atmosphere after solvent removal.

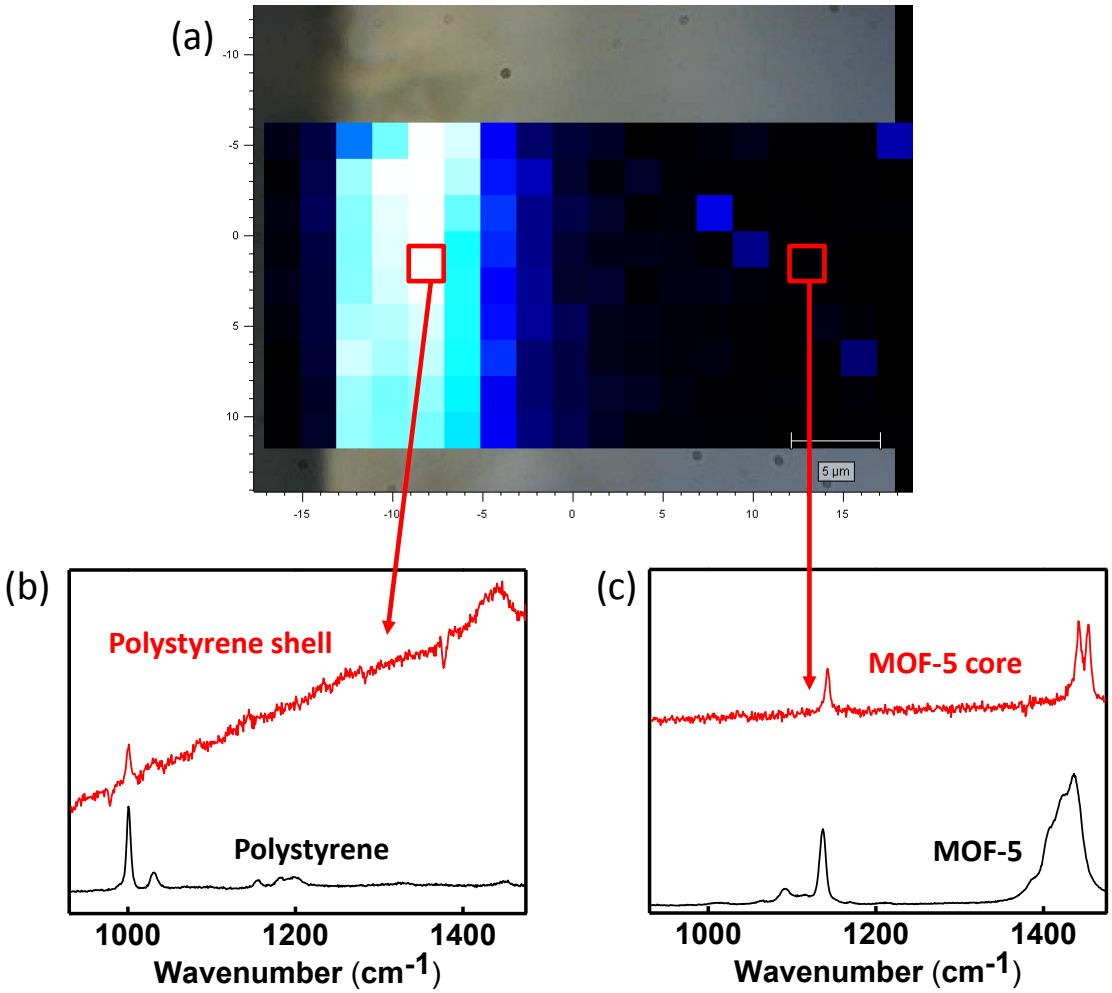

Figure 4.5 (a) Raman mapping of PS@MOF-5 showing the intensity of the peak at the wavenumber of 1001 cm^{-1} representing polystyrene. (b) Raman spectra of polystyrene shell of PS@MOF-5 and polystyrene bead. (c) Raman spectra of MOF-5 core of PS@MOF-5 and MOF-5.

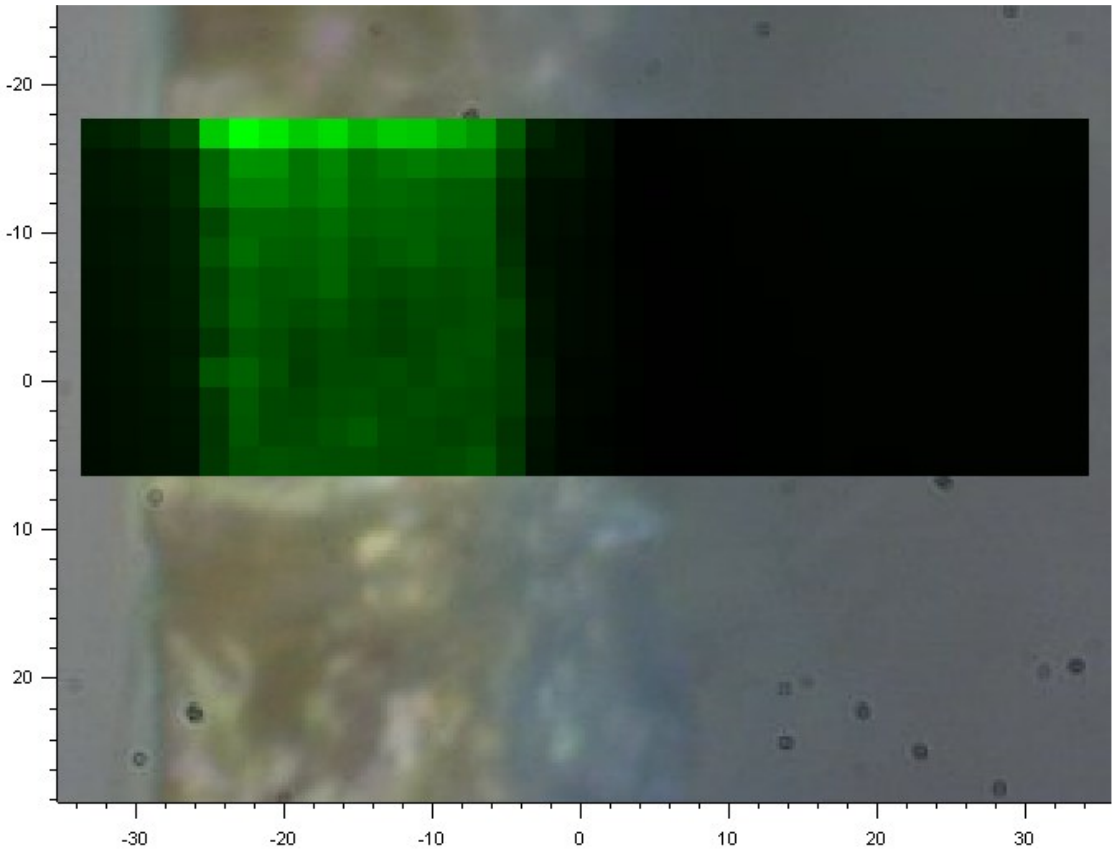

Figure 4.6 Raman mapping of IRMOF-3@MOF-5 showing the intensity of the peak at the wavenumber of 1494 cm^{-1} representing IRMOF-3.

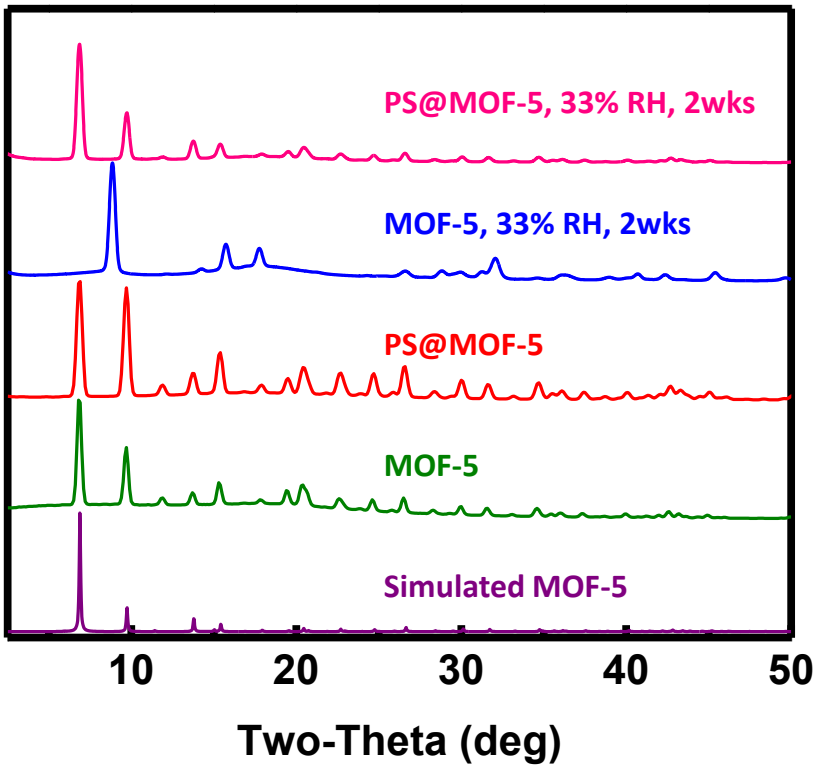

Figure 4.7 PXRD patterns for simulated MOF-5, initial activated MOF-5, PS@MOF-5, MOF-5 and PS@MOF-5 in the presence of 33% relative humidity (RH) for 2 weeks.

4.5 References

(1) Stock, N. High-Throughput Investigations Employing Solvothermal Syntheses. *Microporous Mesoporous Mater.* **2010**, *129*, 287–295.

(2) Stock, N.; Biswas, S. Synthesis of Metal-Organic Frameworks (MOFs): Routes to Various MOF Topologies, Morphologies, and Composites. *Chem. Rev.* **2012**, *112*, 933–969.

(3) Schoenecker, P. M.; Belancik, G. A.; Grabicka, B. E.; Walton, K. S. Kinetics Study and Crystallization Process Design for Scale-up of UiO-66-NH_2 Synthesis. *AIChE J.* **2013**, *59*, 1255–1262.

(4) Stock, N.; Bein, T. High-Throughput Investigation of Metal Carboxyarylphosphonate Hybrid Compounds. *J. Mater. Chem.* **2005**, *15*, 1384.

(5) Stock, N.; Bein, T. High-Throughput Synthesis of Phosphonate-Based Inorganic-Organic Hybrid Compounds under Hydrothermal Conditions. *Angew. Chem. Int. Ed.* **2004**, *43*, 749–752.

(6) Banerjee, R.; Phan, A.; Wang, B.; Knobler, C.; Furukawa, H.; O'Keeffe, M.; Yaghi, O. M. High-Throughput Synthesis of Zeolitic Imidazolate Frameworks and Application to CO_2 Capture. *Science* **2008**, *319*, 939–943.

(7) Moliner, M.; Serra, J. M.; Corma, A.; Argente, E.; Valero, S.; Botti, V. Application of Artificial Neural Networks to High-Throughput Synthesis of Zeolites. *Microporous Mesoporous Mater.* **2005**, *78*, 73–81.

(8) Ferey, G.; Mellot-Draznieks, C.; Serre, C.; Millange, F.; Dutour, J.; Surblé, S.; Margiolaki, I. A Chromium Terephthalate-Based Solid with Unusually Large Pore Volumes and Surface Area. *Science* **2005**, *309*, 2040–2042.

(9) Cychosz, K. A.; Matzger, A. J. Water Stability of Microporous Coordination Polymers and the Adsorption of Pharmaceuticals from Water. *Langmuir* **2010**, *26*, 17198–17202.

(10) Sonnauer, A.; Hoffmann, F.; Fröba, M.; Kienle, L.; Duppel, V.; Thommes, M.; Serre, C.; Férey, G.; Stock, N. Giant Pores in a Chromium 2,6-Naphthalenedicarboxylate Open-Framework Structure with MIL-101 Topology. *Angew. Chem. Int. Ed.* **2009**, *48*, 3791–3794.

(11) Maniam, P.; Stock, N. Investigation of Porous Ni-Based Metal–Organic Frameworks Containing Paddle-Wheel Type Inorganic Building Units via High-Throughput Methods. *Inorg. Chem.* **2011**, *50*, 5085–5097.

(12) Rabenau, A. The Role of Hydrothermal Synthesis in Preparative Chemistry. *Angew. Chem. Int. Ed. Engl.* **1985**, *24*, 1026–1040.

(13) Min Wang, Q.; Shen, D.; Bülow, M.; Ling Lau, M.; Deng, S.; Fitch, F. R.; Lemcoff, N. O.; Semanscin, J. Metallo-Organic Molecular Sieve for Gas Separation and Purification. *Microporous Mesoporous Mater.* **2002**, *55*, 217–230.

(14) Seo, Y.-K.; Yoon, J. W.; Lee, J. S.; Lee, U.-H.; Hwang, Y. K.; Jun, C.-H.; Horcajada, P.; Serre, C.; Chang, J.-S. Large Scale Fluorine-Free Synthesis of

Hierarchically Porous Iron(III) Trimesate MIL-100(Fe) with a Zeolite MTN Topology. *Microporous Mesoporous Mater.* **2012**, *157*, 137–145.

(15) Huang, L.; Wang, H.; Chen, J.; Wang, Z.; Sun, J.; Zhao, D.; Yan, Y. Synthesis, Morphology Control, and Properties of Porous Metal–organic Coordination Polymers. *Microporous Mesoporous Mater.* **2003**, *58*, 105–114.

(16) Tranchemontagne, D. J.; Hunt, J. R.; Yaghi, O. M. Room Temperature Synthesis of Metal-Organic Frameworks: MOF-5, MOF-74, MOF-177, MOF-199, and IRMOF-0. *Tetrahedron* **2008**, *64*, 8553–8557.

(17) Cravillon, J.; Münzer, S.; Lohmeier, S.-J.; Feldhoff, A.; Huber, K.; Wiebcke, M. Rapid Room-Temperature Synthesis and Characterization of Nanocrystals of a Prototypical Zeolitic Imidazolate Framework. *Chem. Mater.* **2009**, *21*, 1410–1412.

(18) Lai, Z.; Bonilla, G.; Diaz, I.; Nery, J. G.; Sujaoti, K.; Amat, M. A.; Kokkoli, E.; Terasaki, O.; Thompson, R. W.; Tsapatsis, M.; et al. Microstructural Optimization of a Zeolite Membrane for Organic Vapor Separation. *Science* **2003**, *300*, 456–460.

(19) Smit, B.; Maesen, T. L. M. Molecular Simulations of Zeolites: Adsorption, Diffusion, and Shape Selectivity. *Chem. Rev.* **2008**, *108*, 4125–4184.

(20) Suzuki, M. Activated Carbon Fiber: Fundamentals and Applications. *Carbon* **1994**, *32*, 577–586.

(21) Kickelbick, G. *Hybrid Materials: Synthesis, Characterization, and Applications*; John Wiley & Sons, 2007.

(22) Hao, J.-N.; Yan, B. Hybrid Polymer Thin Films with a Lanthanide-zeolite A Host-guest System: Coordination Bonding Assembly and Photo-Integration. *New J. Chem.* **2014**, *38*, 3540–3547.

(23) Suárez, S.; Devaux, A.; Bañuelos, J.; Bossart, O.; Kunzmann, A.; Calzaferri, G. Transparent Zeolite-Polymer Hybrid Materials with Adaptable Properties. *Adv. Funct. Mater.* **2007**, *17*, 2298–2306.

(24) Funk, C. V. *Microporous Mixed Matrix (ZeoTIPS) Membranes*; ProQuest, 2008.

(25) Cohen, S. M. Postsynthetic Methods for the Functionalization of Metal-Organic Frameworks. *Chem. Rev.* **2012**, *112*, 970–1000.

(26) Yang, S. J.; Cho, J. H.; Nahm, K. S.; Park, C. R. Enhanced Hydrogen Storage Capacity of Pt-Loaded CNT@MOF-5 Hybrid Composites. *Int. J. Hydrog. Energy* **2010**, *35*, 13062–13067.

(27) Bandosz, T. J.; Petit, C. MOF/graphite Oxide Hybrid Materials: Exploring the New Concept of Adsorbents and Catalysts. *Adsorption* **2011**, *17*, 5–16.

(28) Ikezoe, Y.; Washino, G.; Uemura, T.; Kitagawa, S.; Matsui, H. Autonomous Motors of a Metal-organic Framework Powered by Reorganization of Self-Assembled Peptides at Interfaces. *Nat. Mater.* **2012**.

(29) Lu, G.; Farha, O. K.; Zhang, W.; Huo, F.; Hupp, J. T. Engineering ZIF-8 Thin Films for Hybrid MOF-Based Devices. *Adv. Mater.* **2012**, *24*, 3970–3974.

(30) Zhang, R.; Ji, S.; Wang, N.; Wang, L.; Zhang, G.; Li, J.-R. Coordination-Driven In Situ Self-Assembly Strategy for the Preparation of Metal-Organic Framework Hybrid Membranes. *Angew. Chem. Int. Ed.* **2014**, *53*, 9775–9779.

(31) Zhang, W.; Lu, G.; Li, S.; Liu, Y.; Xu, H.; Cui, C.; Yan, W.; Yang, Y.; Huo, F. Controlled Incorporation of Nanoparticles in Metal-organic Framework Hybrid Thin Films. *Chem. Commun.* **2014**, *50*, 4296–4298.

(32) Zhang, Z.; Huang, Y.; Ding, W.; Li, G. Multilayer Interparticle Linking Hybrid MOF-199 for Noninvasive Enrichment and Analysis of Plant Hormone Ethylene. *Anal. Chem.* **2014**, *86*, 3533–3540.

(33) Jin, S.; Son, H.-J.; Farha, O. K.; Wiederrecht, G. P.; Hupp, J. T. Energy Transfer from Quantum Dots to Metal-Organic Frameworks for Enhanced Light Harvesting. *J. Am. Chem. Soc.* **2013**, *135*, 955–958.

(34) Li, H.; Eddaoudi, M.; O'Keeffe, M.; Yaghi, O. M. Design and Synthesis of an Exceptionally Stable and Highly Porous Metal-Organic Framework. *Nature* **1999**, *402*, 276–279.

(35) Cychosz, K. A.; Wong-Foy, A. G.; Matzger, A. J. Enabling Cleaner Fuels: Desulfurization by Adsorption to Microporous Coordination Polymers. *J Am Chem Soc* **2009**, *131*, 14538–14543.

(36) Wong-Foy, A. G.; Matzger, A. J.; Yaghi, O. M. Exceptional H2 Saturation Uptake in Microporous Metal-Organic Frameworks. *J Am Chem Soc* **2006**, *128*, 3494–3495.

(37) Park, T.-H.; Hickman, A. J.; Koh, K.; Martin, S.; Wong-Foy, A. G.; Sanford, M. S.; Matzger, A. J. Highly Dispersed Palladium(II) in a Defective Metal-Organic Framework: Application to C-H Activation and Functionalization. *J Am Chem Soc* **2011**.

(38) Eddaoudi, M.; Kim, J.; Rosi, N.; Vodak, D.; Wachter, J.; O'Keeffe, M.; Yaghi, O. M. Systematic Design of Pore Size and Functionality in Isoreticular MOFs and Their Application in Methane Storage. *Science* **2002**, *295*, 469–472.

(39) Nguyen, J. G.; Cohen, S. M. Moisture-Resistant and Superhydrophobic Metal-Organic Frameworks Obtained via Postsynthetic Modification. *J Am Chem Soc* **2010**, *132*, 4560–4561.

(40) Koh, K.; Wong-Foy, A. G.; Matzger, A. J. MOF@MOF: Microporous Core-Shell Architectures. *Chem. Commun.* **2009**, 6162–6164.

(41) Schoenecker, P. M.; Carson, C. G.; Jasuja, H.; Flemming, C. J. J.; Walton, K. S. Effect of Water Adsorption on Retention of Structure and Surface Area of Metal-Organic Frameworks. *Ind. Eng. Chem. Res.* **2012**, *51*, 6513–6519.

(42) Hausdorf, S.; Wagler, J.; Mossig, R.; Mertens, F. O. R. L. Proton and Water Activity-Controlled Structure Formation in Zinc Carboxylate-Based Metal Organic Frameworks. *J Phys Chem A* **2008**, *112*, 7567–7576.